ISSN 2949-561X (Online)

APPLIED PHYSICS

1` 26

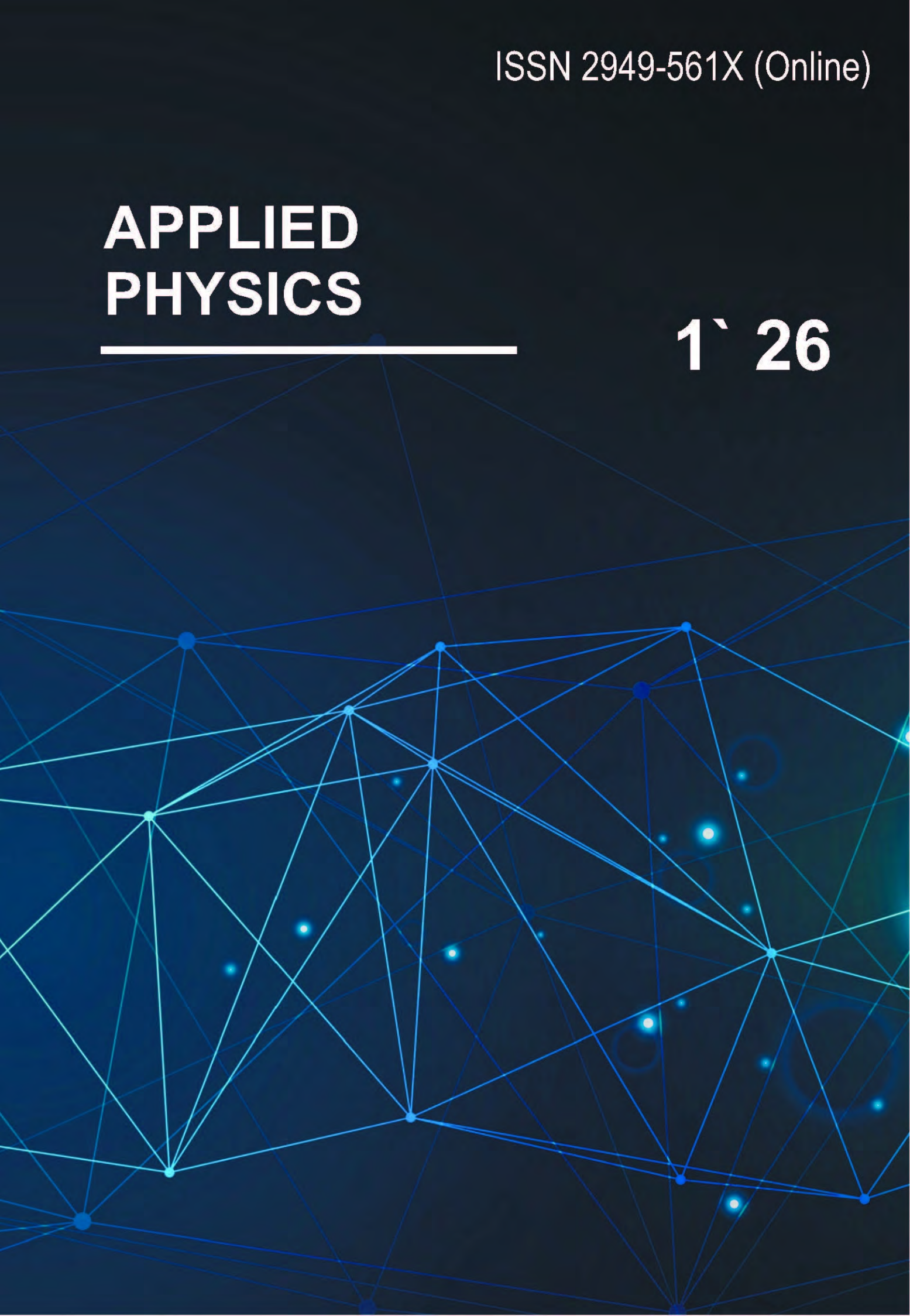

Applied Physics
2026, No. 1

The journal was founded in 1994

The scientific and technical peer-reviewed journal is intended for the publication of articles on the latest achievements in the field of physics with prospects for advancements (technical and scientific) applications.

The periodicity is 6 issues per year.

Founder and publisher

Research, Development and Production Center ORION, Joint-Stock Company – Russian Federation State Science Center
(RD&P Center ORION, JSC)
9, Kosinskaya st., Moscow, 111538 Russia

The journal is included into the List of peer-reviewed science press of the State Commission for Academic Degrees and Titles of Russian Federation. The Journal is included in Scientific Electronic Library eLIBRARY.RU, SCOPUS, Chemical Abstracts (CA), Russian Science Citation Index (RSCI), Directory of Open Access Journals (DOAJ), Directory of Open Access Scholarly Resources (ROAD), Google Scholar.

Editor-in-Chief

Editorial office address

9, Kosinskaya st., Moscow, 111538, Russia,
RD&P Center ORION, JSC.
Phone: 8(499) 374-82-40
E-mail: advance@orion-ir.ru
Internet: applphys.orion-ir.ru

The registration PI No. FS 77-73641
was issued in September 21, 2018
by the Federal Service for Supervision
of Communications, Information Technology, and Mass Media of Russia

Editorial Board

APPLIED PHYSICS [in Russian]

THE SCIENTIFIC AND TECHNICAL JOURNAL

2026, No. 1 | Founded in 1994 | Moscow

C O N T E N T S

PHYSICAL SCIENCE OF MATERIALS

PHYSICAL EQUIPMENT AND ITS ELEMENTS

PERSONALI

INFORMATION

GENERAL PHYSICS

UDC 621.384.62; 629.7 PACS: 87.65.+y, 96.50.Pw
EDN: WKNQBM

The influence of the Earth's exosphere on the micro-destruction of materials of space stations

© L. M. Vasilyak[1,*], A. V. Peklevskiy[2], S. P. Prokopovich[2], V. N. Chikirev[2], and E. V. Shubralova[2]

[1] *Joint Institute for High Temperatures of the Russian Academy of Sciences, Moscow, 125412 Russia*
[*] *E-mail: vasilyak@ihed.ras.ru*
[2] *Joint Stock Company "Central Research Institute for Machine Building", Moscow Region, Korolev, 141070 Russia*

Received 5.12.2025; revised 14.01.2026; accepted 20.02.2026

Research under the Test space experiment program on the physical and chemical properties of the resulting fine sediment on the surface of the International Space Station (ISS) has confirmed the possibility of its active participation in the aggressive influence of its own external atmosphere on the development of micro-degradation of ISS materials. An example of the effect of chemical elements with high electron affinity from volcanic gases reaching the surface of the ISS on the tightness of seals in portholes is given. The presence of graphite on the windows of portholes, samplers and cleaners indicates the degradation of the sealing materials, which can lead to leakage of the gaseous medium. The Test experiment showed that the natural contamination of the ISS surface by dispersed particles of the cosmosol requires consideration of the aging of station materials and their corrosion resistance, taking into account the external environment.

Keywords: international space station, fine deposition, exosphere.

DOI: 10.51368/2949-561X-2026-1-5-10

Introduction

One of the objectives of the "Test" space experiment during 2010–2024 was the collection of fine-dispersed sediment from the surface of the Russian Segment of the ISS using a special sampler for its physicochemical analysis in order to study the transfer of matter in space [1–5]. Sampling is performed by a cosmonaut during extravehicular activity into a container-monoblock (sampler), which is maintained sterile and hermetically sealed throughout the experiment, including during delivery to Earth. The objective of the ground-based phase is to conduct physicochemical, toxicological, microbiological, and molecular analysis of the samples.

Studies of the composition of the fine-dispersed sediment make it possible to assess the potential for micro-destruction of the pressurized hull, degradation of the transparency of portholes, and deterioration of the operational characteristics of solar panels and radiators under the influence of space factors, and to formulate requirements for advanced structural materials. Analysis of the physicochemical properties of the sediment allows determining its role in the aggressive impact on structural elements and, based on its elemental composition, identifying the source of its entry into the ISS's own external atmosphere, as well as refining data on the geochemical composition of cosmic dust at an altitude of 400 km above the Earth's surface and its sources.

Analysis of the possible influence of fine-dispersed sediment on materials of space objects

It has been established that the dispersed composition of cosmic dust on the ISS surface consists of three fractions: micron-sized (1 μm and 5 μm), submicron (the dominant fraction), and nanoparticles. Out of 46 studied samples, at least one element with high electron affinity was found in 27 samples, including chlorine (17 samples), fluorine (6 samples), and sulfur (17 samples), which are known to be constantly present in volcanic gases. Furthermore, the presence of traces of volcanic gases was confirmed by the simultaneous detection of the rare-earth element rhenium and radioactive elements (uranium, thorium, radium, cesium). Rhenium had not previously been detected in cosmic bodies; therefore, it can be assumed that this element is of terrestrial origin. The most probable source of rhenium reaching the ISS surface is the fumarolic gas-steam emissions of the Kudryavy volcano on Iturup Island. Kudryavy volcano represents a rare case of long-term, stationary, high-temperature magmatic degassing, in whose fumarolic gas-steam-dust emissions the amount of rhenium can reach 20–36 tons per year. It is the only open deposit of rhenium, the third largest in the world in terms of reserves of this metal; moreover, radioactive elements (uranium, thorium, radium, cesium) are also constantly present in the fumarolic gases of the Kudryavy volcano [3, 5].

Sulfur, chlorine, and fluorine particles, often detected in the composition of fine-dispersed sediment samples from the ISS surface, are not permanent elements of cosmic dust, but they are always present in volcanic gas emissions and are the main aggressive components of fumarolic gases. These elements actively participated in the formation of the Earth's primary atmosphere and still influence the climate. Ionized particles from gas-dust emissions enter the upper part of the ionosphere at the altitude of the ISS orbit via the ascending branch of the global electrical circuit connecting the stratosphere and the ionosphere. On their "crest", rapid injection of aerodispersed particles into the ionosphere with a change in the phase state "aerosol-cosmosol" is possible [6].

Thus, the detection of rhenium, sulfur, chlorine, and fluorine on the ISS surface based on the results of geological and mineralogical analysis is proof that during volcanic eruptions, gas-dust emissions can rise not only to the altitude of the stratosphere, but also much higher into space to an altitude of 400 km above the Earth. This fact poses an important materials science challenge: to investigate the impact of the deposition of constantly incoming elements with high electron affinity on the condition of materials of orbital objects, seals, porthole glasses, optical instruments, etc.

It should be noted that in the composition of 46 fine-dispersed sediment samples from the ISS surface, 65 chemical elements were found, and only in 5 fine-dispersed sediment samples from the RS ISS surface were no traces of iron detected [3]. In particles of volcanic gases rising beyond the atmosphere to orbital altitude, iron chloride, released from the magmatic melt at high temperatures, may be present. The presence of iron chloride particles in volcanic gases is associated with the reaction of magma with chlorine-containing compounds, which can also be released during an eruption. The volatile form of iron chloride is anhydrous iron chloride $FeCl_3$, which transitions into a gaseous state upon strong heating, forming $FeCl_3$ monomers and Fe_2Cl_6 dimers [7, 8].

The interaction of iron chloride with compact aluminum leads to the accumulation of iron ions, culminating in the deposition of iron in a free state and the appearance of ferrimagnetic particles found on the surface of the fluoroplastic housings of the "Test" instruments. Chloride ions migrate through the oxide film to the metal primarily at defect sites, increasing the corrosion rate [7, 8].

Analysis of the chemical composition of contaminants on porthole glazing revealed a predominance of zinc oxide, which suggests the dispersion of coatings from radiators and other structural elements painted with enamels containing zinc. Silicon, aluminum, potassium, chlorine, fluorine, and sulfur are present as impurities. The presence of carbon was established, with a predominantly tabular particle shape. When sampling from portholes on the glass and at the interface with the frame, and during subsequent cleaning of the glass with special devices, black traces of tabular graphite were always found (Fig. 1).

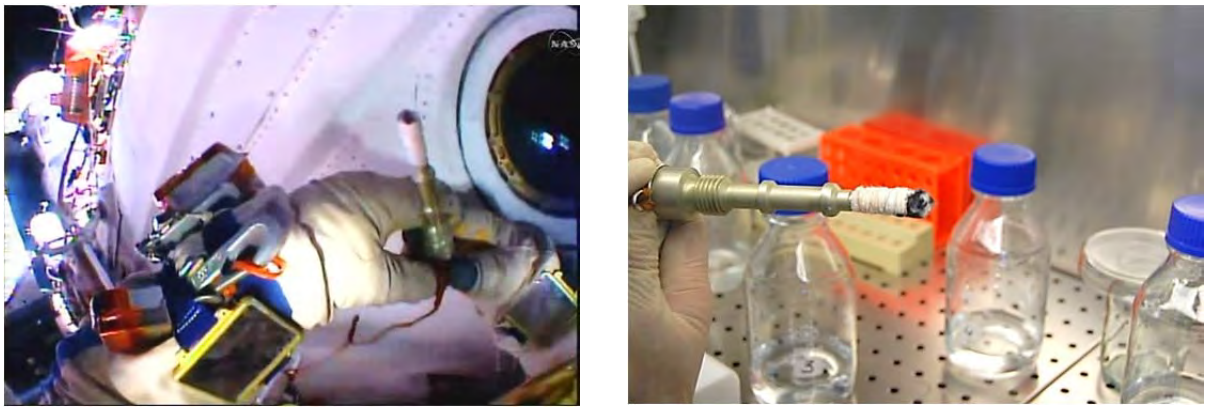

Fig. 1. Sampling from the porthole glass of the ISS service module (left) and view of the black sediment on the sampler swab delivered to the laboratory (right)

The presence of noticeable traces of tabular graphite on porthole glasses, samplers, and cleaning devices indicates ongoing processes of material degradation. Paronite, used as a sealant for porthole frames, contains more than 10 % graphite, including the tabular variety. It is known that under the influence of chlorine, interacting with other chemical components of paronite, the graphite is liberated. This circumstance could affect the tightness of seals in the porthole structures of orbital objects during their long-term operation. It should be noted that it is difficult to pinpoint the location of air leakage due to seal damage using instrumental means.

During the ISS-71 expedition (2024), cosmonauts O. Kononenko and N. Chub discovered the presence of condensate on the inner glass of porthole No. 1 of the small laboratory module MLM-U, indicating a leak in the frame seal. Earlier, on June 12, 2022, a photo of a crescent-shaped frost patch was taken by cosmonaut S. Korsakov on the inner side of the outer glass of this same porthole (Fig. 2). This indicates that a small air leak process has been occurring in the structure of porthole No. 1 of the MLM-U for two years. The formation of ice can be explained by the fact that in 2022, as a result of air leakage into the space between the porthole panes, thermodynamic conditions corresponding to the triple point of water were established: pressure 4.6 Torr (0.006 atm) and temperature 0.01 °C on the inner side of the outer glass. Due to the continued air leak into the inter-pane space, the pressure exceeded 4.6 Torr, and condensate droplets appeared.

Fig. 2. Photo of frost on the inner side of the outer porthole glass

Since the temperature of the outer glass decreases from the frame (at the temperature of the external structural elements of the ISS) towards the center of the glass (reaching temperatures near or below zero), the zone of maximum deposited frost layer and subsequently the location of droplets may indicate the location of the frame seal leak. One possible cause could be the degradation of the paronite seal tightness.

In 2021, to study the long-term survival of microorganisms in open space, two "Test-Exhibit" devices were installed on the handrails of the Poisk module for 3.5 years. The surface areas of the fluoroplastic sealed units were of interest for research, as a coating of fine-dispersed matter from the cosmosol composition formed on their surface. After the "Test-Exhibit" devices were delivered to Earth in 2024,

a scraping was taken from the fluoroplastic unit, and a conditionally clean area was cut from inside the unit for physicochemical analysis of the fine-dispersed substance. Analysis showed that the housing was covered with a reddish-colored sediment, which adhered quite firmly to the fluoroplastic surface, did not transfer to gloves, and was practically not removable with a cotton swab (Fig. 3).

Fig. 3. Sediment on the surface of the "Test" housing

Elemental analysis of the samples was performed using inductively coupled plasma optical emission spectrometry. The results obtained generally repeat the findings of previous papers. The ratio of elements may resemble both the composition of stony meteorites and that of ordinary mineral dust on Earth, as these are the most common elements on Earth. The data for iron and nickel allow for an analysis of the iron's origin. The iron/nickel ratio in the studied sample is 335; consequently, these iron particles are not of meteoritic origin, as for meteorites this ratio does not exceed 14.

In 2019, All-Russian Scientific Research Institute for Physical-Engineering and Radiotechnical Metrology analyzed objects that had been exposed on the external surface of the ISS and contained fine-dispersed particles: a roll of cotton fabric material exposed for 10 years on a bracket of the Zvezda module, and the fluoroplastic "Test-Exhibit" device on a bracket of the Pirs module after 1 year of exposure. Neutron activation analysis (NAA), a highly sensitive and accurate method used for the quantitative analysis of major, minor, and trace elements, was employed for sample analysis. The NAA technique is based on measuring the radiation emitted during the decay of radioactive nuclei formed as a result of irradiating the material with neutrons. The iron/nickel ratios in the studied samples were: for the fluoroplastic instrument housing in 2019–220 (in 2024–335); for the contaminated area of the cotton fabric – 280; and for the clean area – 236.

It is important to note the concentration of uranium and thorium [3] in the samples. Their quantities are small, but this method has excellent resolution for such heavy nuclei. Their amount increased by 3–4 times in the contaminated area. The appearance of these elements could be explained by ground-based testing, the operation of satellites with nuclear power sources, or traces of volcanic gases.

While working with the contaminated fabric areas, its low mechanical strength and increased brittleness were noted. When cutting, the surface fibers crumbled and scattered. This did not occur with the uncontaminated areas. Therefore, a comparative analysis of the contaminated and uncontaminated fabric areas was performed using a JEOS jsm-35CF scanning electron microscope. Several types of defects were found in the contaminated fabric that were absent in the clean fabric and are not characteristic of cotton. "Eroded" and "crumbling" fibers were identified in the contaminated area (Fig. 4).

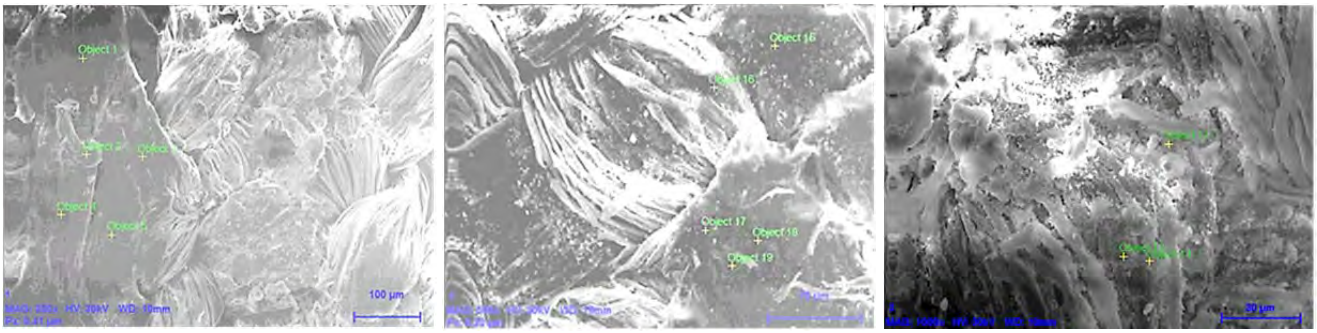

Fig. 4. Enlarged fabric fragments

Loops of fabric fibers were preserved only in a small area. Since the fabric fibers were destroyed, the mechanical properties of intact loops on both sides of the fabric were investigated. On the outer side (which had been exposed), the loops tear with almost no elongation, under a force approximately five times smaller. On the protected side, the minimum breaking force was 1.5 kgf, and the maximum was 2 kgf. On the outer side, in the brown areas, the maximum withstandable mass was 0.5 kg, the minimum about 0.25 kg; in the white areas, it was 1.5 kg and 0.75 kg, respectively.

Elements Al, Si, Ca, and Mg, which are most often found in cosmic dust and meteorites, were detected on both sides of the fabric. On the outer side, S, Cl, and F, which are present in volcanic gases, were also found. The detection of Zn confirms the dispersion of coatings from structural elements painted with zinc-containing enamels. The difference in composition may be a consequence of different velocities of dust particles. Sol particles are extremely small and, moving at high speed, become embedded in the fabric fibers. At high speed, they can pass through the material.

Thus, studies of the physicochemical properties of the fine-dispersed sediment forming on the ISS surface have confirmed its potential active role in the aggressive influence of the own external atmosphere on the development of micro-destruction of structural elements made of various materials on the ISS. This circumstance creates new requirements for the surface materials of spacecraft, coatings, and protective elements, considering the adsorption and accumulation of particles of various origins.

Conclusion

The results of the "Test" space experiment have shown that orbital constellations and space debris act as collectors and carriers of aggressive chemical elements on their surfaces, which are not dispersed into space as previously assumed. It has been discovered that chemically active elements and iron particles can be a result of volcanic activity. The continuous influx of biogenic material, meteoroid stream particles, chemically active elements from volcanic gases, and, importantly, radioactive particles onto the ISS surface necessitates further study of the corrosion resistance of surfaces under conditions of long-term combined exposure to the aggressive near-Earth environment. This defines new hazardous factors of the Earth's exosphere's influence not only on the technical condition of orbital assets externally, but also internally after frequent crew extravehicular activities. Elements of the fine-dispersed sediment accumulated on the external surface of any object will fall to Earth upon the spacecraft's return, and this could pose a danger. Research on the transfer of matter in space is an important task, also necessary for planetary safety.

REFERENCES

1. Shubralova E. V., Peklevskiy A. V., Prokopovich S. P., Uspenskiy F. A., and Chikirev V. N. Cosmic Research, **63** (2), 29–38 (2025) [in Russian].
2. Vasilyak L. M., Shubralova E. V., and Chikirev V. N., Applied Physics, № 6, 14–19 (2024) [in Russian].
3. Zinicovscaia I., Grozdov D., Yushin N., Safonov A., Proshin I., Volkov M., Pryadka A., Belyaev V., Shubralova E., and Tsygankov O., Acta Astronautica **189**, 278–282 (2021).
4. Grebennikova T. V., Syroeshkin A. V., Shubralova E. V., Eliseeva O. V., Kostina L. V., Kulikova N. Y., Latyshev O. E., Morozova M. A., Yuzhakov A. G., Zlatskiy I. A., Chichaeva M. A., and Tsygankov O. S., Scientific World Journal **2018**, 7360147, 1–7 p.
5. Ponomarev G. P., Rashidov V. A., Chuburkov Yu. T. et al., Proceedings of the All-Union Conference “Geodynamics, magmatism and minerageny of the continental margins of the North Pacific” **2**, 200–201 (2003).
6. Popel S. I., Priroda, № 9, 48–56 (2015) [in Russian].
7. Kolpakov M. E., Dresvyannikov A. F., and Yusupov R. A. https://cyberleninka.ru/article/n/dinamika-himicheskih-ravnovesiy-sistemy-fe-ii-fe-iii-al-iii-h2o-pri-korrozii-alyuminiya-v-rastvore-hlorida-zheleza-iii-vysokoy/viewer p. 132–139 [in Russian].
Dresvyannikov A. F. and Kolpakov M. E., Journal of Physical Chemistry **77** (5) 807 (2003) [in Russian].

About authors

Vasilyak Leonid Mikhailovich, Doctor of Physical and Mathematical Sciences, Chief Researcher, Joint Institute for High Temperatures of the Russian Academy of Sciences, (Bd. 2, 13 Izhorskaya st., Moscow, 125412, Russia). E-mail: vasilyak@ihed.ras.ru SPIN-code: 5623-5167, AuthorID: 19599, ORCID 0000-0001-6982, Scopus 7004886755

Peklevsky Andrey Viktorovich, Candidate of Physical and Mathematical Sciences, Leading Researcher, Joint Stock Company “Central Research Institute for Machine Building” (4 Pionerskaya st., Korolev, Moscow Region, 141070, Russia). E-mail: 5737@mail.ru SPIN code: 1870-6205

Prokopovich Sergey Pavlovich, Head of Department, Joint Stock Company “Central Research Institute for Machine Building” (4 Pionerskaya st., Korolev, Moscow Region, 141070, Russia). E-mail: prokopovichsp@tsniimash.ru

Chikirev Vladimir Nikolaevich, Chief Specialist, Joint Stock Company “Central Research Institute for Machine Building” (4 Pionerskaya st., Korolev, Moscow Region, 141070, Russia). E-mail: vladch56@yandex.ru AuthorID: 609834

Shubralova Elena Vladimirovna, Chief Specialist, Joint Stock Company “Central Research Institute for Machine Building” (4 Pionerskaya st., Korolev, Moscow Region, 141070, Russia). E-mail: shubralova@mail.ru SPIN-code: 2734-5521, AuthorID: 1317404

PHOTOELECTRONICS

UDC 621.383.4/5
EDN: YKQGBS

PACS: 42.79.Pw, 85.60.Gz,
07.57.Kp, 85.60.Dw

Investigation of focal plane arrays based on CdHgTe barrier structures for medium-wavelength IR spectral range

© K. O. Boltar[1,2], I. D. Burlakov[1,3], N. I. Iakovleva[1,*], A. V. Trukhachev[1], D. I. Gorn[4], and N. N. Mikhailov[5]

[1] *RD&P Center ORION, JSC, Moscow, 111538 Russia*
[*] *E-mail: niiakovleva@mail.ru*
[2] *Moscow Institute of Physics and Technology, Moscow Region, Dolgoprudny, 141701 Russia*
[3] *MIREA – Russian Technological University, Moscow, 119454 Russia*
[4] *National Research Tomsk State University, Tomsk, 634050 Russia*
[5] *Rzhanov Institute of Semiconductor Physics of the Siberian Branch of the Russian Academy of Sciences, Novosibirsk, 630090 Russia*

Received 23.10.2025; revised 23.12.2025; accepted 20.02.2026

Using experimental technology, focal plane arrays (FPAs) for the medium-wavelength spectral range (MWIR) based on nBn-heterostructures with unipolar barriers and HgTe/CdHgTe superlattices barriers have been manufactured and investigated. The current-voltage, spectral characteristics and performance of photosensitive elements of experimental samples have been measured. The performance confirm the possibility of creating FPAs based on CdHgTe nBn-heterostructures with wide-band barriers and superlattices as barriers, and technical and constructive technological solutions for their manufacture.

Keywords: unipolar photodetector, *n*B*n*-heterostructure, MWIR, HgCdTe, MCT, Focal Plane Array (FPA), spectral response.

DOI: 10.51368/2949-561X-2026-1-11-17

1. Introduction

Hot operating temperature is the main goal for development of infrared (IR) Focal Plane Arrays (FPA) designed for thermal imaging and heat direction finding systems. The work at high operating temperature, as well as achieving high performance, is the choice of CdHgTe unipolar nBn heterostructures with wide-band barriers and superlattices as barriers, operating in MWIR (3–5 μm) and LWIR (8–12 μm) [1–4].

The *nBn*-heterostructure production is carried out using advanced methods of $Cd_xHg_{1-x}Te$ epitaxial growth by molecular beam epitaxy [5], since MBE provides multilayer structures with a given doping level and type of conductivity.

Despite on the some advantages of barrier photodetectors, the FPA implementation is a difficult task due to the presence of an undesirable VBO in the the band diagram at the absorbing/barrier boundary in the MCT structure. The propagation of the barrier layer into the valence band of the *n*B*n*-srtucture limits the non-primary charge carriers (holes) moving, which determine the useful component of the signal current in such devices. The gap in the valence band can be reduced if the barrier layer is replaced with an HgTe/CdHgTe superlattice, which was proposed in specialized papers [6, 7].

The main goal of this work is a study of MWIR photodetector devices based on *n*B*n*-architectures with CdHgTe unipolar barriers and HgTe/CdHgTe superlattice barriers to create a new FPAs generation.

2. Configuration of barrier *n*B*n* structures based on CdHgTe

MWIR *n*B*n*-structures with unipolar barriers and superlattices as barriers have been selected for the photosensitive arrays manufacture.

The composition distribution versus thickness in the CdHgTe unipolar barrier structures with the barrier (*a*) and the superlattice as a barrier (*b*) is shown in Figure 1.

The composition distributions in the barrier layer of two architectures: with the unipolar barrier and with the HgTe/CdHgTe superlattice barrier are shown in Figure 2 (*a*, *b*).

Figure 2*a* shows that from left to right of the substrate there is the barrier with a thickness of about ~ 400 nm and $x = 0.7$. Presented in Figure 2*b* the barrier layer with a thickness of about 130 nm was formed by the superlattice consisting of 10 periods of HgTe/$Cd_xHg_{1-x}Te$, while the wideband layer was the $Cd_xHg_{1-x}Te$ ternary alloy of $x = 0.7$, the second layer was formed by the semi-metallic HgTe. The thickness of the layers was approximately correlated as ~ 2/5.

$Cd_xHg_{1-x}Te$ barrier structures were grown at the Institute of Semiconductor Physics of the Siberian Branch of the Russian Academy of Sciences by molecular beam epitaxy (MBE) on GaAs (013) substrates [8]. The parameters of the individual layers of the *n*B*n* structure are presented in Table 1.

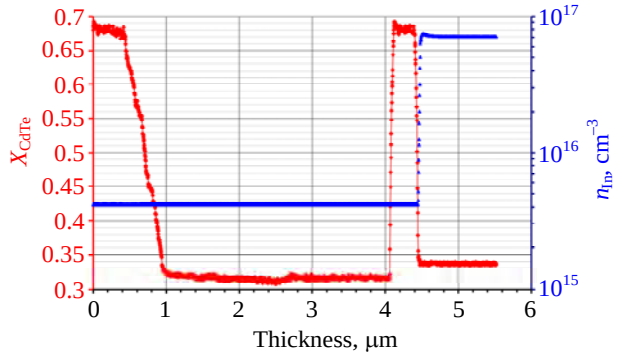

a) CdHgTe *n*B*n*-heterostructure with wideband unipolar barrier

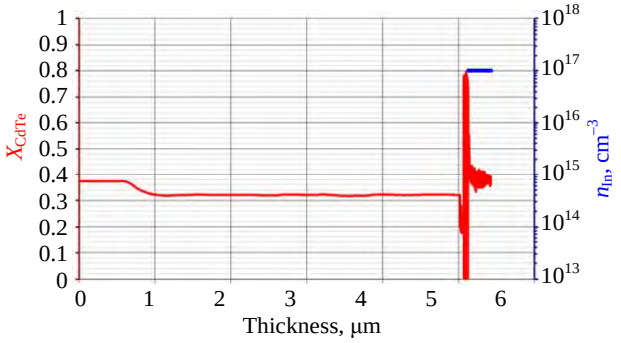

b) CdHgTe *n*B*n*-heterostructure with the superlattice as a barrier

Fig. 1. The composition and concentration distributions versus the doping impurity and thickness in CdHgTe nBn-heterostructures with an absorbing layer of x = 0.3

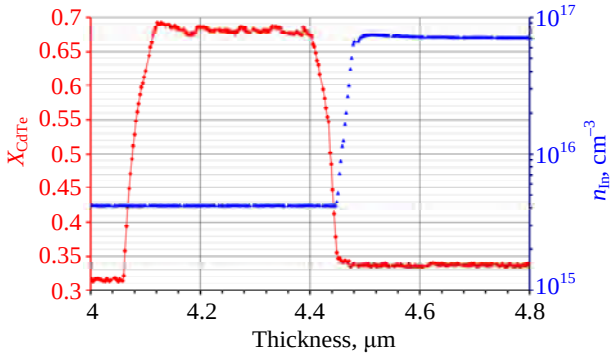

a) CdHgTe *n*B*n*-heterostructure with wideband unipolar barrier

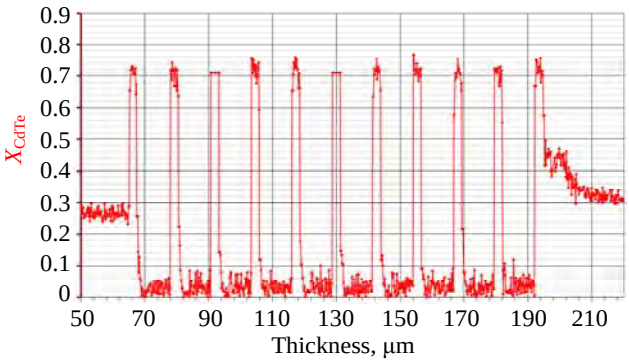

b) CdHgTe *n*B*n*-heterostructure with the superlattice as a barrier

Fig. 2. The composition distribution the in the barrier layer of two architectures: with the unipolar barrier (a) and with the HgTe/CdHgTe superlattice barrier (b)

Table 1

Layer parameters of nBn-heterostructures based on CdHgTe

Name of the layer in the structure	MCT HES with a unipolar barrier			MCT HES with a superlattice $HgTe/Cd_xHg_{1-x}Te$		
	Concentration, cm^{-3}	Composition	Thickness, μm	Concentration, cm^{-3}	Composition	Thickness, μm
n-$Cd_xHg_{1-x}Te$ contact layer	$n \sim (3–8)\times10^{16}$	0.34	0.2	$n \sim (3–8)\times10^{16}$	0.32	0.5
n-$Cd_xHg_{1-x}Te$ barrier layer	–	0.7 (barrier)	0.35	–	0.72 (barrier) / 0.03 (well)	0.004 (barrier)/ 0.010 (well); 10 periods 0.140 (total)
$Cd_xHg_{1-x}Te$ absorbing *n*-layer	$n \sim (3–5)\times10^{15}$	0.32	3.0–4.0	$n \sim (3–5)\times10^{15}$	0.30	3.0–4.0
Graded-gap base CdHgTe	–	1.0–0.32	1.0	–	1.0–0.30	1.0
CdTe buffer layer	–	–	5.5	–	–	5.5
ZnTe buffer layer	–	–	0.03	–	–	0.03
Optically transparent GaAs (013) substrate, ∅ 50.8 mm			600			600

During the MBE growth process a ZnTe buffer layer (~ 30 nm thick), then a CdTe buffer layer (~ 5.5 μm thick), and a $Cd_xHg_{1-x}Te$ gradient layer (~ 1 μm thick) were formed on the GaAs substrate. The *n*B*n*-architecture included *n*-$Cd_xHg_{1-x}Te$ absorbing, barrier and contact layers, the concentration in the absorbing and barrier layers was $n \sim (3–5)\times10^{15}$ cm^{-3}, the concentration in the contact layer exceeded $n > 3\times10^{16}$ cm^{-3}. The $Cd_xHg_{1-x}Te$ absorbing layer had 3–4 μm thickness, the CdTe composition in the barrier layer and the composition in the contact layer with a thickness of ~ 1 μm were depending on the operating spectral range. During the growing process, the doping donor impurity was indium.

3. Manufacturing and research FPAs on the basis of CdHgTe *n*B*n*-architectures

The properties of CdHgTe barrier *N*B*n*-architectures in which the barrier layer (B) effectively suppressed the current component of the main charge carriers (electrons) have been considered in the works [9, 10]. The same type of doping in the barrier and absorbing layers causes a low dark current limited by the diffusion mechanism [11].

Focal plane arrays based on CdHgTe *n*B*n*-heterostructures were manufactured using mesa technology. The size of the photosensitive elements and the step between them were guaranteed by the topological dimensions and the manufacturing accuracy of the photomasks. The separation of the matrix elements was carried out by ion plasma etching through a photoresist mask forward to a barrier or buffer n-layer with finishing liquid etching in order to obtain smooth profile of lateral surfaces and the bottom of the groove without additional inhomogeneities. The crystal of the 64×64 matrix with a step of 40 μm between the elements had overall dimensions of ~ 2.74×2.74 mm. The local sizes of the *n*-area collector were 0.02×0.02 mm, an ohmic contact was made to each matrix element by the technological operation of photolithography, and common indium microcontacts were formed to the base region of the crystal.

The matrix structure after the mesa etching operation with photosensitive elements separated by mesa grooves with indium microcontacts on the top surface is shown in Figure 3 (*a*, *b*).

The distance between the sensitive elements was ~ 11–13 microns. The anisotropic nature of the etching process in the vertical direction concerning to the surface is revealed. Small surface irregularities were observed on the surface of the dividing groove after etching.

Etching to a considerable depth was accompanied by a masking coating decrease

during etching, which led to an increase of separating groove size and a decrease in the area of the sensitive element. Elements with a groove depth exceeding the thickness of the barrier layer had a small sensitivity variation among themselves. There are a number of technological problems in the mesa etching process, one of which is the need for passivation of the mesa elements lateral surface in order to protect their surface and to reduce the processes of generation-recombination on the surface after the mesa etching operation.

The silicon integrated circuit designed for reading, pre-analog processing and output of photosignals from each element of the 64×64 matrix, has been provided the photocurrent accumulation on integration capacitors, amplification and multiplexing into 2 analog outputs.

The hybridization of CdHgTe FPA and silicon ROIC was carried out using indium microcontacts by pressure diffusion welding, which made it possible to obtain a reliable electrical connection of the assembled crystals. The hybrid crystals were placed in vacuum cryostats. The electrical outputs from the silicon ROIC contact pads were welded onto a sapphire raster with mounted thin gold wires, and then from the raster onto the external outputs of cryostat (fig. 4 *a*, *b*).

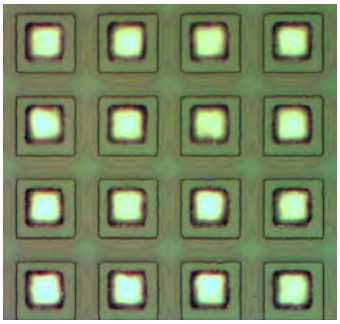

a) a fragment of the matrix structure with In microcontacts

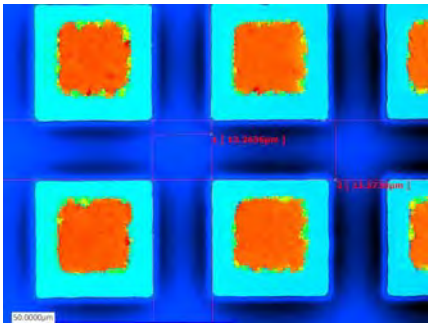

b) measuring the gap between the photosensitive elements

Fig. 3. Fragment of the matrix structure after the mesa etching operation

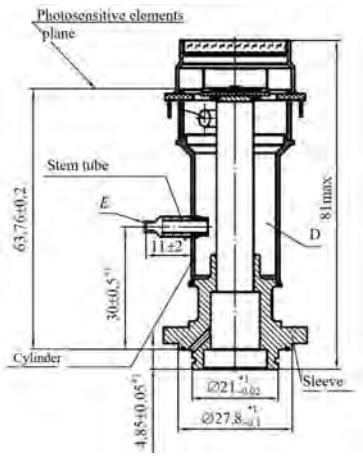

a) cryostat design

b) photo of the cryostat

Fig. 4. CdHgTe 64x64 FPA with the 40 μm step in the vacuum cryostat

The volt-ampere characteristics of the two test matrices FPA-01 and FPA-02 based on CdHgTe *n*B*n*-heterostructures at $T = 300$ K are shown in Figure 5 *a*, *b*.

The spectral response characteristics of the two test FPAs based on CdHgTe *n*B*n*-heterostructures with the wide-band barrier and with the superlattice as the barrier have been measured at $T = 300$ K. The measuring spectral responses of the test FPAs are shown in Figure 6 (*a*, *b*).

The measuring results of the spectral cutoffs of test FPAs based on CdHgTe *n*B*n*-

heterostructures with the wideband barrier (FPA-01) and with a superlattice as the barrier (FPA-02) are presented in Table 2.

The long-wavelength cutoff of the spectral sensitivity response for the elements of the test FPA-01 and FPA-02 are: $\lambda_{L0.5}$ = 5.13 μm and $\lambda_{L0.5}$ = 4.84 μm, they were formed by $Cd_xHg_{1-x}Te$ composition choosing, and the short-wavelength cutoff are $\lambda_{S0.5}$ = 2.74 μm and $\lambda_{S0.5}$ = 2.70 μm, they were determined by the absorption in the gradient layer of the *n*B*n*-heterostructure with a thickness of 1 μm.

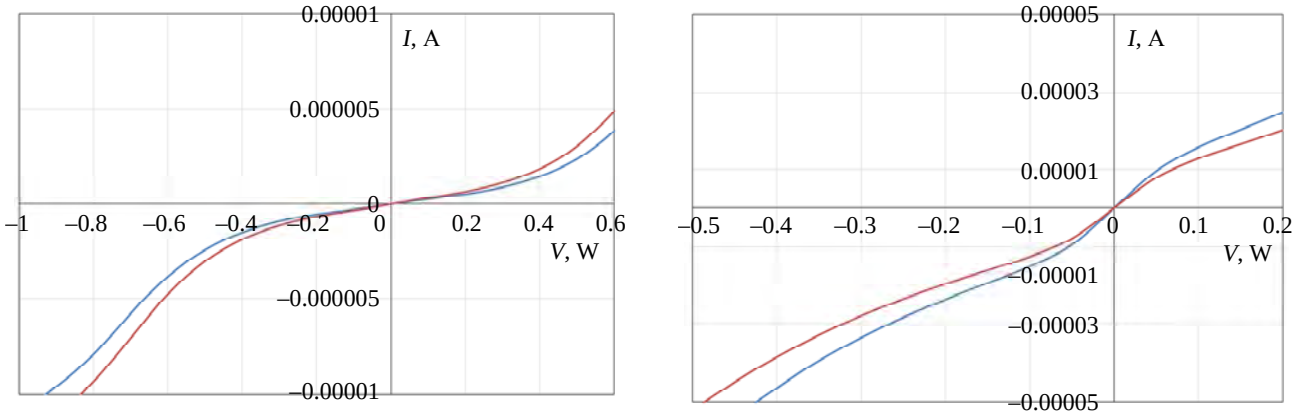

a) FPA-01 with wideband barrier *b*) FPA-02 with the superlattice as a barrier

Fig. 5. The volt-ampere characteristics of the two test matrices FPA-01 and FPA-02 based on CdHgTe nBn-heterostructures with wideband barrier (a) and with the superlattice as a barrier (b)

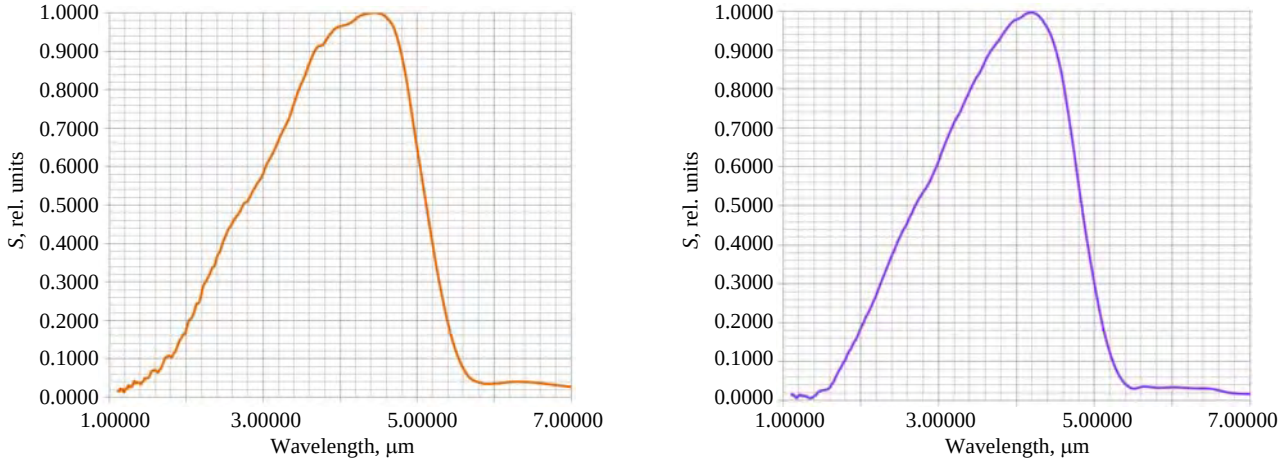

a) FPA-01 with wideband barrier *b*) FPA-02 with the superlattice as a barrier

Fig. 6. The measuring spectral responses of the test FPAs: (a) – with wideband barrier and (b) – with the superlattice as a barrier

Table 2

The spectral cutoffs of test FPAs based on CdHgTe nBn-heterostructures with the wideband barrier (FPA-01) and with a superlattice as the barrier (FPA-02)

Parameter name	Measurement results for FPA-01	Measurement results for FPA-02
1 Long-wave cutoff of the spectral sensitivity range, μm	5.13	4.84
2 Short-wave cutoff of the spectral sensitivity range, μm	2.74	2.70

The performance of FPAs based on CdHgTe *n*B*n*-heterostructures were determined by the photosignal and noise measurements. A flexible automated information processing system operating in automatic mode was used to carry out the measurements. The measuring system consisted of the following main components:

– an optical signal source based on a blackbody;

– control electronics (analog processing and control unit, analog-digital processing unit, interface unit);

– measuring system, which included a computing unit and interface boards.

Measurements of current, photosignal and noise of MWIR test devices FPA-01 and FPA-02 have been carried out (current diagrams for the arrays elements are shown in Figures 7 *a*, *b*).

The achievement of high performance of barrier FPAs is guaranteed both by the quality of the original CdHgTe heterostructures and by the manufacturing FPA technology, ROIC and hybrid assemblies based on them according to the developed technological process. The performance of MWIR barrier 64×64 FPAs with the 40 μm pitch based on CdHgTe *n*B*n*-heterostructures is presented in Table 3.

The average value of detectivity for FPA-01 was of $D^* = 0.52\times10^{11}$ cmHz$^{1/2}$W^{-1}; the average value of volt sensitivity for FPA-01 was $S_u = 0.3\times10^8$ V/W. The average value of detectivity for FPA-02 was of $D^* = 0.61\times10^{11}$ cmHz$^{1/2}$W^{-1}; the average value of volt sensitivity for FPA-02 was $S_u = 0.55\times10^8$ V/W.

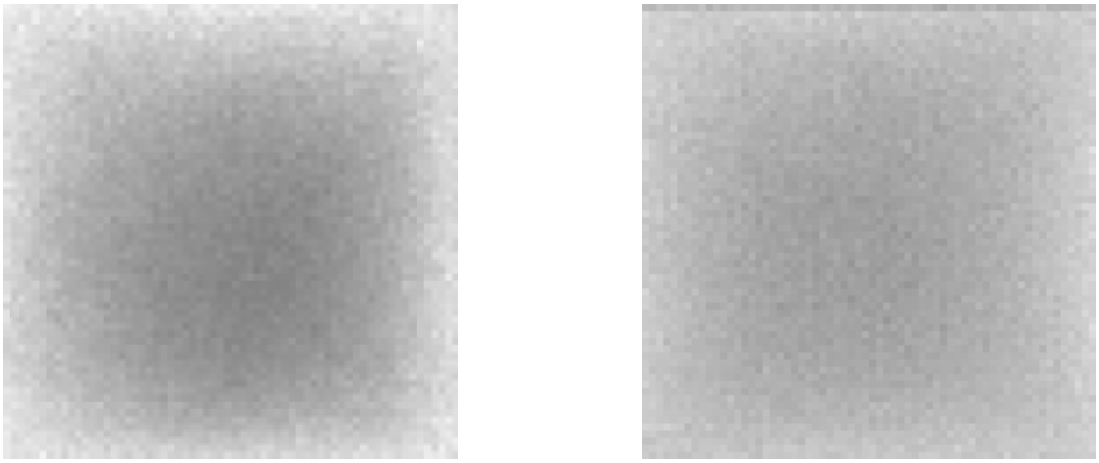

a) FPA-01 *b*) FPA-02

Fig. 7. Current distribution for FPAs format of 64×64 elements with the step of 40 μm based on CdHgTe MWIR barrier nBn-heterostructures

Table 3

The performance of MWIR barrier 64x64 FPAs with the 40 μm pitch based on CdHgTe nBn-heterostructures

FPA No.	Performance (800 K, T_{int} = 0.3 ms)		
	Volt sensitivity, Su, V/W	Noise N, μV	Detectivity D^*, cm·Hz$^{1/2}$·W^{-1}
FPA-01	0.3×10^8	0.35	0.52×10^{11}
FPA-02	0.55×10^8	0.30	0.61×10^{11}

The obtained values of the performances confirm the possibility of creating FPAs based on CdHgTe *n*B*n*-heterostructures with wide-band barriers and superlattices as barriers, as well as the correctness of technical and constructive technological solutions for their manufacture. The further improvement of the FPA performance, it is necessary to optimize the photosensitive element architectures and refine the manufacturing technology of FPAs based on CdHgTe *n*B*n*-heterostructures with wide-band barriers and with superlattices as barriers.

4. Conclusion

The paper presents promising CdHgTe *n*B*n*-architectures with unipolar barriers and superlattices as barriers, and experimentally

investigated performance and spectral responses for FPAs manufactured on their basis.

The following results were obtained:

The long-wavelength cutoff of the spectral sensitivity response for the elements of the test FPA-01 and FPA-02 are: $\lambda_{L0.5} = 5.13$ μm and $\lambda_{L0.5} = 4.84$ μm, they were formed by $Cd_xHg_{1-x}Te$ composition choosing, and the short-wavelength cutoff are $\lambda_{S0.5} = 2.74$ μm and $\lambda_{S0.5} = 2.70$ μm, they were determined by the absorption in the gradient layer of the *n*B*n*-heterostructure with a thickness of 1 μm. The detectivity was of $\sim 10^{11}$ cmHz$^{1/2}$W^{-1}; the average value of volt sensitivity was of $\sim 10^8$ V/W. The obtained values of the performances confirm the possibility of creating FPAs based on CdHgTe *n*B*n*-heterostructures with wide-band barriers and superlattices as barriers, as well as the correctness of technical and constructive technological solutions for their manufacture. The further improvement of the FPA performance, it is necessary to optimize the photosensitive element architectures and refine the manufacturing technology of FPAs based on CdHgTe *n*B*n*-heterostructures with wide-band barriers and with superlattices as barriers, as well as optimizing ROIC for this photosensitive element.

The research was carried out at the expense of a grant from the Russian Science Foundation No. 23-62-10021, https://rscf.ru/project/23-62-10021/.

REFERENCES

1. Boltar K. O., Burlakov I. D., Iakovleva N. I., Sednev M. V., Trukhachev A. V., Irodov N. A., Lopukhin A. A., Permikina E. V., Voitsekhovsky A. V., Gorn D. I., and Mikhailov N. N., Applied Physics, № 1, 38–44 (2025) [in Russian].
2. Voitsekhovsky A. V. and Gorn D. I., Applied Physics, № 4, 83–86 (2016) [in Russian].
3. Kopytko M. et al., J. Electron. Mater. **44** (1), 158–166 (2015).
4. Rogalski A., Martyniuk P., Kopytko M., and Hu W., Appl. Sci. **11**, 501 (2021).
5. Varavin V. S., Dvoretsky S. A., Mikhailov N. N., Remesnik V. G., Sabinina I. V., Sidorov Yu. G., Shvets V. A., Yakushev M. V., and Latyshev A. V., Autometry **56** (5), 12–26 (2020).
6. Akhavan N. D., Umana-Membreno G. A., Jolley G., Antoszewski J., and Faraone L., Appl. Phys. Lett. **105** (12), (2014).
7. Voitsekhovsky A. V., Dzyadukh S. M., Gorn D. I., Dvoretsky S. A., Mikhailov N. N., Sidorov G. Yu., and Yakushev M. V., Applied Physics, № 3, 37–42 (2022) [in Russian].
8. Varavin V. S., Sabinina I. V., Sidorov G. Yu., Marin D. V., Remesnik V. G., Predein A. V., Dvoretsky S. A., Vasilyev V. V., Sidorov Yu. G., Yakushev M. V., and Latyshev A. V., Infrared Phys. Technol. **105**, 103182 (2020). https://doi.org/ 10.1016/j.infrared.2019.103182.
9. Voitsekhovskii A. V., Nesmelov S. N., Dzyadukh S. M., Dvoretsky S. A., Mikhailov N. N., Sidorov G. Yu., and Yakushev M. V., Infr. Phys. and Techn. **102**, 103035 (1–4) (2019).
10. Jiale He, Peng Wang, Qing Li, Fang Wang, Yue Gu, Chuan Shen, Lu Chen, Piotr Martyniuk, Antoni Rogalski, Xiaoshuang Chen, Wei Lu, and Weida Hu, IEEE Trans. Electron Devices **67** (5), (2020).
11. Voitsekhovsky A. V., Dzyadukh S. M., Gorn D. I., Dvoretskii S. A., et al., Journal of Communications Technology and Electronics **69** (4–6), 231–235 (2024). https://doi.org/10.1134/S1064226924700372.

About authors

Boltar Konstantin Olegovich, Doctor of Physical and Mathematical Sciences, Director of Applied Development, RD&P Center ORION, JSC (9 Kosinskaya st., Moscow, 111538, Russia); Moscow Institute of Physics and Technology (9 Institutskiy per., Moscow Region, Dolgoprudny, 141701, Russia). E-mail: boltarko@yandex.ru SPIN-code: 9249-2720, AuthorID: 171355

Burlakov Igor Dmitrievich, Doctor of Technical Sciences, Professor, Deputy General Director for Innovation and Science, RD&P Center ORION, JSC (9 Kosinskaya st., Moscow, 111538, Russia); MIREA – Russian Technological University (78 Vernadsky Ave., Moscow, 119454, Russia). E-mail: idbur@orion-ir.ru SPIN-code: 6042-3634, AuthorID: 171368

Iakovleva Natalya Ivanovna, Doctor of Technical Sciences, Chief Scientific Officer of the STS MFE, RD&P Center ORION, JSC (9 Kosinskaya st., Moscow, 111538, Russia). E-mail: niiakovleva@mail.ru SPIN-code: 1077-9113, AuthorID: 602076

Trukhachev Anton Vladimirovich, Lead Engineer, RD&P Center ORION, JSC (9 Kosinskaya st., Moscow, 111538, Russia). E-mail: orionmoscow@mail.ru

Gorn Dmitry Igorevich, Candidate of Physical and Mathematical Sciences, Senior Research Associate, National Research Tomsk State University (36 Lenin Ave., Tomsk, 634050, Russia). E-mail: gorn_dim@sibmail.com SPIN-code: 4514-3163, AuthorID: 724442

Mikhailov Nikolay Nikolaevich, Candidate of Physical and Mathematical Sciences, Senior Research Associate, Rzhanov Institute of Semiconductor Physics of the Siberian Branch of the Russian Academy of Sciences (13 Lavrentiev Ave., Novosibirsk, 630090, Russia). E-mail: mikhailov@isp.nsc.ru SPIN-code: 3449-3155, AuthorID: 107682

PHOTOELECTRONICS

UDC 621.383
EDN: CYZISH
PACS: 85.60.–q

Encapsulation of photoresistive structures based on colloidal HgTe quantum dots by atomic layer deposition

© A. G. Medvedev[1], D. S. Kuzmichev[1], O. A. Saptsova[1], T. V. Koroleva[1], K. T. Khakimov[1], V. O. Yakovlev[1], V. P. Ponomarenko[1,2], and V. S. Popov[1,2,*]

[1] *Moscow Institute of Physics and Technology, Moscow Region, Dolgoprudny, 141701 Russia*
[*] *E-mail: popov.vs@mipt.ru*
[2] *RD&P Center ORION, JSC, Moscow, 111538 Russia*

Received 25.12.2025; revised 19.01.2026; accepted 20.02.2026

Colloidal quantum dots (CQDs) are a promising material for low-cost infrared photodetectors operating at room temperature. However, the formation of CQD based photosensitive layers is accompanied by the formation of surface defects and oxidation, which leads to the degradation of the devices' performance. In this study, we propose using atomic layer deposition (ALD) to efficiently encapsulate a mercury telluride (HgTe) CQD layer by depositing thin films of hafnium oxide (HfO_2) for the first time. The feasibility of applying the HfO_2 encapsulating layer is confirmed by studying the photoelectric characteristics of the manufactured photoresistors. It is shown that the protective coating reduce the dark current while maintaining the photoresistor's photoresponse under 1550 nm laser irradiation. The obtained results demonstrate the potential of ALD for creating stable and high-performance next-generation IR photodetectors.

Keywords: photosensor, mid-wave IR range, colloidal quantum dots, atomic layer deposition, encapsulation, hafnium oxide.

DOI: 10.51368/2949-561X-2026-1-18-23

Introduction

Infrared photodetectors based on colloidal quantum dots (CQDs) offer several advantages over traditional detectors (e.g., those based on InGaAs or MCT), due to the low cost and simplicity of CQD synthesis using wet chemistry methods, compatibility with CMOS technology, the potential for room-temperature operation, and the mechanical flexibility of the fabricated photosensitive layers on substrates [1–5]. The ability to tune the spectral characteristics of HgTe CQDs through the quantum confinement effect allows their absorption wavelength to be adjusted from the near-infrared to the far-infrared range. This is achieved by controlling the nanocrystal size during synthesis, making this material promising for the development of IR photodetectors [6]. However, despite the relative stability of HgTe CQDs, the process of fabricating photosensitive layers can lead to the formation of undesirable surface states and/or the slow degradation of the surface layer due to oxidation upon exposure to humid air [7–9]. Furthermore, changes in stoichiometry during post-synthetic treatment of the nanocrystals and device fabrication also lead to a sharp increase in trap states, deteriorating sensitivity and response speed.

One well-developed and effective method for producing thin films is atomic layer deposition (ALD), which involves sequential,

self-limiting chemical reactions [10–13]. During the ALD process, precursors alternately react with the surface multiple times, resulting in the reproducible growth of a thin film, one monolayer per cycle, even on substrates with complex geometries. The self-limiting nature of the surface reactions enables control at the atomic level. The ALD process was developed due to the need for high-quality dielectric and luminescent films to be deposited on large-area substrates [14]. ALD is used to deposit various types of thin films, including oxide (Al_2O_3, TiO_2, SnO_2, ZnO, HfO_2), nitride (TiN, TaN, WN, NbN), metal (Ru, Ir, Pt), and sulfide (ZnS) films for diverse applications in semiconductor microelectronics manufacturing [15–20], photovoltaic devices [21–25], energy storage devices [26–28], catalysts [29, 30], semiconductor gas sensors [31–34], optics and photonics [35–37], and many others [38]. However, the ALD method is relatively expensive, both in terms of the complexity of the equipment required and the high purity and quality demands for the precursors and substrates used.

In the context of infrared photodetectors based on colloidal quantum dots, ALD is used to deposit a passivating aluminum oxide film to improve stability during fabrication steps performed in air. For example, it is used to optimize the photosensitivity and stability parameters of detectors based on PbS and PbSe [39, 40] and HgTe [41].

This paper proposes using the ALD method to form a protective hafnium oxide (HfO_2) coating on an array of HgTe CQDs. The development of the ALD method has made the ability to deposit films at relatively low temperatures (below 150 °C) a competitive advantage, ensuring the stability of the surface layer of sensitive materials, including biological and organic samples. The encapsulation efficiency was monitored by measuring the photosensitive characteristics of the photoresistor: the dark current and the magnitude of the photoresponse under illumination by a 1550 nm light-emitting diode.

Experimental section

Synthesis of HgTe CQDs

HgTe CQDs were synthesized via the hot-injection method according to a previously described protocol [41] at a reaction temperature of 80 °C and a reaction time of 30 minutes to obtain CQDs of the desired size.

Fabrication method for the photoresistive structure

The CQDs were deposited onto a quartz substrate with interdigitated Au electrode patterns, employing intermediate layer-by-layer activation with a solution of ethanedithiol in hydrochloric acid and isopropanol (HCl:EDT:IPA = 1:1:20 by vol.) and rinsing with isopropyl alcohol.

Encapsulation method for the photoresistive structure

The HfO_2 film growth was carried out at a reactor chamber temperature of 90 °C using $Hf[N(CH_3)(C_2H_5)]_4$ (TEMAH) and H_2O as precursors. The TEMAH pulse duration into the reaction chamber was 0.5 s, followed by a 12 s purge. The water vapor pulse duration was 0.1 s, followed by a 12 s purge. The temperatures of the TEMAH and H_2O cylinders were maintained stable throughout the entire deposition process at 100 °C and 20 °C, respectively. The protective coating thickness (27 nm) and growth rate (~ 1.36 Å/cycle) were determined using an ellipsometer at a wavelength of 632 nm on a monitor sample of silicon with native oxide.

FTIR spectra were recorded using a Spectrum 100 FTIR spectrometer (PerkinElmer, USA) equipped with an attenuated total reflectance (ATR) accessory.

The current values of the photoresistor under pulsed illumination were recorded using a Keithley 2636B sourcemeter at a constant bias voltage U = 0.1 V. For pulsed illumination, a laser diode with fiber-coupled output at a wavelength of 1550 nm (power 8 mW) was used. The laser diode operated in a square-wave modulation mode (period 4 s, pulse duration 2 s) set by a FeelTech FeelElec FY6900 60M function generator. The radiation from the laser diode passed through a collimator and was then focused by a collecting silicon lens into a light spot approximately 300 μm in diameter onto the photosensitive area of the sample under study. All measurements were performed under ambient conditions in air.

Discussion of the results

The synthesis of HgTe CQDs was carried out using the hot-injection method via the reaction of mercury chloride with a solution of tellurium in trioctylphosphine. The absorption peak maximum of the CQDs synthesized at 80 °C with a nanocrystal growth time of 30 minutes, as determined by FTIR spectroscopy, was 2.83 μm with a full width at half maximum (FWHM) of 0.4 μm (Fig. 1), indicating a relatively narrow size distribution of the mercury telluride nanocrystals. Varying the synthesis time and the nature of the mercury and chalcogenide precursors allows control over the spectral characteristics of CQDs based on mercury chalcogenides [42–44]. The photoresistor was fabricated by layer-by-layer spin-coating of HgTe CQD films from a dispersion. During this process, the layer surface was treated with an ethanedithiol solution to replace the long-chain oleylamine ligands on the CQD surface, which is a recognized approach for tuning the spectral characteristics of CQDs and reducing the number of surface traps [45, 46].

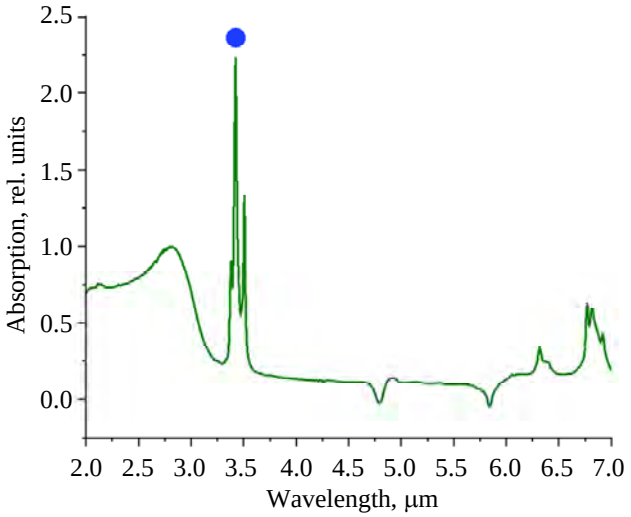

Fig. 1. IR spectrum of HgTe CQDs obtained at a synthesis temperature of 80 ℃ and time of 30 min. The dot marks the position of the peak corresponding to C-H stretching vibrations of the ligand shell

Storage of the photoresistor structure in air leads to changes in the photosensing characteristics. For instance, exposure for 15 days results in an increase in dark current at contacts with an interelectrode distance of 10 μm from 1.62×10^{-4} to 3.63×10^{-4} A, while measurements at contacts with an interelectrode distance of 2120 μm show the dark current increasing from 5.22×10^{-8} to 1.09×10^{-7} A. The photoresponse amplitude, calculated as the difference between the current under 1550 nm laser illumination and the dark current, increased from 2.88×10^{-7} to 2.18×10^{-6} A upon storage for 15 days at contacts with a short interelectrode distance, and decreased from 5.79×10^{-10} to 3.47×10^{-10} A when measured at contacts with a long interelectrode distance. This is apparently related to the possible formation of surface traps caused by adsorption and chemical interaction with oxygen and water. The observed changes in characteristics demonstrate the relatively low stability of the sample. Due to the change in photosensitive characteristics, encapsulation of the photoresistor structure with a thin hafnium oxide film is proposed.

Encapsulation of the photoresistor with a hafnium oxide film was carried out at a relatively low reactor chamber temperature of 90° [47]. The protective coating thickness was 27 nm. The effectiveness of this approach was investigated by comparative analysis of the dark current values, the shape of the photosignal rise and decay, and the photosignal amplitude before and after applying the hafnium oxide protective coating under 1550 nm laser irradiation. Encapsulation leads to a reduction in the dark current to 5.47×10^{-5} A and 1.38×10^{-8} A when measured at contacts with interelectrode distances of 10 μm and 2120 μm, respectively. At the same time, the photoresponse amplitude decreased slightly to 9.69×10^{-7} A and 2.10×10^{-10} A, respectively.

Fig. 2 shows the photoresponse waveforms upon illumination of the structure with a 1550 nm laser after fabrication, after 15 days of exposure to air, and after encapsulation with a thin hafnium oxide film. It should be noted that the measurement results are presented without background subtraction. Encapsulation of the structure leads to a sharp reduction in dark current drift, while a rapid rise of the photosignal to a steady-state value is observed (Fig. 2*c*), whereas the sample before encapsulation was characterized by a strong dark current drift (Fig. 2*a*, *b*) and a slow equilibration of the photosignal. Furthermore, the absence of a slow signal decay region after encapsulation should be

noted, compared to the freshly prepared structure and the structure stored in air for 15 days.

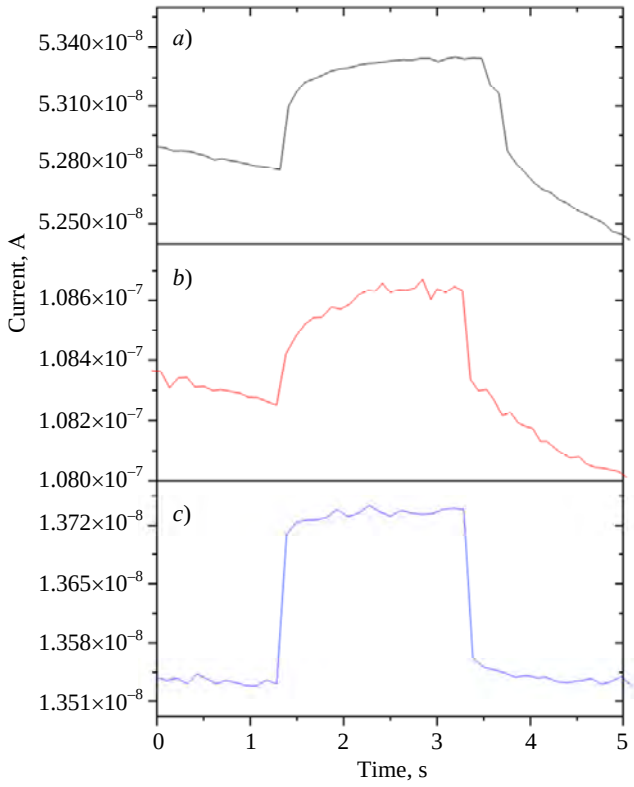

Fig. 2. Photoresponse of the photoresistive structure upon illumination with a 1550 nm laser diode: freshly prepared structure (a), after storage in air for 15 days (b), and after deposition of a hafnium oxide film (c)

Despite the need for additional, more in-depth studies, these preliminary results demonstrate the effectiveness of encapsulating CQD photoresistive structures with a thin hafnium oxide film deposited by ALD at a relatively low temperature. This opens up broad possibilities for reducing dark current and improving stability in the fabrication of photosensitive layers for IR photodetectors based on CQDs.

Conclusion

HgTe colloidal quantum dots with an absorption peak maximum at 2.83 μm were obtained via the hot-injection method. A photoresistive structure based on these dots was fabricated on gold interdigitated electrodes. The effectiveness of encapsulating the obtained structure with a thin protective hafnium oxide film deposited by ALD at a relatively low temperature of 90 °C is demonstrated. The deposition of the hafnium oxide film leads to a decrease in dark current values, preservation of the photoresponse magnitude, reduction of dark current drift, and acceleration of signal decay upon illumination of the structure with a 1550 nm laser diode. The obtained data indicate the potential of using low-temperature ALD for producing thin encapsulating hafnium oxide films in IR photodetectors based on colloidal quantum dots of various metal chalcogenides.

This work was supported by the Ministry of Science and Higher Education of the Russian Federation (Project No. FSMG-2025-0024).

REFERENCES

1. Ponomarenko V. P., Popov V. S., Shuklov I. A., Ivanov V. V., and Razumov V. F., Russ. Chem. Rev. **93** (4), RCR5113 (2024).
2. Kim D., Si M.-J., Kim J., Jung Y., and Baek S.-W., Adv. Opt. Mater. e02859 (2025).
3. Yu L., Tian P., Liang K., Yu L., Tian P., and Liang K., Quantum Beam Sci. **9** (1), 9 (2025).
4. Ponomarenko V. P., Popov V. S., Pankov M. A., et al., Applied Physics, № 1, 45–54 (2025) [in Russian].
5. Ponomarenko V. P., Popov V. S., Pankov M. A., et al., Applied Physics, № 2, 12–20 (2025) [in Russian].
6. Sergeeva K. A., Zhang H., Portniagin A. S., et al., Adv. Funct. Mater. **34** (39) 2405307 (2024).
7. Dou H., Yuan C., Zhu R., Li L., Zhang J., and Weng T. C., Nanomaterials **14** (1), 34 (2024).
8. Kahmann S. and Loi M. A., Appl. Phys. Rev. **7** (4) 041305 (2020).
9. Giansante C. and Infante I., J. Phys. Chem. Lett. **8** (20), 5209–5215 (2017).
10. Kol'tsov S. I., J. Appl. Chem. USSR **38**, 1352 (1965).
11. Malygin A. A., Drozd V. E., Malkov A. A., and Smirnov V. M., Chem. Vapor Depos. **21** (10-12), 216–240, (2015).
12. Puurunen R. L., Chem. Vapor Depos. **20** (10-12), 332–344 (2014).
13. Parsons G. N., Elam J. W., George S. M., Haukka S., Jeon H., Kessels W. M. M., Leskelä M., Poodt P., Ritala M., and Rossnagel S. M., J. Vac. Sci. Technol. A **31** (5), 050818 (2013).

14. Suntola T., Mater. Sci. Rep. **4** (5), 261–312 (1989).
15. Ovanesyan R. A., Filatova E. A., Elliott S. D., Hausmann D. M., Smith D. C., and Agarwal S., J. Vac. Sci. Technol. A **37**, 060904 (2019).
16. Kim S. E., Sung J. Y., Yun Y., Jeon B., Moon S. M., Lee H., Lee C. H., Jung H. J., Lee J. U., and Lee S. W., Curr. Appl. Phys. **64**, 8–15 (2024).
17. Choi A. R., Lim D. H., Shin S. Y., Kang H. J., Kim D., Kim J. Y., Ahn Y., Ryu S. W., and Oh I. K., Chem. Mater. **36** (5), 2194–2219 (2024).
18. O'Brien K. P., Naylor C. H., Dorow C., et al., Nat. Commun. **14** (1), 6400 (2023).
19. Chernikova A. G., Sizykh N. A., Zabrosaev I. V., and Markeev A. M., Surf. Interfaces **62**, 106135 (2025).
20. Koroleva A. A., Kuzmichev D. S., Kozodaev M. G., Zabrosaev I. V., Korostylev E. V., and Markeev A. M., Appl. Phys. Lett. **122** (2), 022905 (2023).
21. Niu W., Li X., Karuturi S. K., Fam D. W., Fan H., Shrestha S., Wong L. H., and Tok A. I. Y., Nanotechnol. **26** (6), 064001 (2015).
22. Van Delft J. A., Garcia-Alonso D., and Kessels W. M. M., Semicond. Sci. Technol. **27** (7), 074002 (2012).
23. Zardetto V., Williams B. L., Perrotta A., Di Giacomo F., Verheijen M. A., Andriessen R., Kessels W. M. M. and Creatore M., Sustain. Energy Fuels **1** (1) 30–55 (2017).
24. Dingemans G. and Kessels W. M. M., J. Vac. Sci. Technol. A **30** (4), 040802 (2012).
25. Zaera F., Chem. Soc. Rev. **42** (7), 2746–2762 (2013).
26. Hu Y., Miikkulainen V., Mizohata K., Norby T., Nilsen O., and Fjellvåg H., Electrochim. Acta **361**, 137019 (2020).
27. Put B., Mees M. J., Hornsveld N., Hollevoet S., Sepúlveda A., Vereecken P. M., Kessels W. M. M., and Creatore M. J., Electrochem. Soc., **166** (6), A1239 (2019).
28. Kozen A. C., Pearse A. J., Lin C. F., Noked M., and Rubloff G. W., Chem. Mater. **27** (15), 5324–5331 (2015).
29. Oneill B. J., Jackson D. H. K., Lee J., Canlas C., Stair P. C., Marshall C. L., Elam J. W., Kuech T. F., Dumesic J. A., and Huber G. W., ACS Catal. **5** (3), 1804–1825 (2015).
30. Woo Shim J., Seok Lee Y., Sung Choi Y., Henke T., Knaut M., Hossbach C., Mane A. U., Tong W. M., Brodie A. D., Mackus A. J., Weber M. J., Thissen N. F., Garcia-Alonso D., Vervuurt R. H., Assali S., Bol A. A., Verheijen M. A., and Kessels W. M., Nanotechnol. **27** (3), 034001 (2015).
31. Mokrushin A. S., Dmitrieva S. A., Gorban Y. M., Stroikova A. R., Simonenko N. P., Averin A. A., and Simonenko E. P., Russ. J. Inorg. Chem. **70**, 624–632 (2025).
32. Mokrushin A. S., Simonenko E. P., Simonenko N. P., Akkuleva K. T., Antipov V. V., Zaharova N. V., Malygin A. A., Bukunov K. A., Sevastyanov V. G., and Kuznetsov N. T., Appl. Surf. Sci. **463**, 197–202 (2019).
33. Pan H., Zhou L., Zheng W., Liu X., Zhang J., and Pinna N., Int. J. Extreme Manufact. **5** (2), 022008 (2023).
34. Cho B., Hahm M. G., Choi M., Yoon J., Kim A. R., Lee Y. J., Park S. G., Kwon J. D., Kim C. S., Song M., Jeong Y., Nam K. S., Lee S., Yoo T. J., Kang C. G., Lee B. H., Ko H. C., Ajayan P. M., and Kim D. H., Sci. Rep. **5** (1), 8052 (2015).
35. Leskelä M., Mattinen M., and Ritala M., J. Vac. Sci. Technol. B **37**, 030801 (2019).
36. He G., Zhu L., Sun Z., Wan Q., and Zhang L., Prog. Mater. Sci., **56** (5), 475–572 (2011).
37. Voitsekhovskii A. V., Dzyadukh S. M., Gorn D. I., Dvoretskii S. A., Mikhailov N. N., Sidorov G. Yu., and Yakushev M. V., Applied Physics, № 5, 15–24 (2025) [in Russian].
38. Kessels E., Devi A., Park J. S., Ritala M., Yanguas-Gil A., and Wiemer C., Nat. Rev. Methods Primers **5**, 66 (2025).
39. Hu C., Gassenq A., Justo Y., Devloo-Casier K., Chen H., Detavernier C., Hens Z., and Roelkens G., Appl. Phys. Lett. **105** (17), 171110 (2014).
40. Liu Y., Tolentino J., Gibbs M., Ihly R., Perkins C. L., Liu Y., Crawford N., Hemminger J. C., and Law M., Nano Lett. **13** (4), 1578–1587 (2013).
41. Malachosky E. W., Ackerman M. M., and Stan L., Nanomaterials **14** (16), 1354 (2024).
42. Shuklov I. A., Milenkovich T., Majorova A. V., Vershinina O. V., Ivanova V. A., Pavlova V. D., and Popov V. S., J. Comm. Tech. Electron. **70** (2), 61–67 (2025).
43. Shuklov I. A., Milenkovich T., Vershinina O. V., Dubrovina N. V., Saptsova O. A., Popov V. S., and Ivanov V. V., Applied Physics, № 3, 34–41 (2025) [in Russian].
44. Popov V. S., Milenkovich T., Khakimov K. T., Koroleva T. V., Deomidov A. D., Davletshin R. V., Khamidullin K. A., Saptsova O. A., Yakovlev V. O., Shuklov I. A., Koronnov A. A., Egorov A. V., and Ponomarenko V. P., J. Comm. Tech. Electron. **70** (6), 278–282 (2025).
45. Brown P. R., Kim D., Lunt R. R., Zhao N., Bawendi M. G., Grossman J. C., and Bulović V., ACS Nano **8**, 5863–5872 (2014).
46. Shuklov I. A., Dyomkin D. V., Konavicheva V. A., Popov V. S., and Razumov V. F., J. Comm. Tech. Electron. **68** (S2), S184–S189 (2023).
47. Chernikova A. G., Kuzmichev D. S., Negrov D. V., Kozodaev M. G., Polyakov S. N., and Markeev A. M., Appl. Phys. Lett. **108** (24), 242905 (2016).

About authors

Medvedev Alexander Gennadyevich, Candidate of Chemical Sciences, Deputy Laboratory Head, Senior Researcher, Moscow Institute of Physics and Technology (9 Institutskiy per., Moscow Region, Dolgoprudny, 141701, Russia). E-mail: medvedev.ag@mipt.ru SPIN-code: 3699-6664, AuthorID: 822022, ORCID 0000-0002-6762-004X

Kuzmichev Dmitry Sergeevich, Candidate of Physical and Mathematical Sciences, Senior Researcher, Moscow Institute of Physics and Technology (9 Institutskiy per., Moscow Region, Dolgoprudny, 141701, Russia). E-mail: kuzmichev.ds@mipt.ru SPIN-code: 3865-0101, AuthorID: 822752, ORCID 0000-0002-8901-5051

Saptsova Olga Alexandrovna Junior Researcher, Moscow Institute of Physics and Technology (9 Institutskiy per., Moscow Region, Dolgoprudny, 141701, Russia). E-mail: saptsova.oa@mipt.ru SPIN-code: 3710-5884, AuthorID: 1323937, ORCID 0009-0008-5445-4629

Koroleva Taisiya Viktorovna, Junior Researcher, Moscow Institute of Physics and Technology (9 Institutskiy per., Moscow Region, Dolgoprudny, 141701, Russia). E-mail: koroleva.tv@mipt.ru SPIN-code: 6991-6170, AuthorID: 1292280, ORCID 0000-0003-0792-1948

Khakimov Karim Timurovich, Junior Researcher, Moscow Institute of Physics and Technology (9 Institutskiy per., Moscow Region, Dolgoprudny, 141701, Russia). E-mail: khakimov.kt@mipt.ru SPIN-code: 8812-6012, AuthorID: 1209525, ORCID 0000-0001-8133-6128

Yakovlev Viktor Olegovich, Junior Researcher, Moscow Institute of Physics and Technology (9 Institutskiy per., Moscow Region, Dolgoprudny, 141701, Russia). E-mail: iakovlev.vo@mipt.ru SPIN-code: 3324-6931, AuthorID: 1290912, ORCID 0009-0009-3507-082X

Ponomarenko Vladimir Pavlovich, Doctor of Physical and Mathematical Sciences, Chief Designer, Head of Department, Professor, Moscow Institute of Physics and Technology (9 Institutskiy per., Moscow Region, Dolgoprudny, 141701, Russia); RD&P Center ORION, JSC (9 Kosinskaya st., Moscow, 111538, Russia). E-mail: 2392325@gmail.com SPIN code: 6882-8721, AuthorID: 171358

Popov Viktor Sergeevich, Candidate of Chemical Sciences, Head of Laboratory, Leading Researcher, Moscow Institute of Physics and Technology (9 Institutskiy per., Moscow Region, Dolgoprudny, 141701, Russia) Associate Professor, RD&P Center ORION, JSC (9 Kosinskaya st., Moscow, 111538, Russia). E-mail: popov.vs@mipt.ru SPIN-code: 1128-2332, AuthorID: 625948, ORCID 0000-0002-0962-9775

PHOTOELECTRONICS

UDC 621.383
EDN: ETSFPH
PACS: 42.79.Pw, 85.60.Gz, 07.57.Kp

Efficiency of applying a high-pass filter cutoff frequency corrector used in the infrared focal-plane array with time delay integration mode (IR-FPA)

© V. V. Abilov, V. A. Streltsov, and V. V. Savtsov*

RD&P Center ORION, JSC, Moscow, 111538 Russia
** E-mail: vlvsav@yandex.ru*

Received 26.12.2025; revised 27.01.2026; accepted 20.02.2026

The fundamental design of the readout integrated circuit (ROIC) of scanning infrared (IR) photomodules (PM) with the time delay integration mode (TDI) is considered. The role and influence of the recursive high-pass filter (HPF) in the input cells (IC) of the readout integrated circuit on the threshold characteristics of the PM are outlined. A mathematical description of the digital correction of the HPF cutoff frequency in the input cell is given. The design and operating principle of a trainable classifier capable of dividing TDI-channels into groups based on the noise power spectral density (NPSD) are described. The cutoff frequency of the HPF of the IC has been corrected for a large number of TDI-channels with different NPSD. The efficiency of applying this correction to increase the signal-to-noise ratio has been calculated, taking into account the standard intra-frame processing for scanning IR PM. It was found that threshold characteristics without window filtering improve by an average of 2.5 %, while with it, they improve by only 1 %. It was noted that with a large number of TDI-channels with low-frequency noise, the digital correction of the HPF cutoff frequency can degrade threshold characteristics by 1.5 %.

Keywords: threshold characteristics, photomodule, infrared range, time delay and integration mode, noise, signal-to-noise ratio, intra-frame processing, noise power spectral density, high-pass filter, cutoff frequency, multi-label classification.

DOI: 10.51368/2949-561X-2026-1-24-30

Introduction

Large-format infrared focal plane arrays (IR FPAs) with time delay and integration (TDI) mode are actively used as part of Earth remote sensing space systems. The key element of such IR FPAs are infrared photomodules (PMs), which are large-scale integration (LSI) readout circuits hybridized with a matrix of photosensitive elements (MPE) based on cadmium mercury telluride. A typical block diagram of the LSI readout circuit for such PMs is shown in Fig. 1.

The task of the LSI readout circuit is to receive signals from the MPE, which is connected to the LSI via microcontacts (Fig. 1, block 1), and to sum these signals in a specific time sequence, i.e., to implement the TDI mode.

When the image is uniformly moved by the scanner across the photomodule, signals are sequentially transferred from the photosensitive elements (from 1 to 6) to the input cells (IC) of the LSI readout circuit. Primary integration and high-pass filtering of the signals are performed in these cells using switched-capacitor circuits (Fig. 1, block 2). High-pass filtering increases the input dynamic range by subtracting the spread of the constant non-informative component of the signals from the MPE. These signals are then switched to each of the inputs (from 1 to 1152) of the TDI register (Fig. 1, block 3). In the TDI register, weighted summation of the terms (signals) arriving at different times is performed. The operation of the TDI register is considered complete when all 6 signals are applied to its

inputs with equal weighting coefficients of 1/6. In this case, the operation of the TDI register can be considered as an averaging operation. The purpose of this averaging is a significant reduction in noise and interference levels, an improvement in the uniformity and stability of signals from the MPE, as well as an increase in the dynamic range at the output.

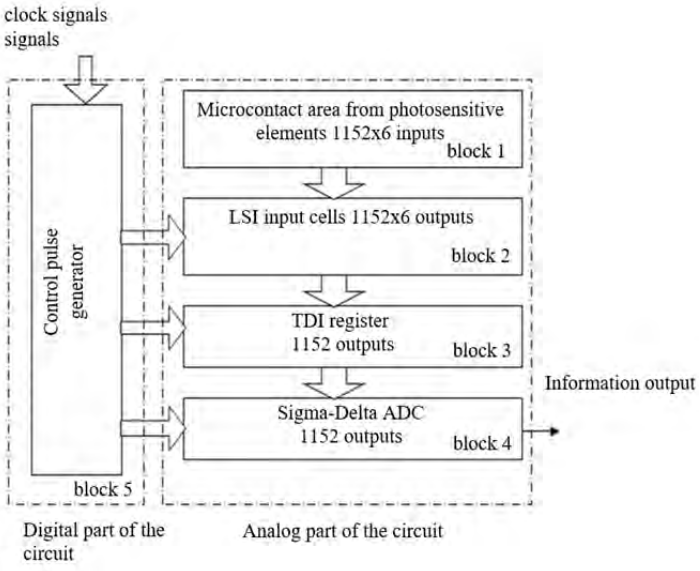

Fig. 1. Typical block diagram of the LSI readout circuit for scanning IR PMs

Further operations performed in block 4 (see Fig. 1) include:

- analog-to-digital conversion (ADC);
- switching signals to the information outputs of the LSI.

Coordination of the LSI operation and rejection of defective photosensitive elements are carried out by the digital control pulse generator block (Fig. 1, block 5) [1].

Since low-frequency noise significantly degrades the accuracy of measuring the signal obtained at the output of the IR FPA [2], given that the predominant part of the power spectral density of the signal from small-sized objects, which are the target detection objects for the considered IR FPAs, is concentrated in the low-frequency region, the idea naturally arises of the need to adjust the cutoff frequency f_{cutoff} of the high-pass filter of the LSI readout circuit input cells (hereinafter referred to as the SC filter) (Fig. 1, block 2) downwards. Conducting research on the selection of optimal parameters for a mathematical recursive filter, which ensures a reduction of the initial cutoff frequency of the SC filter from 120 Hz to 30 Hz, described in [3], showed a significant increase in the signal-to-noise ratio (up to 9 % for a first-order filter and up to 39 % for a second-order filter). However, in that study, parameter selection was carried out for only one TDI channel, which had a noise spectrum close to "white", although it was noted in the same work [3] that a real IR FPA contains a large number of TDI channels with a non-"white" noise spectrum, for which the filtering efficiency differs significantly. In this regard, it becomes relevant to conduct a study of the dependence of the effectiveness of adjusting the cutoff frequency of the LSI readout circuit high-pass filter in the context of increasing the signal-to-noise ratio, for a large number of TDI channels with different distributions of the noise power spectral density (NPSD), which is the subject of this work.

Cutoff frequency correction

The procedure for correcting the cutoff frequency of the SC filter involves applying a combination of two first-order recursive digital filters to the output images of the IR FPA. These filters first flatten the amplitude-frequency response (F1), after which it is subjected to high-pass filtering (F2), but now with the new required cutoff frequency (Fig. 2). The frequency response of the resulting filter (F) (red curve) is calculated as the product of the frequency responses of F1 and F2. The frequency response of the SC filter corrected using Filter is shown by the purple curve ("Resulting FR" in Fig. 2).

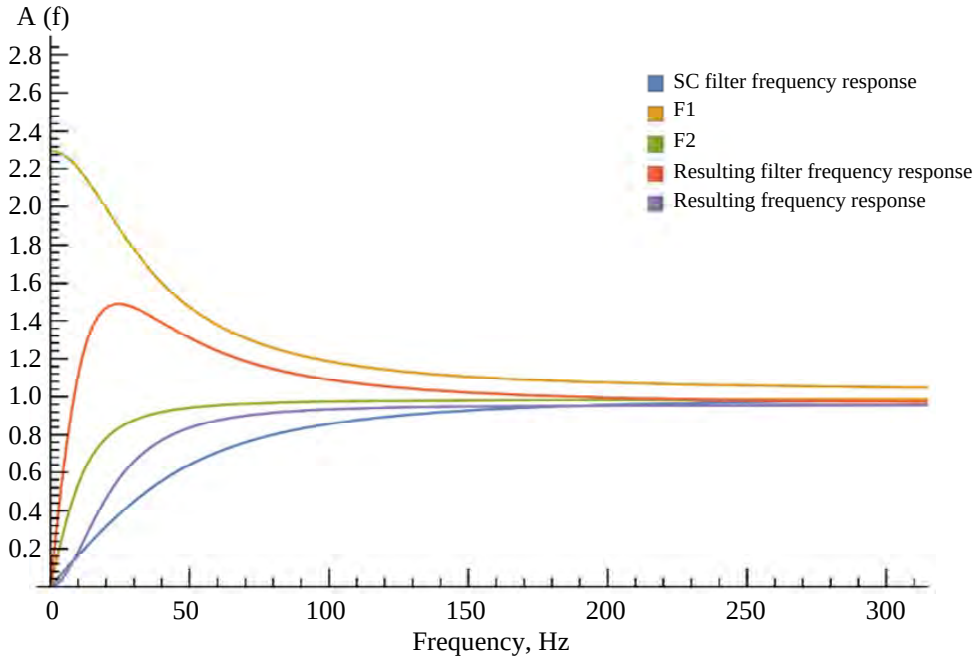

Fig. 2. Amplitude-frequency characteristics of the original SC filter, low-pass filter (F1), high-pass filter with the new cutoff frequency (F2), the resulting second-order filter (F), and the output data after the performed correction (Resulting FR)

A first-order recursive filter is described by the formula:

$$y[n] = a_0 x[n] + a_1 x[n-1] + b_1 y[n-1], \quad (1)$$

coefficients of the low-pass filter F1: $a_0 = 1.061906$, $a_1 = -0.95238$, $b_1 = +0.95238$;

coefficients of the high-pass filter F2: $a_0 = +\alpha$, $a_1 = -\alpha$, $b_1 = +\alpha$, $\alpha = 0.975$.

The resulting second-order filter F is defined by the formula:

$$y[n] = a_0 x[n] + a_1 x[n-1] + a_2 x[n-2] + \\ + b_1 y[n-1] + b_2 y[n-2] \quad (2)$$

with the following coefficients:
$a_0 = 0.975$, $a_1 = -1.84944$, $a_2 = 0.874438$, $b_1 = 1.92738$, $b_2 = -0.928571$.

After performing such frequency correction, the signal from a small-sized object increases, since the majority of its power spectral density is concentrated precisely in the low-frequency region. Noise also increases, however, in the case of uniform or high-frequency noise, this increase is not proportional to the increase in the signal, as a result of which the signal-to-noise ratio increases and the threshold characteristics improve. But if low-frequency noises predominate among the TDI channels, such processing may either be ineffective or worsen the threshold characteristics.

NPSD classifier for TDI channels

To determine the effectiveness of correcting the SC filter cutoff frequency for various types of NPSD, it is necessary to classify a large number of TDI channels into four main noise classes described in [4] (elementary classes):

1) noise of standard TDI channels ("White");

2) noise with a predominant high-frequency component (high-frequency);

3) noise with excessive low-frequency components (low-frequency);

4) noise with a rise in the vicinity of 1/3 of the sampling frequency (TDI noise).

For automatic identification of the NPSD, a trainable classifier was developed, which makes it possible to determine the probability of a TDI channel belonging to one of the above groups.

The input data for the classifier are the frequency dependencies of the NPSD of the TDI channels, which have undergone preliminary digital processing carried out in 3 stages [5]:

1) window filtering using the median function in a window of radius 2;

2) window filtering using the arithmetic mean function in a window of radius 5;

3) normalization – ensuring that the mean value of the data is equal to one.

Based on the data obtained after preprocessing, 3 coefficients ($x1$, $x2$, $x3$) are calculated, each of which characterizes the belonging of the TDI channel to one of the groups:

1) The slope coefficient in the low-frequency region is defined as the slope coefficient of a straight line constructed using the least squares method (LSM) from data in the region [50; 500] Hz.

2) The slope coefficient in the main part of the NPSD is defined as the slope coefficient of a straight line constructed using LSM from data in the regions [500; 1177] ∪ [1377; 1915] Hz.

3) The coefficient characterizing TDI noise is determined as follows: from the data in the region Δ = [1177; 1377] Hz, the coefficients of an approximating parabola are calculated using LSM. After that, depending on the value of the coefficient in front of the highest degree of the parabola (a), the value of the TDI noise coefficient is determined:

a) if $a > 0$, then the parameter is 0;

b) if $a < 0$ and the position of the parabola's maximum is outside the range of region Δ, then the parameter is 0;

c) otherwise, the parameter is equal to the value of the correlation coefficient of the data from region Δ with the sampled approximating parabola.

The classifier is trained by calculating the characteristic NPSD coefficients for which the class has been manually determined, and constructing probability density functions for each class based on them (Fig. 3):

1) For each elementary class C_k (white, high-frequency, low-frequency, TDI; k – parameter index) and for each characteristic coefficient x, the distribution width is estimated as the median absolute deviation, reduced to the RMS value – $\sigma_{k,x}$.

2) For each elementary class C_k and for each coefficient x, a distribution density of this coefficient is formed: the final density value $\rho_{k,x}$ is the sum of Gaussians with a mean equal to the parameter value and an RMS equal to $\sigma_{k,x} \times n$, $n = 1/4$.

3) The obtained distribution densities are normalized: $\int_{-\infty}^{\infty} \rho_{k,x}(x)\,dx = 1$.

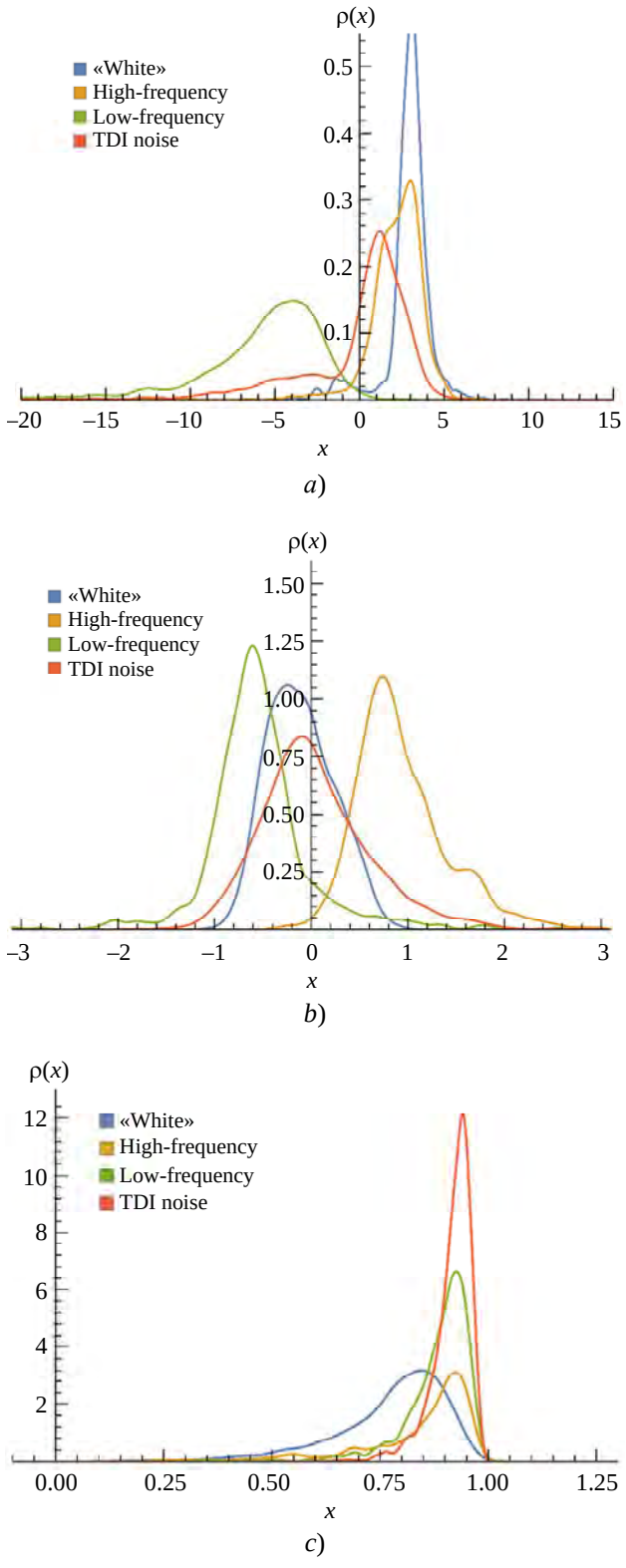

Fig. 3. Probability density functions of each elementary NPSD class: a) for the low-frequency noise slope coefficient, b) for the slope coefficient of the main part of the NPSD, c) for the correlation coefficient of the preprocessed data and the approximating parabola

After calculating the characteristic coefficients of the classified NPSD, the probability of its belonging to one of the elementary classes is calculated using the Bayes formula [6]:

$$P(C_k \mid \vec{x}) = \frac{P(C_k) \cdot P(\vec{x} \mid C_k)}{P(\vec{x})}, \qquad (3)$$

where $\vec{x} = (x_1\, x_2\, x_3)^T$ is the vector with parameter values (coefficients);

$P(C_k)$ is the probability of encountering an elementary class C_k;

$P(\vec{x} \mid C_k)$ is the probability that the value of the coefficient vector equals $\vec{x}$ given that the input data belongs to class C_k.

The prior probability of hypothesis C_k is calculated by the formula:

$$P(C_k) = N_k / N \qquad (4)$$

where N_k is the number of samples in which elementary class k was observed among the training set;

N is the total number of training samples.

Due to the independence of the coefficients from each other, the conditional probability of observing the coefficients $\vec{x}$ given that they belong to the elementary class C_k is calculated by the formula:

$$P(\vec{x}|C_k) = \prod_{i=1}^{3} \int\limits_{|\xi_i - x_i| \le \sigma_i \cdot n} \rho_k(\xi_i)\, d\xi_i. \qquad (5)$$

The probability $P(\vec{x})$ is calculated using the formula for the total probability of an event dependent on several mutually exclusive hypotheses:

$$P(\vec{x}) = \sum_{k=1}^{4} P(\vec{x} \mid C_k) \cdot P(C_k). \qquad (6)$$

Efficiency of applying the SC filter cutoff frequency corrector for TDI channels with different NPSDs

Using the developed classifier, 5760 TDI channels from a single line of a scanning IR FPA sample were divided into groups. Using the NPSD of these TDI channels, time-domain noise realizations with a length of 1937 samples were generated for each of the channels, thus forming a frame that simulates the output low-background image of the IR FPA. Using the noise frame as a basis, a series of frames is formed, each of which represents a superposition of the time-domain noise realizations and the image of a small-sized object focused on one of the TDI channels.

The resulting series of frames is simultaneously subjected to two digital processing methods: standard processing (two-point correction and window filtering quasi-matched to the signal from the small-sized object [7]) and sequentially applied cutoff frequency correction followed by standard processing. From the processed frames, the signal-to-noise ratio (SNR) is calculated for each TDI channel, after which the ratio of the SNR values obtained from the series of frames subjected to standard processing with the cutoff frequency corrector to the SNR values obtained from the series of frames subjected only to standard processing is found. The values of these ratios characterize the effectiveness of applying the SC filter cutoff frequency correction to improve the threshold characteristics of each individual TDI channel, given their mutual arrangement in the line (due to window filtering).

Having information about which NPSD shape group each TDI channel belongs to, it is possible to correlate the effectiveness of applying the SC filter cutoff frequency correction with the noise spectrum and its prevalence in a real sample of a scanning IR FPA (Fig. 4).

The obtained results show that the application of the corrective filter:

a) for "white" noise increases the SNR by 1 %;

b) for high-frequency noise increases the SNR by 2 %;

c) for low-frequency noise decreases the SNR by 1.5 %;

d) for TDI noise increases the SNR by 1.3 %.

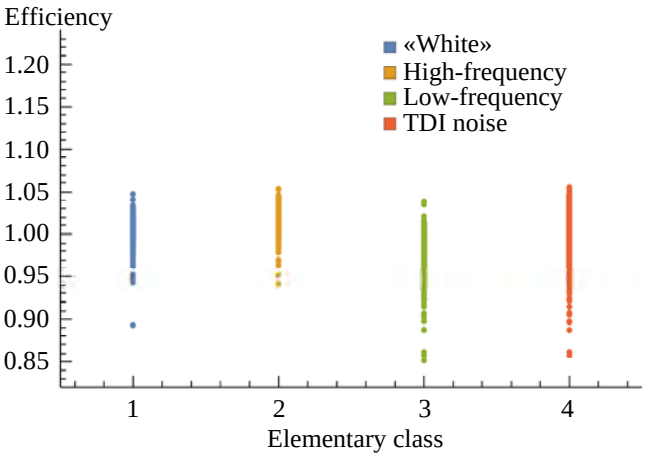

Fig. 4. Efficiency of applying SC filter cutoff frequency correction for various NPSD types considering quasi-matched window filtering

However, if window filtering of the output images is not performed, limiting standard processing to only two-point correction, then the efficiency of applying the SC filter cutoff frequency correction will be distributed as shown in Fig. 5.

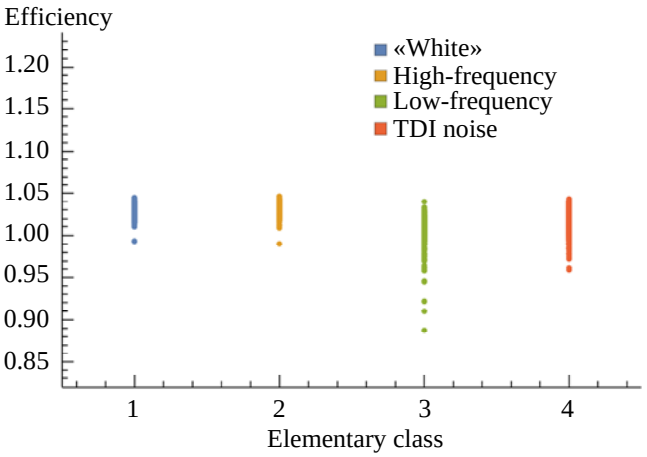

Fig. 5. Efficiency of applying SC filter cutoff frequency correction for various NPSD types without considering quasi-matched window filtering

In this case, the application of the corrective filter:

a) for "white" noise increases the SNR by 3 %;

b) for high-frequency noise increases the SNR by 3 %;

c) for low-frequency noise increases the SNR by 1 %;

d) for TDI noise increases the SNR by 2.3 %.

Summarizing the obtained results, it can be concluded that the efficiency of the SC filter cutoff frequency correction on average slightly improves the threshold characteristics (up to 2.5 %), if they are evaluated from the original output images of the IR FPA. However, due to the "blurring" of time samples between TDI channels when applying window filtering, which is often used for the same purpose of improving threshold characteristics, this effect is practically negated (down to 1 %). Also, in the case of predominance of low-frequency noise in the photomodule, correction of the SC filter cutoff frequency can worsen its threshold characteristics (up to 1.5 %), which indicates the high specificity of this type of preprocessing of IR FPA output signals.

Conclusion

In this paper, a study was conducted on the influence of the shape of the noise power spectral density of IR FPA TDI channels on the efficiency of correcting the cutoff frequency of the LSI readout circuit high-pass filter in the context of increasing the signal-to-noise ratio, given the application of standard intraframe digital processing, which includes two-point correction of the sensitivity non-uniformity of the TDI channels and window filtering quasi-matched to the signal from a small-sized object. To determine whether the NPSD plots of TDI channels belong to one of the four main types, a trainable classifier was developed, which makes it possible, based on manually classified data, to calculate the probability of the classified TDI channel belonging to one or several groups at once. Using the classifier, a large number of TDI channels from a real sample of a scanning IR FPA were identified, after which, using their NPSD, a series of frames was generated containing images of a small-sized object on each of the studied TDI channels. After parallel intraframe processing of these frames with and without SC filter cutoff frequency correction, a comparison was made of the effectiveness of this correction for improving threshold characteristics for various types of TDI channels:

a) in the case of applying window filtering,

correction of the SC filter cutoff frequency on average increases the SNR by 1 %;

b) in the case without applying window filtering, correction of the SC filter cutoff frequency on average increases the SNR by 2.5 %.

It was also shown that in the case of predominance of TDI channels with low-frequency noise in the photomodule, correction of the SC filter cutoff frequency reduces the SNR by 1.5 %, which, together with the low efficiency when applying window filtering, indicates the high specificity of this type of preprocessing of IR FPA output signals and the impossibility of using it without a preliminary assessment of the noise characteristics of the device used. In the case of predominance of noise with a uniform or high-frequency spectrum in the device, this correction allows a slight improvement in threshold characteristics, which is nevertheless a satisfactory result for this type of IR FPA.

REFERENCES

1. Bochkov V. D., Drajnicov B. N., Kuznetsov P. A., Kozlov K. V., and Solyakov V. N., Usp. Prikl. Fiz. (Advances in Applied Physics) **2** (1), 65–70 (2014) [in Russian].
2. Deomidov A. D., Kozlov K. V., Polesskiy A. V., Solomonova N. A., and Firsenkova U. A., Applied Physics, № 4, 102–108 (2015) [in Russian].
3. Streltcov V. A., Abilov V. V., and Filippov S. O., Usp. Prikl. Fiz. (Advances in Applied Physics) **7** (3), 267–276 (2019) [in Russian].
4. Abilov V. V. and Streltsov V. A., Applied Physics, № 3, 55–62 (2023) [in Russian].
5. Press W. H., et al. Numerical Recipes: The Art of Scientific Computing. 3er ed. Cambridge University Press, 2007.
6. Zhang M.-L., Pena Jos´e M., and Robles Victor, Information Sciences **179** (19), 3218–3229 (2009).
7. Drajnicov B. N., Kuznetsov P. A., Kozlov K. V., and Solyakov V. N., Usp. Prikl. Fiz. (Advances in Applied Physics) **3** (6), 566–572 (2015) [in Russian].

About authors

Abilov Vladislav Vladimirovich, Candidate of Technical Sciences, Chief Specialist, RD&P Center ORION, JSC (9 Kosinskaya st., Moscow, 111538, Russia). E-mail: Abilov.V.V.@yandex.ru SPIN code: 2756-7990, AuthorID: 1233856

Streltsov Vadim Alexandrovich, Engineer of the 1st Category, RD&P Center ORION, JSC (9 Kosinskaya st., Moscow, 111538, Russia). E-mail: vadim.streltsov@phystech.edu SPIN code: 7411-5614, AuthorID: 1242995

Savtsov Vladimir Valeryevich, Head of Department, RD&P Center ORION, JSC (9 Kosinskaya st., Moscow, 111538, Russia). E-mail: vlvsav@yandex.ru

PLASMA PHYSICS AND PLASMA METHODS

UDC 53.043, 533.9.072
EDN: GSQONW
PACS: 33.20.Ni; 52.50.Dg; 52.77.−j; 61.30.Hn

Effect of non-equilibrium atmospheric plasma on the hydrophilicity of metal surfaces

© D. V. Beloplotov[1,*], V. S. Skakun[1], D. A. Sorokin[1,2], E. A. Sosnin[1,2], V. A. Panarin[1], and B. A. Zaitsev[2]

[1] *Institute of High Current Electronics, SB RAS, Tomsk, 634055 Russia*
[*] *E-mail: dv.beloplotov@hcei.ru*
[2] *Tomsk State University, Tomsk, 634050 Russia*

Received 21.10.2025; revised 7.11.2025; accepted 20.02.2026

The comparative effect of non-equilibrium atmospheric pressure plasma on the contact angle of metal surfaces (Cu, stainless steel, Al-Mg alloy) was determined. The plasma was generated using apokampic and nanosecond diffuse discharges in air as well as in an argon jet. Treatment for 15, 30, 60, 120 and 240 sec revealed that a 30–60 sec treatment is sufficient in all cases to achieve maximum hydrophilicity. The apokampic discharge in air and the pulsed discharge in an argon flow, which are simpler in technical implementation, are not inferior to the nanosecond atmospheric discharge in their ability to increase hydrophilicity. Partial preservation of the hydrophilic properties was noted for 24 hours after all three types of treatment.

Keywords: apokampic discharge, vacuum ultraviolet VUV, nanosecond diffuse discharge, non-equilibrium low-temperature plasma, plasma jet.

DOI: 10.51368/2949-561X-2026-1-31-38

Introduction

Atmospheric pressure plasma is a promising agent for controlling the surface properties of various materials (organic, inorganic, metals). In particular, it is known that plasma cleaning and activation of the surface increases the adhesive properties at the "metal–metal" and "metal–polymer" interfaces by approximately 3.4 times [1, 2]. The sources of such plasma are traditionally arc, corona, and barrier discharges, as well as various versions of the so-called atmospheric pressure plasma jets, in which the plasma flow is formed in the discharge gap (excitation is carried out by radio-frequency, corona, glow, or barrier discharge), after which it is ejected through a narrow capillary or slit due to the excess pressure in the discharge zone exceeding atmospheric pressure [3–5].

In the task of controlling the surface wetting angle, polymer and biological materials used in photonics and microelectronics are most often studied [6, 7]. Significantly fewer studies are devoted to controlling the wetting angle of metals, although the advantages of such treatment compared to, for example, plasma activation at reduced pressures are clear: devices for producing plasma jets are mobile and operate under normal conditions, allowing them to act on both smooth and profiled surfaces.

In particular, data have been obtained on the effect of atmospheric plasma on materials such as Al, Cu, Cr, steel (AISI 304L), and galvanized steel (H300LAD) [8–12]. In all these cases, plasma treatment reliably increased the hydrophilicity of the surfaces.

In the present study, to impart hydrophilic properties to the metal surface, we will use three

sources of atmospheric non-equilibrium plasma that have not been used for this purpose before. These are sources based on an apokamp discharge in air [13, 14], a nanosecond diffuse discharge in air [15], and a new source of vacuum ultraviolet (VUV) emission formed in an argon flow [16, 17]. All three sources produce active oxygen and nitrogen species at the boundary of the streamer channel (plasma jet) and the surrounding air or directly in the diffuse discharge. Furthermore, the first and second sources predominantly emit ultraviolet light originating from the second positive system of nitrogen (transitions $C^3\Pi_u$–$B^3\Pi_g$), while the third emits on the transitions $3s^2P$–$2p^2P^\circ$ and $3s^2P$–$2p^2D^\circ$ of atomic nitrogen at 174.3 and 149.3 nm, respectively.

The aim of the work is to assess the ability of these plasma sources to achieve maximum and long-term changes in the hydrophilicity of metallic surfaces (Cu, steel, Al-Mg alloy), considering that they have not been used for this purpose before.

Experimental setups and methods

Objects and methods of treatment. The objects of exposure were metal foils of copper, stainless steel and aluminum-magnesium alloy (97 % Al, 3 % Mg), with a thickness of 20, 100 and 50 μm, respectively. All these materials are widely used in manufacturing. Rectangular foil samples (15×15 mm) were placed in the path of propagation of an apokamp discharge streamer, an argon plasma jet, or in the area of action of a diffuse discharge at different distances x from the electrode system (Fig. 1).

The nanosecond discharge [15] was formed in a point-to-plane gap located inside a coaxial discharge chamber (Fig. 1*a*). Voltage pulses of negative polarity with an amplitude of –25 kV and a duration of 4 ns were applied to an electrode 6 mm in diameter made of stainless steel, the end of which had a conical shape with an angle of 60 degrees. The voltage pulse repetition rate was 100 Hz. The grounded counter electrode had the shape of a cylinder with a diameter of 20 mm. The distance between the electrodes was 6 mm. Samples of metal foils exposed to the plasma of the nanosecond discharge were placed on the end face of the grounded electrode. Air was pumped along the axis of the discharge gap using a diaphragm pump and a special nozzle placed on the high-voltage electrode. The pumping rate did not exceed 5 L/min.

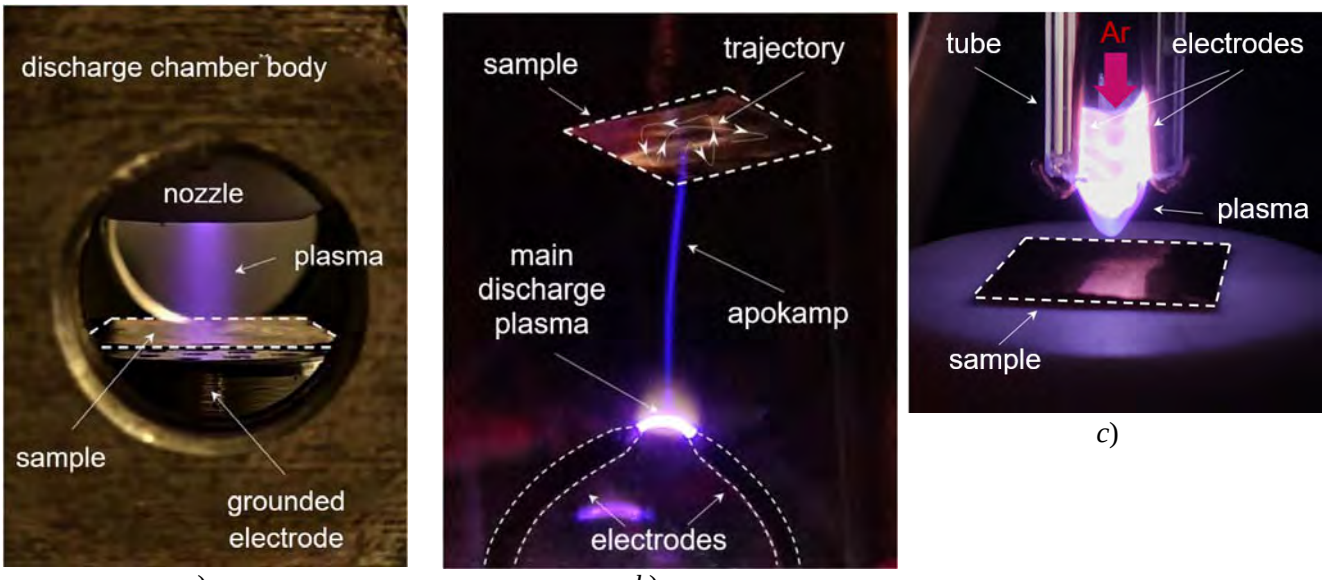

a) *b*) *c*)

Fig. 1. Photographs of the discharge systems during the treatment of copper samples (15×15 mm): (a) nanosecond discharge in air at atmospheric pressure with a pulse repetition rate of 100 Hz, exposure 1/90 sec, (b) apokamp in air at atmospheric pressure, exposure 1/30 sec, (c) pulsed discharge in an argon flow with VUV emission, exposure 1/30 sec.

The apokamp discharge was formed between pointed rods 2 mm in diameter made of stainless steel, which were oriented towards each other (Fig. 1*b*). The distance between them was 4 mm. Voltage pulses of positive polarity with an amplitude of 10 kV and a duration of 1 μs were applied to one of the electrodes, and the pulse repetition rate was 27 kHz. The opposite electrode was connected to one plate of a capacitor with a capacitance of 10 pF, the other plate of which was grounded. This electrical circuit is of fundamental importance for the formation of an apokamp discharge [18]. During the voltage rise stage (0.5 μs), a breakdown of the gap (over tens of ns) occurred between the rods, forming a discharge channel with a characteristic dark space near the cathode and an extended positive column. As the voltage increased, the capacitor charged almost to the open-circuit voltage of the generator (considering the voltage drop in the plasma channel, as across an active load). From the bend of the discharge channel, which had a positive potential, a positive streamer started in a direction perpendicular to the axis of the discharge gap. Thus, an apokamp with a length of 2–3 cm was formed, visually resembling a so-called plasma jet (Fig. 1*b*). Samples of metal foils were placed in the path of the apokamp propagation at a distance of 2 cm from the electrodes. Exposure to the apokamp plasma was carried out upon direct contact of its tip, chaotically moving over the surface of the samples.

The pulsed discharge in an argon flow was ignited between parallel wires inside a quartz tube 50 mm long and with an inner diameter of 6 mm (Fig. 1*c*). Argon (99.99 % purity) was pumped through the quartz tube at a rate of 2 L/min. One of the wires was grounded. The second wire was connected to the high-voltage output of a pulse generator (amplitude 10 kV, duration 1 μs, pulse repetition rate 27 kHz) through a capacitor with a capacitance of 10 pF. As a result, a discharge channel formed between the wires, sliding along the wires in the direction of the argon flow. At the final stage, the discharge channel "emerged" from the end of the tube to a distance of 5–7 mm and broke off, after which the process was repeated. It is recalled that it was previously shown that VUV emission (174.3 and 149.3 nm) is generated in the plasma of such a discharge at the transitions of atomic nitrogen ($3s^2P - 2p^2P^0$ and $3s^2P - 2p^2D^0$) [17], formed during the dissociation of molecular nitrogen contained in the argon cylinder as an impurity, as well as when the discharge channel is pushed out from the end of the quartz tube into the atmosphere. Samples of metal foils were placed at a distance of 8–10 mm from the end of the tube so that the plasma channel did not touch their surface (Fig. 1*c*). However, VUV emission could reach the surface of the samples due to the displacement of air by the argon flow, which is transparent to VUV emission .

The samples were treated with plasma for 15, 30, 60, 120, and 240 seconds. There were 15 samples of each metal in total. The wetting angle was measured immediately after treatment and after 24 hours.

The wetting angle (θ) of the metal sample surface was measured using the sessile drop technique [19] with distilled water as the test liquid.

The measurement bench was assembled to ensure high accuracy in recording the droplet profile. For this purpose, the sample under study was placed on a three-coordinate stage with micrometer screws for precise positioning. A syringe with distilled water was fixed directly above the sample.

The droplet application procedure consisted of forming a droplet of distilled water with a diameter of 1.25 mm ($V \approx 1$ μL) at the tip of the needle, after which the stage was smoothly moved upward until gentle contact was made and the droplet was transferred to the treated (central) part of the sample surface, minimizing dynamic effects. The droplet diameter was monitored using a pre-calibrated digital on-screen ruler.

Illumination was provided by diffuse emission from a semiconductor laser diode ($\lambda = 652$ nm) without a collimator, passed through ground glass, which ensured a uniform and contrasting background for clearly defining the droplet profile.

The profile of the droplet resting on the sample surface was photographed from the side using a full-frame digital camera EOS R (Canon Ltd, Japan) with a K2 DistaMax long-distance microscope fitted with a CentriTel focuser and a CF-3 objective lens (Infinity Photo-Optical Company, USA), which has high (up to 1.7 μm)

spatial resolution. This ensured the necessary detail of the "droplet-air-sample" interfaces. The image from the camera was transmitted to a computer in real-time via a Wi-Fi channel.

The wetting angle was determined based on the obtained images using ImageJ software [20] with the installed Contact Angle plugin [https://imagej.net/ij/plugins/contact-angle.html]. This plugin allowed for mathematical approximation of the droplet profile and calculation of the angle between the tangent to the droplet profile at the contact point and the baseline (sample surface). To increase statistical reliability and account for possible surface heterogeneity, the measurement θ was performed 2–4 times on different areas of each sample. The final result was presented as the average value over all measurements, and the random error was also calculated at a confidence probability of 0.95, which made it possible to assess the accuracy and reproducibility of the obtained data. Depending on the method and mode of sample treatment, the relative random error of the wetting angle measurements could range from 10 to 40 %.

Results and Their Discussion

Initially, the wetting angles of the original untreated samples of copper, stainless steel, and the aluminum-magnesium alloy were measured. Thus, the initial values θ_0 for copper, stainless steel, and the aluminum-magnesium alloy were, respectively, 97.0±3.6°, 75.5±3.3°, 72.9±3.4°. The obtained values allow characterizing the initial surface of each sample. Thus, the surface of the copper foil sample can be considered weakly hydrophobic, since the average wetting angle exceeds 90°. As a rule, clean metals are characterized by hydrophilicity. The hydrophobic nature of the copper sample is probably due to the presence of adsorbed organic contaminants, which reduce the surface energy. The surface of the stainless steel and Al-Mg alloy samples can be characterized as hydrophilic (wetting angle significantly below 90°). These properties are probably determined by the presence of oxide films, the "metal–oxygen" bonds in which are polar and can interact with dipoles – water molecules.

Figure 2 shows the dependences of the wetting angle values of the studied samples immediately after treatment by all methods.

Analysis of the obtained dependences of the wetting angle, measured immediately after treatment, reveals a key pattern common to all samples and treatment methods, namely, the effect of plasma from all three types of discharge (apokamp discharge in air, nanosecond discharge in air, and pulsed discharge in Ar with VUV) leads to a significant decrease in the wetting angle, which indicates an increase in the hydrophilicity of the sample surface.

Let us consider in detail the results for each method of treating the sample surface. When exposing the samples to apokamp plasma, the strongest effect of reducing the wetting angle is observed for the Al-Mg alloy. Thus, the initial value $\theta_0 \approx 73°$ decreased to approximately 20° after just 30 seconds of treatment. Even after 15 seconds of exposure, the wetting angle decreases to 28°. For copper and stainless steel, the reduction in the wetting angle is also significant. Copper demonstrates the largest difference between the initial angle (97°) and that after exposure (32°). The sharpest decrease in θ occurs at short treatment times (15–60 s). Further increase in treatment duration (up to 240 s) leads to a more moderate additional decrease or stabilization of the angle, considering the random measurement error, indicating the achievement of a certain limit of surface modification.

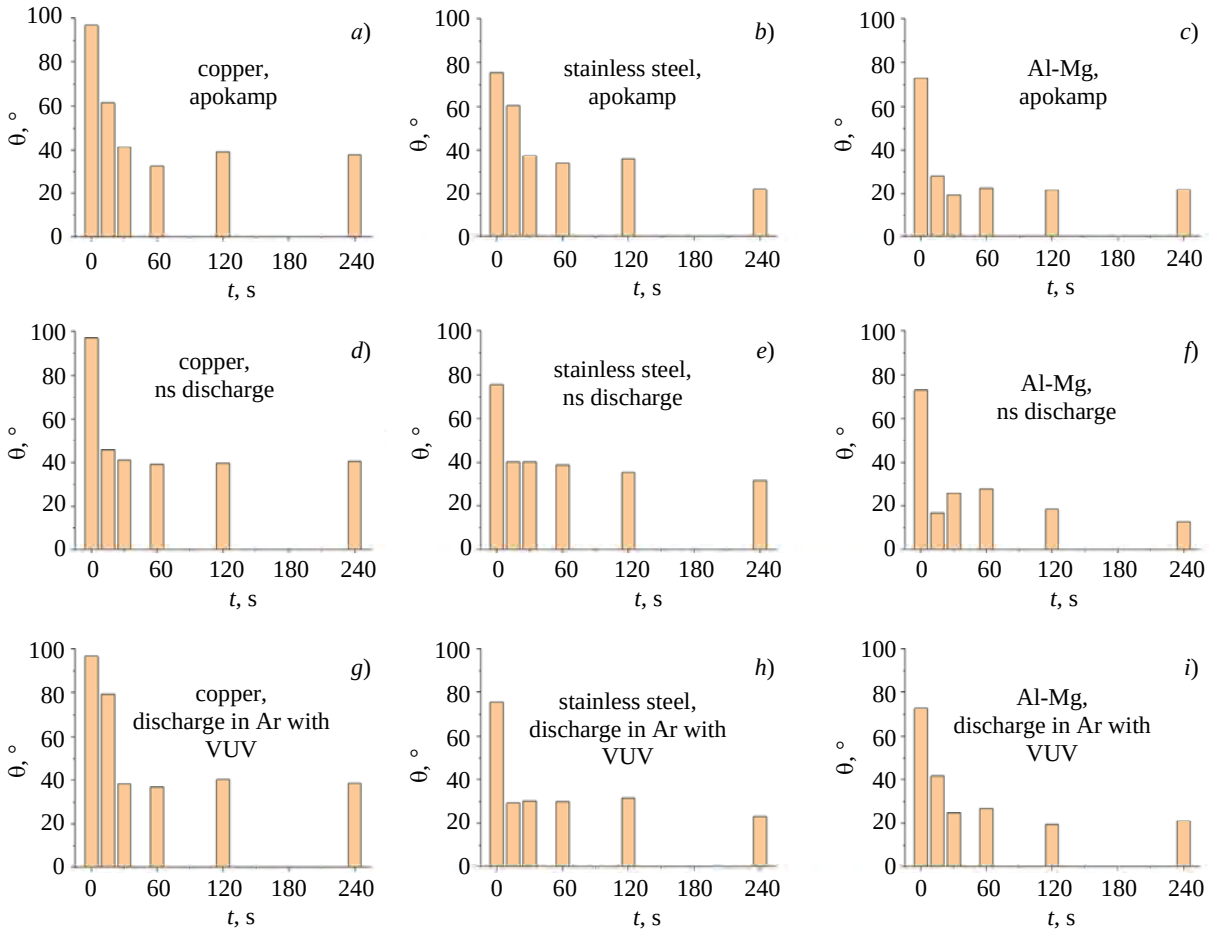

Fig. 2. Dependences of the wetting angle of the sample surface on the duration and method of treatment immediately after treatment: (a–c) apokamp in air at atmospheric pressure, (d–f) nanosecond discharge in air at atmospheric pressure, (g–i) pulsed discharge in an argon flow with VUV emission. Sample material: (a, d, g) copper, (b, e, h) stainless steel, (c, f, i) Al-Mg alloy

When treating samples with nanosecond discharge plasma, maximum (in the entire series of experiments) surface hydrophilization is also achieved. The Al-Mg alloy again shows the lowest values of θ down to 13°. Given the random error (tens of %), the absolute reduction of θ under the influence of the nanosecond discharge plasma is comparable to the results obtained under the influence of the apokamp plasma. For copper and stainless steel, the final values of θ are also comparable to those obtained under the influence of the apokamp plasma. Furthermore, as in the case of the apokamp, the main reduction in the contact angle is achieved within the first 30–60 s, after which stabilization or minor changes are observed.

When treating samples with the pulsed discharge plasma in an argon flow, which also combines the effect of VUV emission, all three metals also quickly achieve low values of θ (≈ 20–30°) with a treatment time of 30 s or more. Here, stainless steel demonstrates the fastest response to the treatment compared to other metals and discharges: with a treatment duration of 15 s, θ reaches ≈ 30°. This may indicate a particular sensitivity of the stainless steel oxide film to VUV emission or active species from the argon flow. For comparison, copper after 15 s of exposure shows a reduction in the contact angle only to ≈ 80°. However, at 30 s or more, a sharp decrease in θ to 36–40° occurs, followed by stabilization. The Al-Mg alloy shows better results. Effective reduction of θ to ≈ 20–25° is achieved after 30 s of exposure.

Figure 3 presents the contact angle values of the studied samples, obtained one day after treatment.

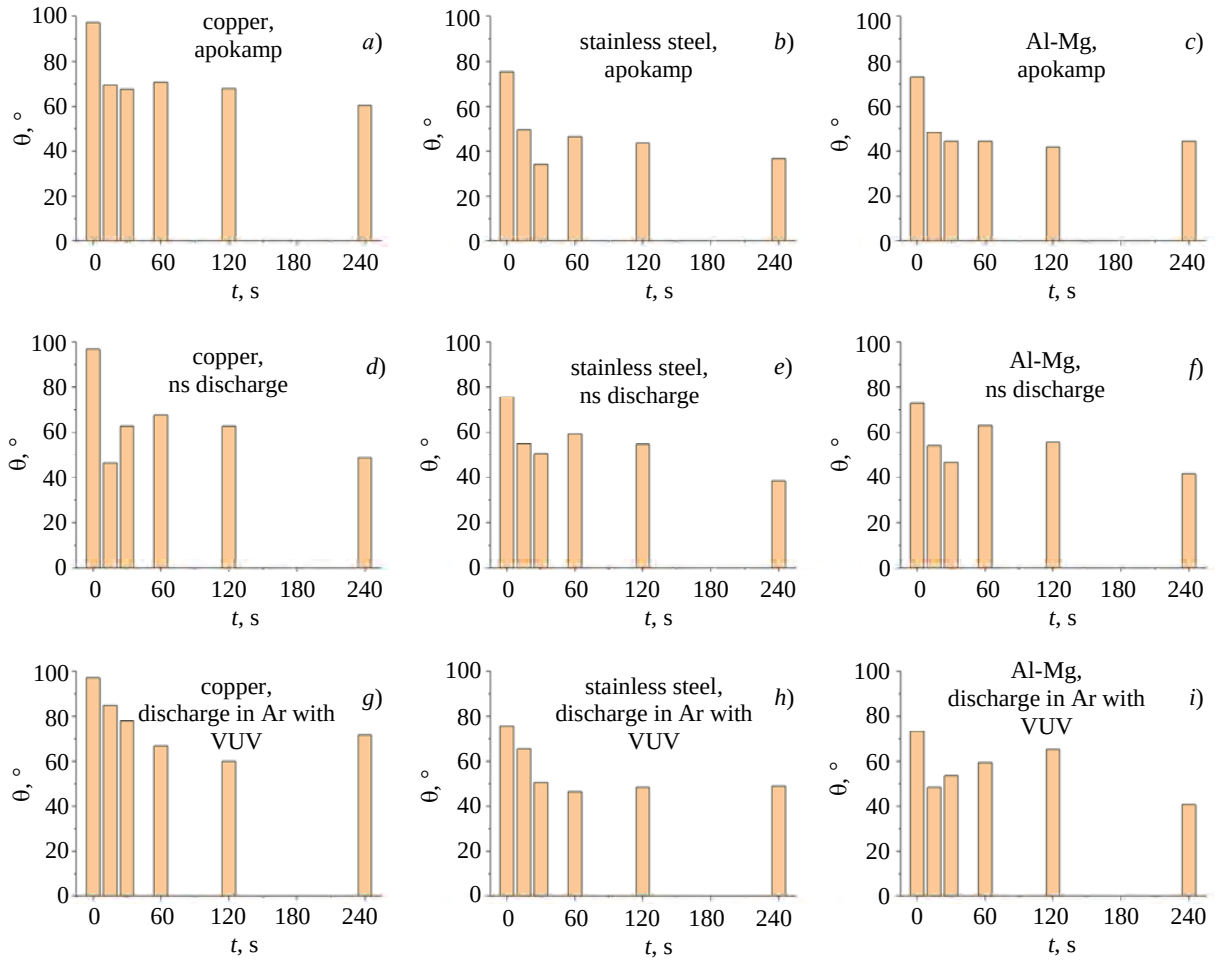

Fig. 3. Contact angles of the sample surface at various treatment durations and methods one day after treatment: (a–c) apokamp in air at atmospheric pressure, (d–f) nanosecond discharge in air at atmospheric pressure, (g–i) pulsed discharge in an argon flow with VUV emission. Sample material: (a, d, g) copper, (b, e, h) stainless steel, (c, f, i) Al-Mg alloy

Measurements taken one day after treatment show a partial recovery of the contact angle, specific to the materials used, which is common for all samples and all treatment methods.

Thus, for the case of apokamp plasma treatment, the fastest recovery of the contact angle is observed for copper samples. The values of θ recover to 60–70° for all treatment durations. For stainless steel and the Al-Mg alloy, the recovery is more moderate. The angles are in the range of 40–50°. It should be noted that there is no clear dependence of the final angle on the treatment duration. Such a dependence might possibly appear when measuring the contact angle minutes to hours after exposure.

In the case of treating samples with nanosecond discharge plasma, the degree of recovery of θ for copper and stainless steel is comparable to that of the apokamp, with final values of θ in the range of 50–70° for copper and 40–60° for stainless steel. The Al-Mg alloy shows a slightly less pronounced recovery, with values of θ remaining in the range of 40–55°.

The strongest recovery of θ values (up to 70–80°) is observed for copper one day after exposure to the products of the pulsed discharge in an argon flow, which also combines the VUV emission. This may indicate that the increase in surface hydrophilicity is achieved precisely through VUV modification, the effect of which is less stable. For stainless steel and the Al-Mg alloy, recovery of θ is also observed, but the final values of θ remain relatively low (≈ 50–60°).

The obtained data indicate that in our experiments, the change in the wettability of metal samples is the result of a complex impact (of plasma products and VUV emission). Their contribution depends on the type of discharge and the material. In the case of direct exposure of the

sample surface to apokamp and nanosecond discharge plasma in air, highly active plasma species (reactive nitrogen and oxygen species, radicals, and ions) probably effectively destroy and remove loosely bound contaminants from the sample surface. Subsequently, prolonged exposure to open air leads to the readsorption of contaminants/dust by the high-energy surface. Furthermore, upon direct contact of the air plasma with the surface, chemical modification may occur as a result of interaction with the same reactive nitrogen and oxygen species. New polar oxygen-containing functional groups (e.g., oxides) are formed on the metal surface, significantly increasing the surface energy and, consequently, the hydrophilicity.

In the case of exposing samples to the products of a pulsed discharge in an argon flow, which also includes the action of VUV emission, both photochemical reactions on the surface, causing the destruction of contaminants and the formation of radicals, and reactions with metastable particles of argon and nitrogen molecules can occur. These factors can modify the structure or chemical composition of the existing oxide and other films.

Conclusion

Three sources of non-equilibrium atmospheric pressure plasma with different spectral compositions and presumably different quantitative compositions of active components were used for the first time to increase the hydrophilicity of metal surfaces (Cu, stainless steel, Al-Mg alloy). It is shown that the contact angle drops to a minimum within 30–60 seconds, remaining unchanged at longer exposures considering the measurement error.

Measurements taken one day after treatment show a partial recovery of the contact angle, specific to the materials used, which is common for all samples and all treatment methods. The obtained data are preliminary for the subsequent identification of physical factors affecting the hydrophilicity of metal surfaces.

From the point of view of selecting the source (from those taken for the study) that provides the maximum and long-term change in hydrophilicity, the following can be concluded:

– compared to the nanosecond discharge, the apokampic discharge provides a comparable long-term change in the hydrophilicity of metal surfaces and is technically simpler to implement (no nanosecond pulse generation technique is needed, and no impedance matching of the generator output, transmission line, and load is required);

– the VUV emission source formed in an argon flow allows precise localization of the treatment area compared to the apokampic discharge.

Therefore, in the future, for treating other metal surfaces, particularly those used in medicine, a choice should be made in favor of sources that are relatively simple to operate — the apokampic discharge and the VUV emission source formed in an argon flow.

The study was supported by a grant from the Russian Science Foundation No. 25-79-31008, https://rscf.ru/project/25-79-31008/

REFERENCES

1. Massines F., Rabehi A., Decomps P., Gadri R. B., Segur P., and Mayoux C., J. Appl. Phys. **83**, 2950 (1998).
2. Klages C.-P., Hopfner K., Klake N., and Thyen R. Proc. Int. Symp. on High Pressure Low Themeral Chemistry, Hakone VII. 2000, p. 429.
3. Tendero C, Tixier Ch., Tristant P., Desmaison J., and Leprince P., Spectrochimica Acta Part B **61**, 2 (2006).
4. Schutze A., Jeong J. Y., Babayan S. E., Park J. Y., Selwyn G. S., and Hicks R. F., IEEE Trans. Plasma Sci. **26**, 1685 (1998).
5. Shao T., Zhang C., Wang R., Zhou Y., Xie Q., and Fang Z., IEEE Trans. Plasma Sci. **43**, 726 (2015).
6. Penkov O. V., Khadem M., Lim W.-S., and Kim D.-E., J. Coat. Technol. Res. **12**, 225 (2015).
7. Sidorova S. V., Moiseev K. M., Vasilev D. D., Nazarenko M. V., and Mikhailova I. V., Photonics **16**, 288 (2022).
8. Kim M. C., Yang S. H., Boo J. H., and Han J. G., Surf. Coat. Technol. **174–175**, 839 (2003).
9. Tang S., Kwon O. J., Lu N., and Choi H. S., Korean J. Chem. Eng. **21**, 1218 (2004).
10. Prysiazhnyi V., J. Surf. Eng. Mat. Adv. Technol. **3**, 138 (2013).

11. Liu X., Chen F., Huang Sh.-A., Yang X.-L., Lu Y., Zhou W. L., and Xu W.-J., IEEE Trans. Plasma Sci. **43**, 1959 (2015).
12. Kanbir Ö., Ayas K., and Çavdar K., Materials Testing. **67**, 875 (2025).
13. Sosnin E. A., Skakun V. S., Panarin V. A., Pechenitsin D. S., Tarasenko V. F., and Baksht E. Kh., JETF Letters. **103**, 761 (2016).
14. Andreev M. V., Kuznetsov V. S., Skakun V. S., Sosnin E. A., Panarin V. A., and Tarasenko V. F., Applied Physics, № 6, 32 (2016) [in Russian].
15. Sorokin D. A., Beloplotov D. V., Grishkov A. A., Shklyaev V. A., Tarasenko V. F., Belomyttsev S. Ya., and Lomaev M. I. High-voltage nanosecond discharge in an inhomogeneous electric field and its properties. Tomsk, STT, 2020 [in Russian].
16. Sosnin E. A., Panarin V. A., Panchenko A. N., Skakun V. S., and Sorokin D. A. Sposob polucheniya vakuumnogo ul`trafioletovogo izlucheniya. Patent RU 2844454 C1. Application № 2024119294. Priority: 10.07.2024. Published: 30.07.2025. Bull. 22.
17. Panchenko A. N., Beloplotov D. V., Panarin V. A., Skakun V. S., and Sorokin D. A., Optics and Spectroscopy **133**, 719 (2025) [in Russian].
18. Sosnin E. A., Babaeva N. Yu., Kozyrev A. V., Kozhevnikov V. Yu., Naidis G. V., Skakun V. S., Panarin V. A., and Tarasenko V. F., Phys. Usp. **64**, 191 (2021).
19. Summ B. D. and Goryunov Yu. V. Physico-chemical bases of wetting and spreading. Moscow, Khimiya, 1976 [in Russian].
Schneider C. A., Rasband W. S., and Eliceiri K. W., Nat. Methods. **9**, 671 (2012).

About authors

Beloplotov Dmitry Viktorovich, Candidate of Physical and Mathematical Sciences, Senior Researcher, Institute of High Current Electronics, SB RAS (2/3 Akademicheskii Ave., Tomsk, 634055, Russia). E-mail: dv.beloplotov@hcei.ru SPIN-code: 1677-3530, AuthorID: 688871

Skakun Viktor Semenovich, Candidate of Physical and Mathematical Sciences, Senior Researcher, Institute of High Current Electronics, SB RAS (2/3 Akademicheskii Ave., Tomsk, 634055, Russia). E-mail: vs.skakun@hcei.ru SPIN-code: 8772-3430, AuthorID: 40357

Sorokin Dmitry Alexeevich, Candidate of Physical and Mathematical Sciences, Head of the Laboratory, Institute of High Current Electronics, SB RAS (2/3 Akademicheskii Ave., Tomsk, 634055, Russia); Tomsk State University (36 Lenin Ave., Tomsk, 634050, Russia). E-mail: da.sorokin@hcei.ru SPIN code: 6447-6366, AuthorID: 614296

Sosnin Eduard Anatolyevich, Doctor of Physical and Mathematical Sciences, Leading Researcher, Institute of High Current Electronics, SB RAS (2/3 Akademicheskii Ave., Tomsk, 634055, Russia); Tomsk State University (36 Lenin Ave., Tomsk, 634050, Russia). E-mail: ea.sosnin@hcei.ru SPIN code: 1546-9106, AuthorID: 40356

Panarin Viktor Alexandrovich, Candidate of Physical and Mathematical Sciences, Researcher, Institute of High Current Electronics, SB RAS (2/3 Akademicheskii Ave., Tomsk, 634055, Russia). E-mail: va.panarin@hcei.ru SPIN code: 4482-5747, AuthorID: 505811

Zaitsev Bogdan Alexandrovich, Master's Student, Tomsk State University (36 Lenin Ave., Tomsk, 634050, Russia). E-mail: bogdanzaitsev683@gmail.com

PLASMA PHYSICS AND PLASMA METHODS

UDC 52.77 PACS: 52.80.Hc
EDN: JKVXCM

Nitrization of soil by corona discharge

© V. L. Bychkov*, I. G. Stepanov, P. A. Goryachkin, A. P. Shvarov, D. V. Bychkov, and A. A. Logunov

M. V. Lomonosov Moscow State University, Moscow, 119991 Russia
* *E-mail: bychvl@gmail.com*

Received 9.09.2025; revised 19.11.2025; accepted 20.02.2026

Experimental and theoretical studies of the nitrization possibility of turf-podzolic soil have been carried out. The experimental results obtained show that the electrical conductivity of the sample of the arable horizon of turf-podzolic soil increases with the time of exposure to plasma, the electrical conductivity of the soil paste after treatment for 2 hours is 285 μSm/cm, after treatment for 4 hours is 317 μSm/cm, with a reference value of the electrical conductivity of the sample of 115 μSm/cm. The nitrate content in the aqueous extract from the soil shows an increase in 2 hours to 14.5 mg/l, and a further decrease in 4 hours to 12.8 mg/l, relative to the control of 9 mg/l. Calculations show an increase in plasma concentrations of nitrogen components that enter the soil. Their accumulated concentrations reach 5×10^{21} cm^{-3}, which is an order of magnitude close to the experimental value of the accumulated nitrates during the experiment. The results confirm the idea of the possibility of using corona discharge for nitrization of poor soils.

Keywords: nitrization, turf-podzolic soil, electrical conductivity, nitrates, air, experiment, calculations.

DOI: 10.51368/2949-561X-2026-1-39-43

Introduction

The tasks of soil treatment by gas discharge appear relevant from the perspective of applications in agriculture. They are associated with the disinfection of air and grain, improvement of soil fertility, modification of its components, changes in their conductivity and chemical composition, and the generation of active particles within them [1–7]. Our study is devoted to these issues. Wherein, we investigate the question of saturating the soil with nitrogen components, i.e., whether the action of a corona discharge can lead to soil nitrification.

As it is known [2], nitrogen is the most important nutrient element for all plants: it is part of such important organic substances as proteins, nucleic acids, nucleoproteins, chlorophyll, alkaloids, phosphatides, etc. The nitrogen content in plants varies significantly depending on the plant species, their age, soil and climatic conditions of crop cultivation, etc. Nitrogenous compounds available to plants are formed mainly from soil organic matter as a result of its decomposition. Soil nitrogen reserves are replenished mainly through the nitrogen-fixing activity of free-living and nodule microorganisms and its input from atmospheric precipitation. To some extent, the nitrogen reserve in the soil is replenished by nitrogen from atmospheric precipitation.

According to literature data [2], precipitation brings from 2 to 11 kg of nitrogen per hectare annually. The known sources of replenishing natural nitrogen reserves are of practical interest, but they supply only a part of the nitrogen that is removed with agricultural crop yields. Therefore, measures should be taken to increase soil fertility and, first of all, to replenish its nitrogen reserves.

Experiments with the ^{15}N isotope [2] have shown that nitrogen losses due to volatilization average 15 % of that applied, sometimes reaching 30 %. The greatest amount of nitrogen lost due to volatilization is in the form of ammonia (NH_3), molecular nitrogen (N_2), and nitrous oxide (N_2O). A significant part of gaseous nitrogen is lost from the soil due to the denitrification process [2]. This process of reducing soil nitrate nitrogen to free gaseous nitrogen (N_2) occurs as a result of the vital activity of soil organisms. The denitrification process proceeds through a series of intermediate stages [2]

$$HNO_3 \rightarrow HNO_2 \rightarrow (HNO)_2 \rightarrow N_2O \rightarrow N_2 \quad (1)$$

Molecular nitrogen and nitrous oxide are the main gaseous products of biological denitrification, through the volatilization of which nitrogen losses from soils occur. The objective of this work was to elucidate the question of whether it is possible to carry out soil nitrification using a corona discharge plasma generated in the air near the soil surface. That is, whether it is possible to weaken the implementation of process (1).

Our research was conducted both experimentally using a negative corona discharge and theoretically based on a model of the discharge plasma. The following considerations guided these studies [1, 8]. The drift time of formed ions over a typical electrode needle length in the electric field of a corona discharge, on the order of 5×10^{-6}–5×10^{-7} s in air, is much less than the typical soil treatment time, which reaches 1–4 hours. The active particles formed in the air plasma also move rapidly toward the soil surface under the action of diffusion. Thus, the characteristic diffusion time of particles formed in the plasma to the soil surface is in the range of 0.3–1 s, which is also less than the soil treatment time by the corona discharge plasma, which reaches 1–4 hours. Therefore, it can be deemed that the formation of active particles in the air by the corona discharge, which under our conditions influence processes in the soil, is an important result of the plasma action.

The influence of the humidity factor on the results of the corona discharge action is of undoubted interest, so in our calculations we used a humid air model, which differs from the model in [9]. This paper presents the results of model studies to assess the influence of corona discharge plasma on the properties of the surface air layer near the soil surface at a real humidity level reaching 2 %, whose ionic components penetrate the soil.

Experiment

In the experiments, a corona discharge in air was used at voltages of 5–10 kV, with a current on the order of 100 μA, a description of which is presented in [7]. The discharge action time varied from 30 minutes to 4 hours. A negative corona was used as the test discharge in the experiment. The nitrate content was determined in a water extract at a soil-to-water ratio of 1:5. The products of chemical reactions in the soil pass into the solution. The nitrate content in the solution was measured by the potentiometric method using ion-selective electrodes on EXPERT-001 ionometer. The instrument is calibrated for a specific ion using standard solutions. KNO3 is used for nitrates.

A sample from the plow horizon of an agro-soddy-podzolic light loamy soil on mantle loams underlain by moraine was used. Coordinates of the soil sample section X: 56.03867°, Y: 37.16581°, Z: 215.0 BS (Baltic System). Location: Chashnikovo, Solnechnogorsky District, Moscow region

Basic properties of samples subjected to corona discharge:

1. Sample moisture content – in an air-dry state, in a state of hygroscopic moisture of 2.81 % (0.281 g H_2O/g soil).
2. Acidity pH = 5.53–5.56. Humus content 2.73 %.
3. Cation exchange capacity (CEC) – 14.25 mg-eq/100 g soil.
4. Physical clay content (particles < 0.01 mm) 26.8 %.
5. Specific surface area 51.0 m^2/g.
6. Surface charge density 2.4×10^{-3} mg/m².

Experimental Results

The experiment showed that the electrical conductivity of the sample from the plow horizon of sod-podzolic soil increases with the time of

plasma exposure. The electrical conductivity of the soil paste after treatment for 2 hours equals 285 μS/cm, after treatment for 4 hours – 317 μS/cm, with a control value of the sample's electrical conductivity being 115 μS/cm. The oxidation-reduction potential (ORP) of the control sod-podzolic soil water extract (without treatment) is 169–170 mV. The ORP of the water extract from the soil increases to +187 mV after 2 hours of treatment, and then after 4 hours of treatment it decreases to +180 mV. The ORP of distilled water is 147 mV+. Initial soil moisture content is 2.8 %, steam-saturated moisture is 6.0 %; after soil treatment for 2 h – moisture content is 5.4 %; after soil treatment for 4 h – moisture content is 2.9 %.

The nitrate content in the water extract from the soil shows an increase to 14.5 mg/l over 2 hours and a further decrease upon treatment for 4 hours to 12.8 mg/l, relative to the control of 9 mg/l. Thus, over 4 hours with an input power of 1 W, there was an increase in nitrate concentration by ~ 40 %, which is greater than the maximum nitrogen loss value of 30 % due to volatilization. At the same time, an improvement in soil quality occurred, as shown by the increase in ORP and electrical conductivity.

Model Calculations

This section presents the results of model studies to assess the influence of corona discharge plasma on the properties of the surface air layer near the soil surface. Model calculations were performed using the Kinet program, with verification in the Maple 2024 software, employing the Rosenbrock method. We were primarily interested in N_xO_y compounds and their yield from reactions, since upon interaction with water they form HNO_3 and, according to calculations in [10], are the main source NO_3^-. Based on the analysis of reaction rate constants [8–12], 150 chemical reactions and 34 components involved in the transformations were included in the model, such as: e, O, O_2, O_3, O^-, O_2^-, O_3^-, O_4^-, O^+, O_2^+, O_4^+, N, N_2, N_2^+, N_2O, NO, NO_2, NO_3, N_2O_5, NO^+, NO^-, NO_2^-, NO_3^-, NO_2^+, H_2O, H_2O^+, H_3O^+, H_2, H, H^-, OH, OH^-, HO_2, HNO_2, HNO_3. Calculations were performed for values of the reduced electric field: 150 Td and humidity of 2 % (in this case referring to the ratio of the concentration of water molecules in the air to the total concentration of components in the air). For humid air, the rate constant of dissociative attachment in the field at 150 Td was taken equal to 9.4×10^{-10} cm³/s, the rate constant of oxygen molecule dissociation in such a field was taken equal to 1.9×10^{-8} cm³/s, and the ionization rate constant was taken from [8].

In the case of an electric field strength of 150 Td, the concentration of O_3 increased to 3×10^{18} cm^{-3}, OH (is consumed rapidly, its concentration drops over 6 seconds from 8×10^{16} cm^{-3} to 2×10^{0} cm^{-3} (i.e., practically almost to zero), $N_2O \approx 2\times10^{14}$ cm^{-3}, $NO \approx 4.7\times10^{10}$ cm^{-3}, $NO_2 \approx 1.7\times10^{12}$ cm^{-3}, $NO_3 \approx 6\times10^{14}$ cm^{-3}, $N_2O_5 \approx 1.3\times10^{17}$ cm^{-3}, HNO_3 decreases to 4×10^{10} cm^{-3} considering the reverse reaction with HNO_2, whose increase reaches a value of 3.2×10^{17} cm^{-3}. This is seen from Fig. 1. This figure shows the evolution of the concentrations of the components HNO_3 and HNO_2. Evidently, within the framework of the presented model, the components HNO_2 remain in the system, which participate in enriching the soil with nitrogen components as a result of the sequence of chemical reactions.

With an increase in air humidity, the electron concentration increased by up to two orders of magnitude, which in the model leads to an acceleration in obtaining components; for example, for ozone at a humidity of 1 %, the ozone O_3 concentration rises to a value of 3×10^{18} cm^{-3} in 50 μs, and in the absence of moisture in the same time. The maximum achieved values of the components differed, especially for nitrogen components.

Fig. 2 presents the calculation results for the concentration of negative ions at E/N = 150 Td in air at 2% H_2O. It can be seen that at long times, the ion concentrations reach steady-state values, with the maximum increase observed for the NO^- ion.

Fig. 3 presents the concentrations of components involving nitrogen and ozone molecules depending on different concentrations of H_2O in the air at E/N = 150 Td. It can be seen that the concentration of N_2O_5 is the main one among the nitrogen-containing components at all humidity values considered.

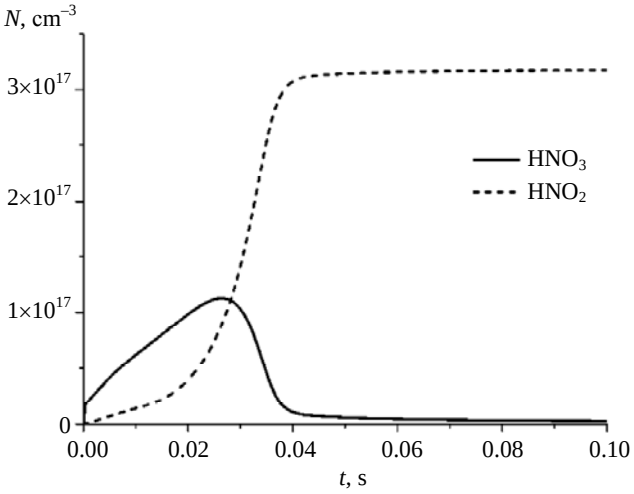

Fig. 1. Evolution of HNO_3 and HNO_2 (cm^{-3}) under discharge action at E/N = 150 Td in air at 2 % H_2O

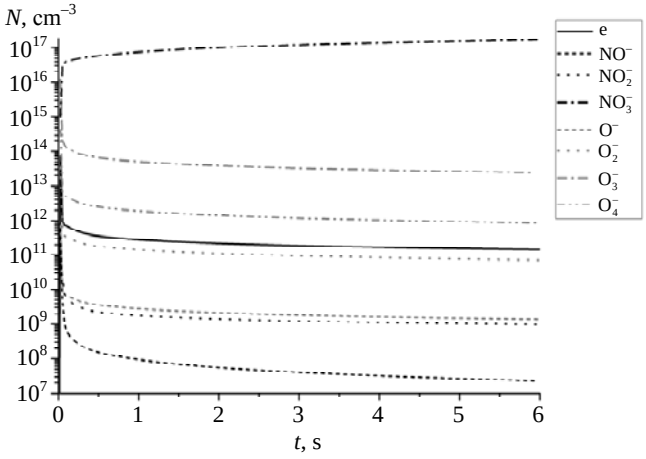

Fig. 2. Evolution of negative ion concentrations in air under discharge action at E/N = 150 Td in air at 2 % H_2O

Comparison with the models of Kossyi et al. [9] and Sekimoto et al. [10] confirms the correctness of the relative concentrations of the components and their dependence on the electric field; however, the absolute values of the concentrations of HNO_3 and N_2O_5 require further refinement within the framework of developing the theoretical model.

The model did not consider the results of work [12] on the role of positive nitrogen ions near the electrodes, nor the fact that particles composing the soil can enter the plasma. The obtained results allow a comparison of experimental and theoretical data.

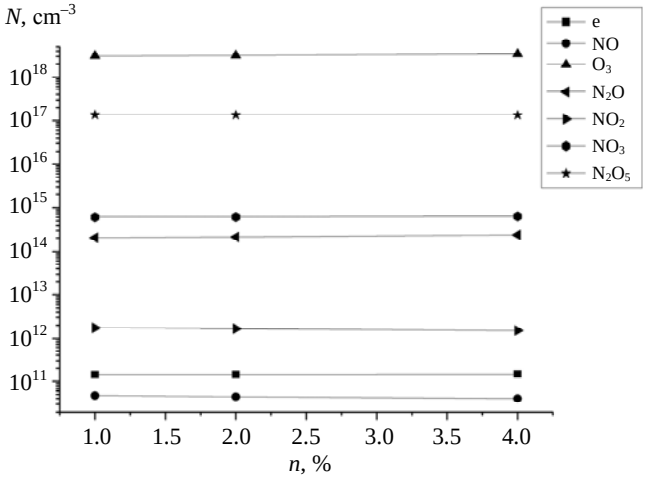

Fig. 3. Concentrations of neutrals for different concentrations of H_2O in air (n = 1%, 2 %, and 4 %). The calculation times for humid air were 600 μs, and for dry air – up to 100 s, E/N = 150 Td

Measurements showed that the average nitrate content in the water extract from the soil over 2 and 4 hours increases by 5 mg/l relative to the control, or 5×10^{-4} g/cm³. We will consider HNO_2 as the reference component. From Fig. 1, the production rate of HNO_2 can be estimated as $Q = 10^{19}$ $cm^{-3}\cdot s^{-1}$. This yields that over 4 hours, 2.4×10^{21} cm^{-3} of HNO_2 will be produced in the volume, and a similar order of magnitude concentration of N_2O_5 will be produced, i.e., both nitrate production mechanisms together will yield a quantity on the order of ~5×10^{21} cm^{-3}, which is of the same order of magnitude as the experimental value of nitrates produced. We see that efficient production of nitrates occurs.

Conclusion

The obtained experimental results show that the electrical conductivity of the sample from the plow horizon of sod-podzolic soil increases with the time of plasma exposure. The electrical conductivity of the soil paste after treatment for 2 hours equals 285 μS/cm, after treatment for 4 hours – 317 μS/cm, with a control value of the sample's electrical conductivity being 115 μS/cm. The oxidation-reduction potential of the water extract from the soil increases to +187 mV after 2 hours of treatment, and then after 4 hours of

treatment it decreases to +180 mV. This shows that an improvement in soil quality occurs. The nitrate content in the water extract from the soil shows an increase to 14.5 mg/l over 2 hours and a further decrease upon treatment for 4 hours to 12.8 mg/l, relative to the control of 9 mg/l. This latter result shows that the action of a low-power corona discharge leads to a positive effect on the properties of the surface soil layers. In this case, the nitrate content increases by an average of 50 %. The performed calculations show an increase in the concentration of nitrogen components in the plasma, which enter the soil. Their produced concentrations reach 5×10^{21} cm^{-3}, which is of the same order of magnitude as the experimental value of nitrates produced during the experiment. The obtained results confirm the idea of the possibility of using a corona discharge for the nitrification of poor soils. Therefore, the use of a corona discharge can be recommended as a means for soil activation in places of risky human activity.

REFERENCES

1. Encyclopedia of low-temperature plasma: Series B. Thematic Vol. **9-5**: Applied Plasma Chemistry / ed. Fortov V. E. Moscow, Janus-K, 2008 [in Russian].
2. Mineev V. G. Agrochemistry. Moscow, Nauka, 2006 [in Russian].
3. Alexandrov A. F., Bychkov V. L., Bychkov D. V., et al., Vestnik Moscow Univ. Ser. 3. Phys. Astron. № 4, 67 (2011) [in Russian].
4. Panov V. A., Pecherkin V. Y., Vasilyak L. M., et al., Plasma Phys. Rep. **47**, 623 (2021).
5. Bychkov V. L., Chernikov V. A., Deshko K. I., et al., IEEE Trans. Plasma Sci. **49** (3), 1028 (2021).
6. Bychkov V. L., Bikmukhametova A. R., Chernikov V. A., Deshko K. I., et al., IEEE Trans. Plasma Sci. **48** (2), 350 (2020).
7. Bychkov V. L., Shvarov A. P., Goryachkin P. A., et al., Applied Physics, № 6, 11 (2023) [in Russian].
8. Ardelyan N. V., Bychkov V. L., Bychkov D. V., and Kosmachevskii K. V. In Plasma assisted combustion, gasification and pollution control. Vol. **1** / Ed. Matveev I. B. Denver, Colorado, Outskirts press, 183 (2013).
9. Kossyi I. A., Kostinskiy A., and Matveev A. A., Plasma Sources Sci. Tech. **1**, 207 (1992).
10. Sekimoto K. and Takayama M., Eur. Phys. J. D. **50**, 297 (2008).
11. Atkinson R., Baulch D. L., Cox R. A., Crowley J. N., et al., Chem. Phys. **4**, 1461 (2004).
12. Chistolinov A. V., Yakushin R. V., Lubin A. A., and Ugryumov A. V., Applied Physics, № 6, 17 (2024) [in Russian].

About authors

Bychkov Vladimir Lvovich, Doctor of Physical and Mathematical Sciences, Leading Researcher, M. V. Lomonosov Moscow State University (Bd. 2, GSP-1, Leninskie Gory, Moscow, 119991, Russia). E-mail: bychvl@gmail.com SPIN-code: 2936-116; AuthorID: 18266, ORCID 0000-0002-5470-1297, Scopus Author ID 7102540048, WoS Researcher ID V-7141-2018

Stepanov Ilya Georgievich, Junior Researcher, M. V. Lomonosov Moscow State University (Bd. 2, GSP-1, Leninskie Gory, Moscow, 119991, Russia). E-mail: ilyastep91@mail.ru AuthorID: 1164557, Scopus ID 56900826700

Goryachkin Pavel Alexeevich, Postgraduate Student, M. V. Lomonosov Moscow State University (Bd. 2, GSP-1, Leninskie Gory, Moscow, 119991, Russia). E-mail: mystereo@mail.ru Scopus ID 57202727406

Shvarov Alexander Petrovich, Candidate of Biological Sciences, Associate Professor, M. V. Lomonosov Moscow State University (Bd. 2, GSP-1, Leninskie Gory, Moscow, 119991, Russia). E-mail: ashvarov@mail.ru SPIN-code: 5431-8919, AuthorID: 91766; Scopus ID 6505890527

Bychkov Dmitry Vladimirovich, Candidate of Physical and Mathematical Sciences, Junior Researcher, M. V. Lomonosov Moscow State University (Bd. 2, GSP-1, Leninskie Gory, Moscow, 119991, Russia). E-mail: bychkovdv@gmail.com AuthorID: 611220 Scopus ID 24502747200

Logunov Alexander Alexandrovich, Candidate of Physical and Mathematical Sciences, Junior Researcher, M. V. Lomonosov Moscow State University (Bd. 2, GSP-1, Leninskie Gory, Moscow, 119991, Russia). E-mail: logunov_aa@physics.msu.ru SPIN-code: 8069-9474, AuthorID: 244088, Scopus ID: 57214977963

PLASMA PHYSICS AND PLASMA METHODS

UDC 621.793.7
EDN: JMOVWT
PACS: 52.77.-n

Influence of plasma power and gas mixture composition on the formation of structures on silicon carbide

© V. S. Klimin[1,*] and I. E. Lysenko[2]

[1] *Institute of Radio Engineering Systems and Control, Southern Federal University, Taganrog, Rostov Region, 347922 Russia*
[*] *E-mail: kliminvs@sfedu.ru*
[2] *Mapper LLC, Moscow, 109316 Russia*

Received 31.07.2025; revised 27.08.2025; accepted 20.02.2026

This work investigates the processes of structure formation on silicon carbide (SiC) surfaces. The influence of plasma-chemical processing parameters on the geometric characteristics of fabricated structures was examined. Correlations were established between the power of the inductively coupled plasma (ICP) source, the composition of the gas mixture (O_2/SF_6/Ar), and key structural parameters: height, surface roughness, and wall inclination angle. It was demonstrated that increasing ICP power and SF_6 concentration in the gas mixture enhances the etching rate. Processing conditions correspond to extremes in surface roughness and specific wall inclination angles were identified. Notably, under conditions of 300 W ICP power and a gas ratio of O_2/SF_6/Ar = 81/7/11, the following results were achieved: structure height of 983.62 ± 37.64 nm, surface roughness of 14.13 ± 2.15 nm, and inclination angle of 74.63 ± 1.87°.

Keywords: silicon carbide, plasma-chemical etching, fluoride plasma, structure formation, microelectronics.

DOI: 10.51368/2949-561X-2026-1-44-48

Introduction

Silicon carbide retains the status of a key material not only for power electronics and Hf-devices but also for promising elements of gas sensors which is attributed to its unique combination of properties: wide band gap, high electric strength and exceptional chemical stability in the corrosive media [1–3]. The latter property is especially important for sensors where silicon carbide elements can function for a long time at increased temperatures ensuring the detection of flammable gases and toxins under the conditions inaccessible to traditional materials [4].

However, the use of silicone carbide in standard technology is limited by its high hardness and chemical inertness making it difficult to from micro- and nanostructures with the specified geometry and low surface defectiveness [4–6].

Plasma-chemical etching is one of the most promising methods of creating functional elements of devices on silicon carbide including parts of MOS transistors, MEMS and optical waveguides [4–7]. The parameters of the surface morphology of the etched surface directly affecting the sorption capacity and response speed are critical for gas sensors [7].

The key controlled parameters of the process determining the resulting characteristics of the structures are the power of plasma source and gas mixture composition [8–13]. The studies confirm complex interdependence of these parameters. Variation of gas mixture composition ($SF_6/O_2/N_2$, Cl_2/Ar) affects the chemical etching processes, the material removal rate and the formation of passivating layers which determines the anisotropy and morphology [8, 10, 14–16]. Oxygen additives affect the inclination angle of

the structure [13], and nitrogen – remodeling of the profile through the deposition of by-products [15]. For sensor applications it allows to create nanostructured surfaces with increased active area. The power of plasma source regulates the density of ions and radicals determining the balance of chemical etching and physical spraying. Its optimization is critical to achieve high speeds [12], minimize defects [5, 10, 17] and form structures with high aspectual ratio [18–21], which is important for the miniaturization of sensor elements. However, combination of high power and temperature can cause mask degradation [19, 22] and surface amorphization [5, 10, 20, 22], which degrades the electronic properties of sensitive layers.

Despite the progress [1–6], the quantitative investigation of the effect of combined variation of power and composition of gas mixtures on the parameters of the structures remains valid, especially in terms of application for technological processes of creating micro- and nanostructures in the new generation sensorics [7, 14, 9, 23–25].

The purpose of this work is to establish the experimental dependencies of parameters of the form structures on the modes of plasmachemical treatment at different powers of the inductive coupled plasma sources and gas mixture composition, including roughness and the inclination angle of the structure, which are critically important for the effectiveness of gas-sensitive elements.

Experiment procedure

Silicon carbon plates of hexagonal polytype 6H-SiC were used as samples in the experimental studies. A thin Al film with a thickness of 1 μm applied on the surface of silicon carbide by magnetron sputtering method. FP 9120-1 photoresist was used in work and it was dried at 110 °C for 15 min. Development is conducted in aqueous solution NaOH (0.6 %) until the aluminum surface not protected by photoresist was completely etched. Newly applied FP 9120-1 photoresist layer ensured protection of plate surface against contamination during separation of samples by laser cutting. Complete removal of the photoresist was conducted in the oxygen inductively-coupled plasma for 3 min. at plasma power source of 650 W. Mixture composition O_2 /Ar (87/13).

Plasmachemical treatment of silicone carbide samples was performed for three groups of samples. Gas mixture for creating plasma for the first group of samples had the following composition $O_2/SF_6/Ar$ (81/7/11); for the second group – $O_2/SF_6/Ar$ (74/14/11); for the third group – O_2 /SF_6/Ar (67/21/11). The power values of the inductive coupled plasma source for each group of samples varied from 300 W to 500 W. The power of the source of capacitively-coupled plasma equal to 150 W and shift voltage of 109 W. Operating pressure in the reactor was 2.5 Pa.

Upon completion of the plasmachemical treatment process the remnants of the protective Al mask were removed by etching in the NaOH (0.6 %) solution. Then the sample was scanned on the profilometer. The scanning was carried out in the area formed during the etching of the step to identify its parameters. A repeated scanning of the silicon carbide surface exposed to plasma during etching was also performed.

Experimental Results

Fig. 1 shows the image of the formed structure on the silicon carbide surface from the first experimental group (step in fig. 1*a*, the profile of the etched structure in fig. 1*b*).

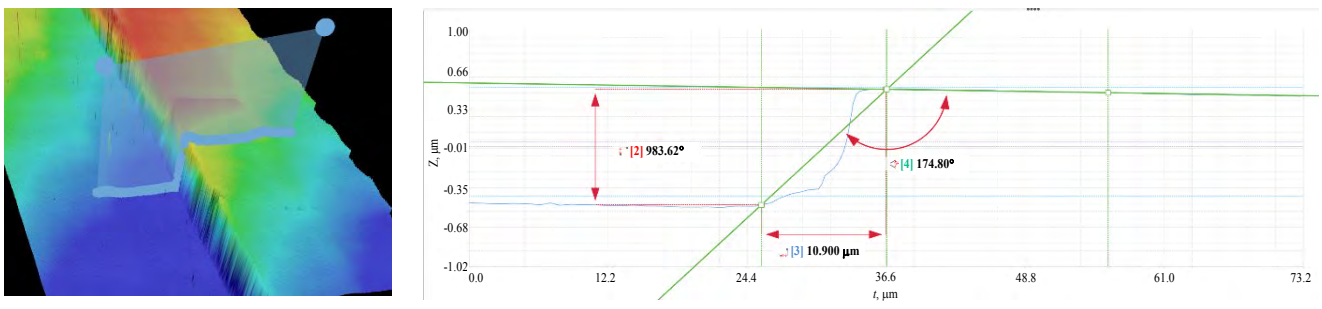

a) *b*)

Fig. 1. Image (a) and profile (b) of one of the obtained structures

Fig. 2 shows the results of experimental studies reflecting dependencies of the height of the obtained structures on the power of the inductive coupled plasma source at different ratios of gas mixture.

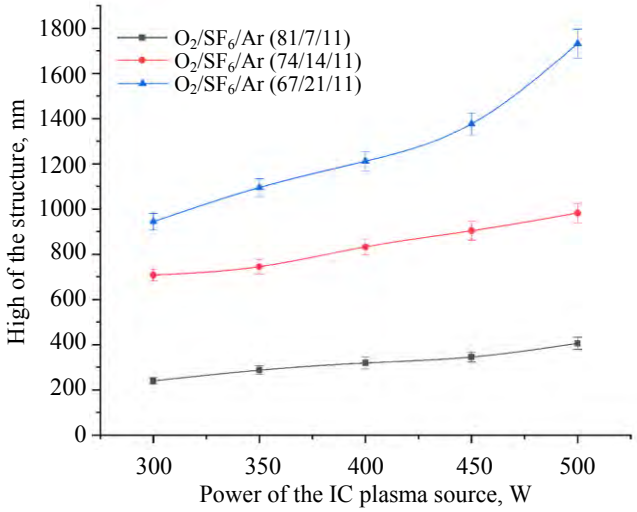

Fig. 2. Dependence of the height of the etched silicon carbide layer on the inductive coupled plasma source at different ratios of gas mixture

Analysis of the dependencies showed that under the given modes dependencies are actually linear. As the power of the plasma source increases, the structure height also increases which can be explained by the energy of particles and degree of decomposition of the reactive has mixtures that intensifies the process. It can also be seen that when increasing the proportion of the F-gas, the number of active fluorine ions in the plasma also increases and they in turn interact with the silicon component of the silicon carbide structure and provide heavy ions for the process of reactive ions etching which in turn results in the increase of height of the formed structures.

Fig. 3 shows the results pf experimental studies reflecting the effect of the power of the inductive coupled plasma source at different gas mixture rations on the inclination angle of the formed structure.

The obtained dependency shows that a decrease in oxygen in the mixture significantly affects the structure's angle which was measured as shown in fig. 1. It can be concluded from the dependency show that with a lower oxygen value and an increase in the power of the inductive coupled plasma source, the inclination angle value of the structure decreases. With an increase in the percentage of oxygen in the mixture, the inclination angle value changed slightly and has a virtually linear nature which correlates with theoretical studies.

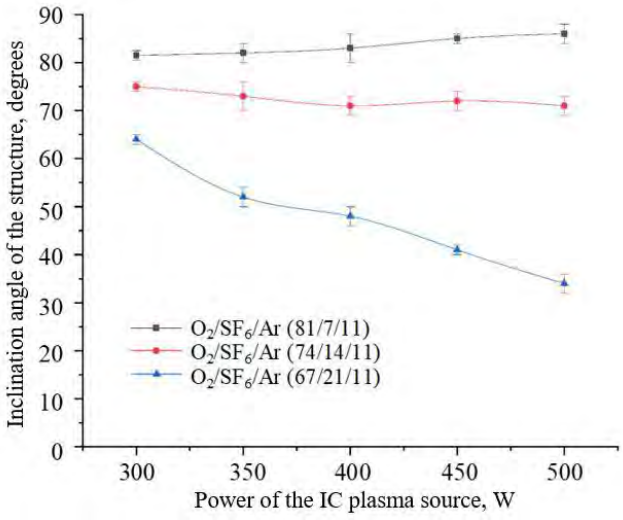

Fig. 3. Dependence of the angle of the structure formed on the surface of silicone carbide on the power of the inductive coupled plasma source at different gas mixture ratios

Fig. 4 shows the results of experimental studies reflecting the effect of the power of the inductive coupled plasma source at different gas mixture ratios on the roughness of the etched surface.

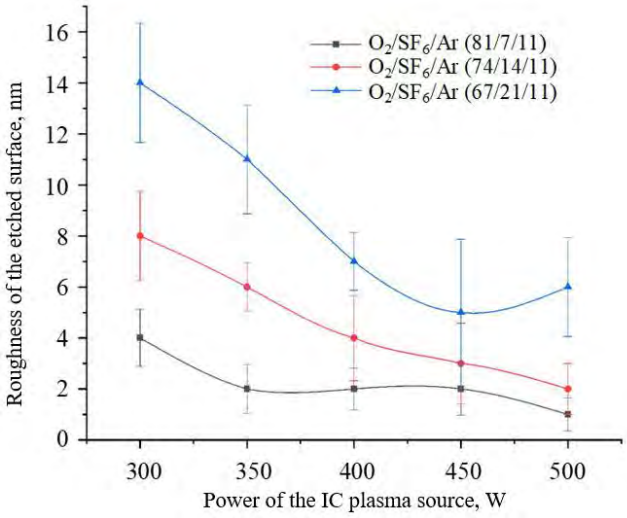

Fig. 4. Dependence of the roughness of the etched silicone carbide surface on the power of the inductive coupled plasma source at different ratios of gas mixture

The obtained dependency shows that when increasing the proportion of F-gas the number of heavy ions also increases and the roughness of the etched surfaces increases, when increasing the power, the process of chemical plasma polishing probably occurs and the component responsible for physical spraying decreases, respectively, the roughness of the etched surface decreases.

Conclusion

Thus the conducted experimental studies made it possible to establish patters of the height of the structures formed by plasma etching and the roughness of the etched surface on the power of the inductive coupled plasma source at different gas mixture ratios. Dependence of the inclination angle of the structure on the power of the inductive coupled plasma source at different gas mixture ratios was established. The modes corresponding to the minimum and maximum roughness of the etched surface at specified heights of the structure, as well as modes of formation of inclined structures. The identified experimental dependencies showed that the power increase of the inductive coupled plasma source, as well as increase of F-gas content result in the increase of plasmachemical etching rate, for example, at the ICP source power of 300 W and gas mixture composition of $O_2/SF_6/Ar$ (81/7/11), the height of the structure on the silicon carbide was 983.62 ± 37.64 nm and the roughness of the etched surface was 14.13 ± 2.15 nm, the inclination angle was 74.63 ± 1.87 degrees. It is shown that the increase in oxygen in the mixtures results in the increase of inclination angle of the structure, while the effect of power on the inclination angle of the stricture decreases with the oxygen increase.

The study has been conducted with the support of the Russian Science Foundation grant No. 25-29-00722, https://rscf.ru/project/25-29-00722/ in the Southern Federal University. The results of the study were obtained using the equipment of Mapper LLC.

REFERENCES

1. Huff J., Advanced Materials Technologies **8** (12), 2201235 (2023).
2. Ashurov K., et al., Semiconductor Science and Technology **38** (4), 043001 (2023).
3. Klimin V. S., Kessler I. O., Morozova Yu. V., Saenko A. V., Vakulov Z. E., and Ageev O. A., Applied Physics, № 6, 23–28 (2022) [in Russian].
4. Saenko A. V., Klimin V. S., Rozhko A. A., and Malyukov S. P., Journal of Communications Technology and Electronics **67**, 108–114 (2022).
5. Donaev R., et al., Materials **15** (1), 123 (2022).
6. Dzhuplin V. N., Klimin V. S., Morozova Y. V., Rezvan A. A., Vakulov Z. E., and Ageev O. A., Russian Microelectronics **50** (6), 412–419 (2021).
7. Tan X., et al., Microelectronics Engineering **301**, 111567 (2024).
8. Evans P., et al., Applied Physics Letters **102** (19), 192109 (2013).
9. Kato T., et al., IEEE Transactions on Semiconductor Manufacturing **34** (2), 198–205 (2021).
10. Li C., et al., Journal of Materials Chemistry C **12**, 18211–18237 (2024).
11. Klimin V. S., Kessler I. O., Morozova Yu. V., Saenko A. V., Vakulov Z. E., and Ageev O. A., Bulletin of the Russian Academy of Sciences: Physics **86**, S96–S99 (2022).
12. Ivanov A., et al., Scientific Reports **10**, 19977 (2020).
13. Pirnaci K., et al., Journal of Vacuum Science & Technology A **35** (3), 031301 (2017).
14. Liu G., et al., ECS Journal of Solid State Science **11** (4), 043008 (2022).
15. Klimin V. S., Morozova Y. V., Kots I. N., Vakulov Z. E., and Ageev O. A., Russian Microelectronics **51** (4), 236–242 (2022).
16. Arslan S., et al., Journal of Micromechanics and Microengineering **31** (8), 085002 (2021).
17. Pant B. and Tandon U., Plasma Chemistry and Plasma Processing **19**, 545–558 (1999).
18. Popova E., et al., Vacuum **193**, 110523 (2021).
19. Wang L., et al., Materials **15** (1), 123 (2022).
20. Zhang Y., et al., Journal of Applied Physics **130** (15), 153301 (2021).

21. Saenko A. V., Vakulov Z. E., Klimin V. S., Bilyk G. E., and Malyukov S. P., Russian Microelectronics **52** (4), 297–302 (2023).
22. Miyazaki H., et al., Nanotechnology **32** (25), 255301 (2021).
23. Holst F., et al., Applied Surface Science **579**, 152189 (2022).
24. Klimin V. S., Geldash A., and Ageev O. A., Russian Microelectronics **53** (2), 117–122 (2024).

About authors

Klimin Viktor Sergeevich, Candidate of Technical Sciences, Institute of Radio Engineering Systems and Control, Southern Federal University (44, Nekrasovsky lane, Taganrog, Rostov Region, 347922, Russia). E-mail: kliminvs@sfedu.ru SPIN-code: 1023-2994, AuthorID: 596163, Orcid ID 0000-0002-9794-4459, Scopus Author ID 57191376740

Lysenko Igor Evgenevich, Doctor of Technical Sciences, Head of the NTO project organization, Mapper LLC (Bd. 5, 42 Volgogradsky pr., Moscow, 109316, Russia). E-mail: igor.lysenko@mapperllc.ru SPIN-code: 7114-3671, AuthorID: 160157, Orcid ID 0000-0002-7505-1983, Scopus Author ID 55971078200

PLASMA PHYSICS AND PLASMA METHODS

UDC 533.9.07 PACS: 52.75.Hn
EDN: JSKZKF

Study of the dynamics of arc discharge burning in a methane-hydrogen-containing atmosphere in an alternating current plasma torch

© A. A. Safronov, Yu. D. Dudnik*, M. I. Vasilyev, V. N. Shiryaev, O. B. Vasilieva, A. V. Nikonov, and G. V. Nakonechnyi

Institute for Electrophysics and Electric Power of Russian Academy of Sciences, St. Petersburg, 191181 Russia
* *E-mail: julia_dudnik-s@mail.ru*

Received 3.09.2025; revised 26.09.2025; accepted 20.02.2026

The paper deals with the results of a study of a single-phase plasma torch with ring electrodes with a power of up to 10 kW. The measurements were carried out using copper ring electrodes at atmospheric pressure with an air flowrate of up to 3.5 g/s. A study of the plasma torch discharge development was carried out at two positions of the high-speed chamber: the first – the main optical axis of the chamber coincided with the main axis of the plasma torch, the second – the main optical axis of the chamber is located perpendicular to the plasma jet at the exit from the plasma torch. Time dependences of the plasma radiation intensity inside the chamber and a free plasma torch were obtained. A comparison was made of the arc power calculated from the oscillograms of current and voltage with the observed plasma radiation intensity at the frontal position of the video camera. It was determined that the plasma radiation intensity reflects the evolution of the arc power with a correlation coefficient of ~0.96.

Keywords: plasma torch, alternating current, arc discharge, high-speed video recording, correlation between plasma radiation intensity and arc power.

DOI: 10.51368/2949-561X-2026-1-49-54

Introduction

The widespread introduction of plasma torches into industrial technologies dictates the need for in-depth study of mechanisms of occurrence and maintenance of arc discharge stability. Standard diagnostic methods based exclusively on the assessment of electrical characteristics are often insufficiently informative for adequate reproduction of complex temporal and spatial dynamics of arc burning, especially under the conditions of rapidly changing processes.

Application of the newest digital cameras with high resolution and high frame rate provides comprehensive information about temporal and spatial features of the discharge, these methods allow you to record in detail instantaneous transformations of arc structure, trace trajectories of its movement.

The analytical approach proposed in this work is based on invertibility property of Fourier transformation making it possible to identify the relationship between main infrequences of spectral decomposition and characteristics of signal itself. By analyzing the intensity of plasma radiation, it becomes necessary to identify the relation between spacial-temporal changes of light brightness and internal mechanisms of electric arc formation. For this purpose, it is convenient to use the properties of Fourier transformation which is able to represent the signal (for example, change of radiation intensity) as a set of harmonic oscillations of different

frequencies. One of the key conclusions of the theory is that if the main component of the spectrum of two functions coincide, the functions themselves are quite close within the first approximation. In other words, the nature of the change in the main component of the plasma radiation spectrum is closely related to the development features of an electric discharge.

Practically this means that by measuring the distribution of frequencies in the plasma radiation intensity spectrum, you can indirectly judge the parameters of the electric arc itself, such as current strength, voltage and plasma temperature. Thus, establishment of such dependency makes it possible to create and effective diagnostic tool for the state of the plasma torch during operation.

The purpose of this paper is to study the processes of discharge development in plasma torch at two different positions of a high-speed camera and to conduct a comparative analysis of the arc power calculated according to the current oscillograms and voltage with the observed intensity of plasma radiation. Measurements were conducted using plasma-supporting gas – in the flow range from 0.84 g/s to 1.75 g/s at atmospheric pressure.

Experimental unit and measurement methods

Experimental setup included a single-phase AC current plasma torch with ring electrodes, electric power source, water cooling system, plasma-supporting gases supply system and measuring complex.

The operating plasma torch is shown in fig. 1. The key structural feature of the presented plasma torch is rejection of the traditional solid body that distinguishes this design from similar devices [1–3]. Single-phase plasma torch is a combination of joined ring-shaped electrodes made of copper grade M1 and M2. To provide visual observation of the arc development inside the plasma torch, electrode 1 is equipped with inspection window attached to it with mounting flange. Flange has a hole for a nozzle, its internal design creates a circuit for supplying plasma-supporting gas – circuit 1.

Electrodes 1 and 2 are connected via insulating flange with tangential ring for gas supply – circuit 2. Similarly, on the opposite side, electrode 3 is attached to electrode 2, creating one more circuit for gas supply – circuit 3. The size of interelectrode gaps between electrodes 1 and 2 and 2 and 3 can vary in the range from 0.1 to 3 mm. The external surface of electrode 2 is equipped with welded shell with connection pipes, making up cooling water jacket. The tightness of the structures is provided by rubber seals preventing the plasma-supporting gas and cooling liquid outside the plasma torch.

When a high voltage is applied to electrodes 1 and 3 of the plasma torch, an electrical breakdown of the interelectrode gaps occurs, which sequentially occurs between electrodes 1 and 2 and then electrodes 2 and 3. The result is the formation of two independent electric arcs.

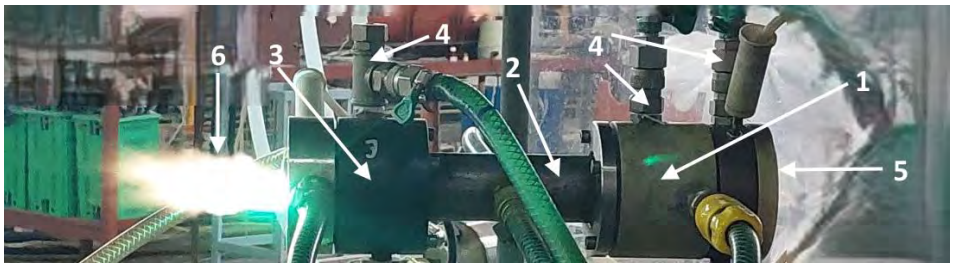

Fig. 1. Photo of working plasma torch with ring electrodes: 1 – electrode 1; 2 – electrode 2; 3 – electrode 3; 4 – gas supply circuits; 5 – inspection window; 6 – plasma jet

The movement of arc is attributed to the action of plasma-supporting gas introduced tangentially to the supply circuits, as well as the combined action of electrodynamic and gasdynamic forces. Under their influence the reference points of arcs begin to move along the surface of the ends of electrodes causing gradual deformation and elongation of arcs bringing them close together. Gradually the arcs close, merging into one electric arc extending from electrode 1 to

outlet nozzle of plasma torch where the arc joint point is localized at the outlet edge of the nozzle. The merged arc continues its propagation along the axial direction of the plasma torch channel, smoothly lengthening and escaping the nozzle, ensuring the operation of device.

Power supply control is based on the application of Advantech industrial microcontroller allowing to monitor the current and voltage oscillograms, instantaneous values of currents and voltages are recorded using current and voltage sensors included in the power supply system. Air gas supply system included a collector rack with installed pressure regulators with pressure gauges ensuring the possibility to adjust gas supply to each of the circuits.

The recording of current and voltage oscillograms of electric arc was conducted simultaneously with high-speed video filming of single-phase plasma torch with ring electrodes and installed gaps D_1 =1.9 mm and D_2 = 2,5 mm in air using Citius imaging High Speed Video Camera that was fixed in two positions relative to the plasma torch main axis. In the first case, the main optical axis of the camera coincided with the main plasma torch axis, namely, there was a frontal fixation of discharge inside the plasma torch discharge camera. In the second case the main optical axis of the camera was perpendicular to the main plasma torch axis and the camera recorded a plasma jet at the plasma torch outlet.

Time dependencies of the plasma radiation intensity inside the chamber and free plasma torch were obtained. The camera recorded high resolution video at 4.000 frames per second (fps) and was connected to the PC. Video files of plasma were recorded into computer memory for further processing. This registration method made it possible to determine the method of arc binding and conduct the detailed analysis of the temporal and spatial characteristics of the arc discharge.

Findings and Discussion

Electric arc in the air at atmospheric pressure is a stable electric discharge which is accompanied by a very bright glow. The arc occurs between electrodes at high current strength and relatively low voltage [4]. Temperature of the arc column can reach 4000–10000 K, which creates a spectral radiation continuum that is similar in the shape to the blackbody spectrum at similar temperatures due to strong bremsstrahlung and recombination radiation. It can be noted that at atmospheric pressure the radiation spectrum of electric arc is close to continuous overlaid with linear (band) spectra of atoms and molecules. Wavelength of the broad maximum and general spectrum shape are often well approximated by Planck's law.

It should be noted that the radiation intensity integral over all wavelengths makes a greater contribution compared to linear-band spectrum, the contribution of which is 10–30 % of the total radiated energy [5, 6]. In the same study it was noted that the UV radiation energy from electric arc at a voltage of 4 kV is 30 % of the energy radiated as optical emission. The prevailing share falls on the photon energy of visible light – up to 69 %. The infrared radiation energy is very small and is only 1 % of the total energy in the spectrum range.

Considering spectral sensitivity of Citius imaging video camera used in work which is limited from 300 to 1050 nm with a broad maximum at 450–750 nm, high-speed shooting gives information on the plasma radiation intensity and reflects fluctuations in the arc column, attenuation/restart, temperature fluctuations and the shape of the arc. These visual changes are related to changes in current and thermal capacity and that is why we can assume that in the first approximation they reflect the evolution of the plasma energy of the electric arc.

As the result of high-speed shooting of plasma torch, files recorded in the .avi format were captured. Each file was a sequence of separate frames formed by image sensor of Citius imaging camera. Thus, “avi” files reflect the dynamics of plasma radiation intensity of different plasma torch modes. Then the files were further processed: values of all pixels of each *j*-th frame are summed up, the total sum is recorded into *j*-th position. The result of summation was recorded into the *j*-th position of the new vector, the length of which corresponded to the number of frames in the “avi” file.

The study used a recording speed of 4000 frames/s with a resolution of 320×306.

As part of the research performed, a number of experiments with different air consumptions modes were conducted that are presented in the table. Air flow rate for each of the circuits varied from 0.9 g/s to 1.75 g/s and the plasma torch power varied up to 10 kV, the total duration of

experiment did not exceed 30 minutes and plasma torch showed stable operation during them. For all conducted experiments, the plasma torch power strength and arc voltage were synchronously measured with a time interval of 100 μs.

Measurement of oscillogram of current instantaneous values (marked with blue) and arc voltage (marked with red) for characteristic mode 13 are shown in fig. 2.

The calculated value of arc power as the product of the instantaneous values of current and voltage is shown in blue in Figure 3 and dependence of radiation intensity of the plasma when observed from the front video camera position – in red.

Table

Plasma torch operation mode

Record No.	Flow rate G_1, [g/s]	Flow rate G_2, [g/s]	Flow rate G_3, [g/s]	Total flow rate G, [g/s]
Video camera is perpendicular to the main plasma torch axis (profile)				
1-3	0.9	1	1.75	3.65
4-6	0.9	0.84	1.75	3.49
7-9	0.9	0.74	1.75	3.39
10	0.9	0.61	1.75	3.26
Video camera is coaxial to the plasma torch main axis (frontal view)				
11	0.9	0.92	1.72	3.54
12	0.9	0.84	1.72	3.46
13	0.9	0.74	1.72	3.36

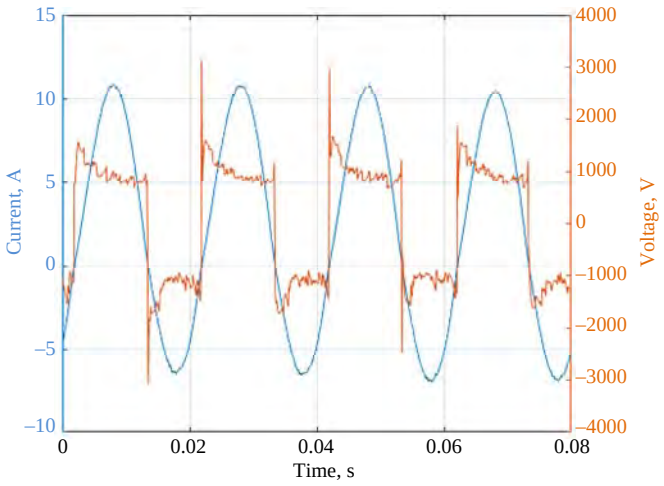

Fig. 2. Current and arc voltage oscillograms for mode 13

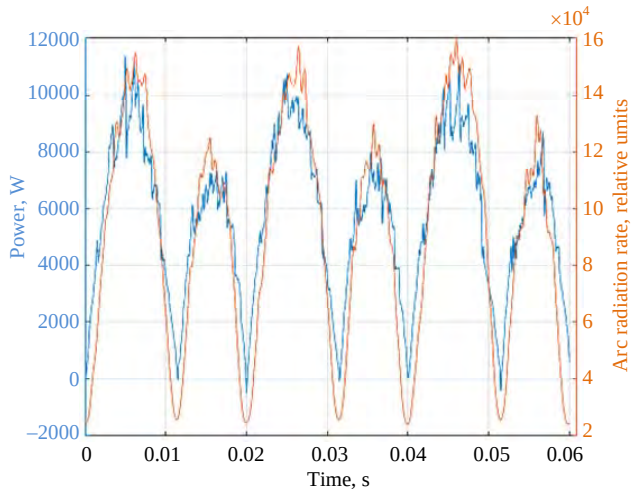

Fig. 3. The calculated value of arc power and the observed intensity of plasma radiation at frontal video camera position

Since the electrical parameters of the arc were calculated with a time interval of 100 microces and the video frames were recorded with a time step of 250 microsec, the samples were unified using interpolation for the calculation of correlation coefficient of two dependencies shown in fig. 3. Correlation coefficient between the calculated arc power value and observed plasma radiation intensity was $R = 0.9612$, which confirms the assumption that the arc radiation intensity measured by high-speed video camera reflects the evolution of electric arc plasm energy in a good approximation.

For the calculated discharge power function (fig. 3) and plasma radiation intensity, the frequency characteristics of processes was determined using Fast Fourier Transformation (FFT).

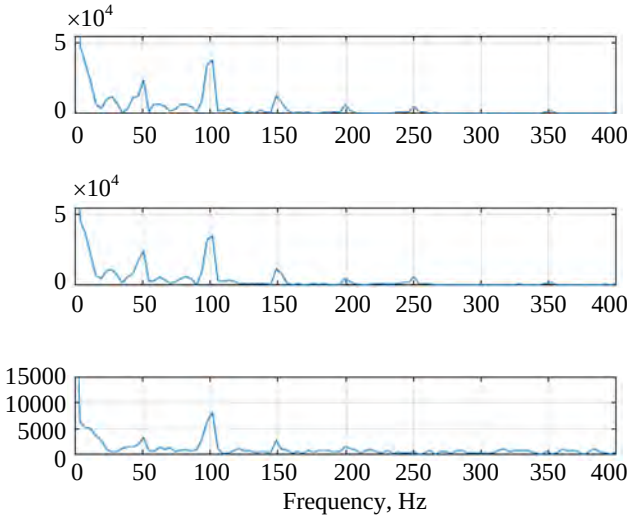

Fig. 4. Fourier Transformation: upper chart–fft of the calculated value of arc power; middle chart–fft of the plasma radiation intensity at frontal camera position (coaxial to the plasma torch main axis) and lower chart –fft of the plasma radiation intensity when the camera is perpendicular to the plasma jet at the plasma torch outlet

Fig. 4 shows the results of Fast Fourier Transformation for the calculated value of the arc power (upper chart) and plasma radiation intensity at two video camera positions – frontal (middle chart) and profile (lower chart). For all transformations the main frequency was 100 Hz and a very close ratio in amplitude of satellite frequencies that were multiples of the main frequency.

Using invertibility property of Fourier transformation, it follows that the coincidence of the fundamental frequencies of the Fourier transformation of functions results in closeness in the first approximation of the functions themselves. Thus and with similar consideration it can be assumed the plasma radiation intensity correlates well with the electric arc discharge power.

Conclusion

The study investigated the processes of discharge development in plasma torch at two different positions of a high-speed camera and compared arc power calculated according to the current oscillograms and voltage with the observed intensity of plasma radiation. During the analysis of measurements results we considered the dynamic characteristics related to changes in the process of arc burning in time, the value of arc power was calculated as product of instantaneous current and voltage values.

Comparison of the calculated value of the electric arc power and observed plasma radiation intensity confirms the assumption that the plasma radiation intensity measured using high-speed video camera shows the evolution of the electric arc plasma energy in good approximation, at the same time the correlation coefficient is ~ 0.9612.

Additional confirmation of the possibility of using plasma radiation intensity for the analysis of plasma torch electric arc power is based on the invertibility property of Fourier transformation from which it follows that the coincidence of the fundamental frequencies of Fourier transformation results in closeness in the first approximation of the functions themselves.

REFERENCES

1. Safronov A. A., Kovshechnikov V. B., Vasilieva O. B., Dudnik Y. D., Kuznetsov V. E., and Shiryaev V. N., High Temperature **57**(6), 808–812 (2019).
2. Safronov A. A., Kuzhnetsov V. E., Vasilieva O. B., Dudnik Yu. D., and Shiryaev V. N., Instruments and Experimental Techniques **62** (2), 193–200 (2019).

3. Safronov A. A., Kuzhnetsov V. E., Dudnik Yu. D., Shiryaev V. N., and Vasilieva O. B. Zavalishenskie chteniya 23. Collection of reports of the XVIII Int. Conf. on Electromechanics and Robotics. Sankt-Petersburg, 2023, pp. 391–395 [in Russian].
4. Lee T. H., Kam D. H., Oh J. H., and Kim Ch., JMR&T **19**, 685–696 (2022).
5. Nagi Ł., Kozioł M., and Zygarlicki J., Energies **13** (19), 5137 (2020).
6. Nagi Ł., Kozioł M., and Zygarlicki J., Energies **13** (7), 1676 (2020).

About authors

Safronov Alexey Anatolyevich, Doctor of Technical Sciences, Corresponding Member of RAS, Head of the Department, Institute for Electrophysics and Electric Power of Russian Academy of Sciences (18 Dvortsovaya Emb., St. Petersburg, 191181, Russia). E-mail: 9932553@mail.ru SPIN code: 5771-1927, AuthorID: 37228, Scopus ID 7101711564

Dudnik Yulia Dmitrievna, Research Assistant, Institute for Electrophysics and Electric Power of Russian Academy of Sciences (18 Dvortsovaya Emb., St. Petersburg, 191181, Russia). E-mail: julia_dudnik-s@mail.ru SPIN-code: 7170-7912, AuthorID: 670805, ORCID ID 0000-0002-0640-9419, Scopus ID 5719415463

Vasilyev Mikhail Ivanovich, Candidate of Physical and Mathematical Sciences, Researcher Assistant, Institute for Electrophysics and Electric Power of Russian Academy of Sciences (18 Dvortsovaya Emb., St. Petersburg, 191181, Russia). E-mail: milavas@mail.ru SPIN-code: 6836-0810, AuthorID: 162131

Shiryaev Vasily Nikolaevich, Senior Research Assistant, Institute for Electrophysics and Electric Power of Russian Academy of Sciences (18 Dvortsovaya Emb., St. Petersburg, 191181, Russia). E-mail: shiryaev_vasily@mail.ru SPIN-code: 6728-5133, AuthorID: 37225, Scopus ID 7004970484

Vasilieva Olga Borisovna, Research Assistant, Institute for Electrophysics and Electric Power of Russian Academy of Sciences (18 Dvortsovaya Emb., St. Petersburg, 191181, Russia). E-mail: vasilieva_olg@mail.ru SPIN-code: 7691-1515, AuthorID: 161866, ORCID ID 0000-0003-1095-7677, Scopus ID 56803683100

Nikonov Aleksei Valerevich, Research Assistant, Institute for Electrophysics and Electric Power of Russian Academy of Sciences (18 Dvortsovaya Emb., St. Petersburg, 191181, Russia). E-mail: nikonav@mail.ru SPIN-code: 8215-1982, AuthorID: 161871, ORCID ID 0000-0003-1471-2327, Scopus ID: 57193909837

Nakonechnyi Gennadii Valerevich, Research Assistant, Institute for Electrophysics and Electric Power of Russian Academy of Sciences (18 Dvortsovaya Emb., St. Petersburg, 191181, Russia). E-mail: ghennady@mail.ru SPIN-code: 6708-9658, AuthorID: 161870, Scopus ID: 57198769946

PHYSICAL SCIENCE OF MATERIALS

UDC 621.383.4/5
EDN: KZMAQY

PACS: 42.79.Pw, 85.60.Gz,
07.57.Kp, 85.60.Dw

Comparative analysis of the refractive and spectral properties of the potassium bromide with boron-nitride nanotubes interface

© P. V. Kuzhakov[1,2] and N. V. Kamanina[1,2,3,*]

[1] *AO "Scientific and Production Corporation S. I. Vavilov State Optical Institute", St. Petersburg, 192171 Russia*
[*] *E-mail: nvkamanina@mail.ru*
[2] *B. P. Konstantinov Peterburg Institute of Nuclear Physics – National Research Center "Kurchatov Institute", Gatchina, 188300 Russia*
[3] *St. Petersburg State Electrotechnical University "LETI", St. Petersburg, 197022 Russia*

Received 16.04.2024; revised 31.05.2024; accepted 20.02.2026

The analysis of the refractive and spectral properties of the potassium bromide with the boron-nitride nanotubes interface is carried out. The most optimal type of the chirality of the boron–nitride nanotubes in the entire spectral range studied was revealed, which is established from the calculations performed for the dispersion dependences of the refractive index of the boron–nitride nanotubes with different chirality, as well as from the evaluation of the dispersion dependences of the reflection coefficient at the KBr-BNNT interface with different chirality.

Keywords: spectral range, refractive index, interface, reflection spectra.

DOI: 10.51368/2949-561X-2026-1-55-59

Introduction

In recent years boron nitride nanotubes (BNNT) have attracted the attention of researches due to their significant semiconductor gap [1] and high structural stability which makes this material suitable for use in photoluminescent devices [2]. The electronic and structural properties of BNNT have been theoretically studied in detail. Dependence of the width of the BNNT forbidden region was studied as the function of internal diameter and nanotube chirality. A strong decrease in the gap was observed for nanotube diameters less than about 1.3 nm. The calculations of minimal lattice energy conducted by Hernandez et al. show that the most favorable chirality for BNNT is zigzag [4]. They also predicted the Young's modulus of about 300 GPa for zigzag-shaped and armchair nanotubes and a certain degree of bending perpendicular to the nanotube axis. There are a lot of experimental works performed using transmission electron microscopy (TEM) [5–14], and much fewer articles on the electronic and optical properties of BNNT samples. This is, for example, the IR response of BN vibrations in BNNT which can be used to characterize nanotube samples. BNNT were first obtained by methods of arc discharge and laser ablation. Most produced BNNT have a zigzag-shaped geometry.

Nowadays there is great interest in boron nitride nanotubes due to their electronic [15–17], thermal [18–21] and mechanical properties [22, 23] which in many cases differ or are superior to similar parameters of carbon nanotubes. The analysis of IR spectroscopy with Fourier Transformation is conducted using infrared spectrum analyzer in the wave numbers range of 4000–500 cm^{-1}, relative to the KBr crystal matrix. As shown in fig. 1*a*,*b*, with similar absorption curves in BNNT we can observe characteristic peaks at 1380 cm^{-1} and 800 cm^{-1}

due to fluctuations in the B-N bond, parallel and perpendicular axis, respectively [24]. Both peaks demonstrated a strong IR-response which is observed in IR reflecting power.

Spectrum presented in fig. 1*c* shows strong fluctuations at 1375 and 793 cm^{-1}, which are characteristic for primary and secondary absorption curves of BNNT, respectively. Absorption band at 1375 cm^{-1} is related to the well-known planar vibrational mode (E2g) BNNT, while weak absorption bands at 793 cm^{-1} correspond to the out of plane vibration [25]. Both the spectrum profile and absorption curves are similar to those reported for BNNT which additionally conforms that unprocessed products are BNNT.

Absorption spectra of BNNT (fig. 1*d*), show sharp absorption peak at 204 nm. Light absorption property and width of the BNNT forbidden zone were investigated using spectroscopy operating in the reflection mode, as shown in fig. 1*e*. Reflection spectra in the UV-visible range show two absorption bands at 266.4 nm (4,65 eV) and 214.2 nm (5,79 eV) corresponding to the exciton absorption and optical absorption at the BNNT band edge [25].

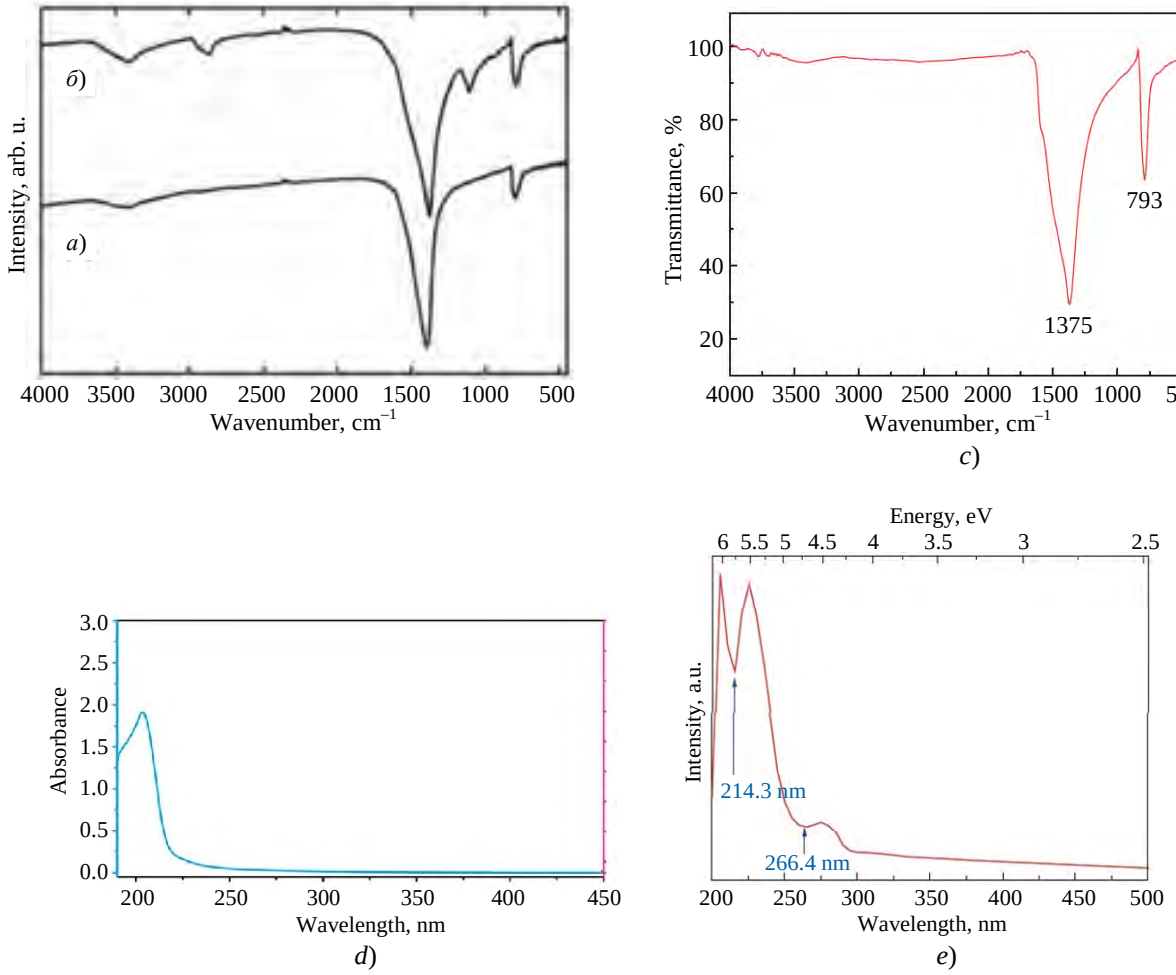

Fig. 1. Infrared Fourier transmission spectrum of the original (a) and restored (b) boron-nitride samples in the Kbr [26] matrix, (c) transmission spectrum BNNT (d) absorption spectra in the BBNT UV-visible range (e) reflection spectra in the BBNT UV-visible range [25]

Refraction index models

Dispersion characteristic of the KBr refraction index is well-known and approximates as follows [27]:

$$n^2 = 1.39408 + \frac{0.79221\lambda^2}{\lambda^2 - (0.146)^2} + \frac{0.01981\lambda^2}{\lambda^2 - (0.173)^2} + \frac{0.15587\lambda^2}{\lambda^2 - (0.187)^2} + \frac{0.17673\lambda^2}{\lambda^2 - (60.61)^2} + \frac{2.06217}{\lambda^2 - (87.72)^2} \quad (1)$$

Here λ is wavelength expressed in μm.

By using the calculation method presented in studies [27–29], the following calculations were performed in this study.

It is shown (fig. 2) that the refractive index of nanotubes based on boron nitride depends on the chirality (armchair, zigzag-shaped, chiral).

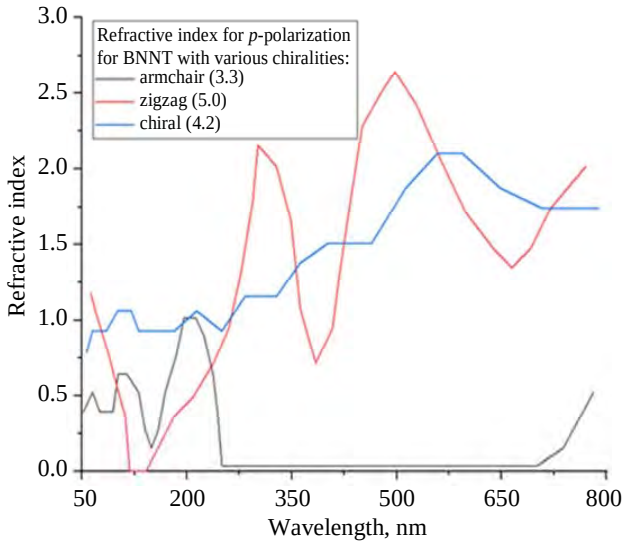

Fig. 2. Dispersion dependencies of the BBNT refractive index with different chirality for p-polarized (a) and s-polarized (b) radiation in the spectrum range of 50–800 nm

The obtained refractive properties of BBNT with different chirality types do not contradicts the data of publications [30–34] where optical properties of such structures have also been studied.

Reflection spectrum models

Continuing to study the spectral parameters of BNNT, we have also calculated reflection losses at the interfacial area of KBr-BNNT (fig. 3) using the Fresnel's formula (2) for normal incidence:

$$R(\lambda)=\left(\frac{n_{\mathrm{KBr}}(\lambda)-n_{\mathrm{BNNT}}(\lambda)}{n_{\mathrm{KBr}}(\lambda)+n_{\mathrm{BNNT}}(\lambda)}\right)^2 \qquad (2)$$

Here n_{KBr} and n_{BNNT} are refraction indices for KBr (see expression 1) and BNNT (from the data from fig. 2) that depend on the wavelength λ.

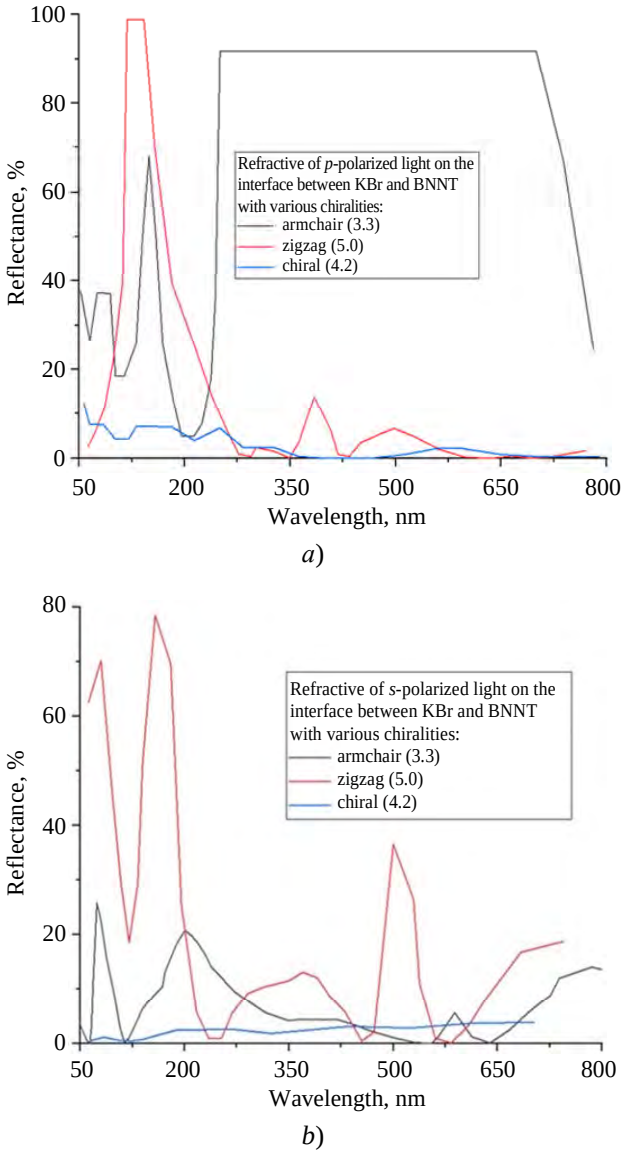

Fig. 3. Dispersion dependencies of the reflection coefficient at the interfacial area of KBr-BNNT with different chirality for p-polarized (a) and s-polarized (b) radiation in the spectrum range of 50–800 nm

It should be noted that when selecting the chirality of nanotubes, BNNTs with chirality (4.2) were selected, similarly to [35]. Based on the analysis of publications [36–40] of different BNNT types, this type of nanotubes has a more optimal atomic configuration.

Conclusion

From the calculations performed for the dispersion dependencies of the BBNT refractive indices with different chirality, as well as from the assessment of dispersion dependencies of the reflective coefficient at the KBr-BNNT interfacial area with different chirality, it was established that the most stable properties in the entire studied spectral range (from X-ray to the neat infrared) are boron–nitride nanotubes with chirality (4.2).

It was shown that for further calculation of energies of chemical bonds and optimization of structures it is more preferable to use boron–nitride nanotubes with chirality (4.2) the reflection spectra of which differ by no more than 10 % from the calculated and predictable ones in both polarizations and spectral range from 50 to 800 nm.

The studied nanostructured material can be used as new structural material for spectroscopy, for example, when optimizing the polarization of potassium bromide plane-parallel plates in X-ray apparatus. Low reflection may be a priority here for the selected spectral range. The conducted study will be useful in the training process when studying the properties of nanostructural composites functioning not only in the visibly spectrum but also in the area of IR-spectrum.

REFERENCES

1. Blaze X., Rubio A., Louis S. G., and Cohen M. L., Europhys. Lett. **28**, 335 (1994).
2. Bai X. D., Wang E. G., and Yu J., Appl. Phys. Lett. **77**, 67 (2000).
3. Rubio A., Corkill J. L., and Cohen M. L., Phys. Rev. B **49**, 5081 (1994).
4. Erdinands E., Goze K., Bernier P., and Rubio A., Phys. Lett. **80**, 4502 (1998).
5. Chopra N. G., Luyken R. J., Cherry K., Crespi V. X., Cohen M., Louis C. G., and Zetl A., Science **269**, 966 (1995).
6. Loiseau A., Willaime F., Demoncy N., Hug G., and Pascard H., Phys. Rev. Lett. **76**, 4737 (1996).
7. Terrones M., Hsu W., Terrones H., Zhang J., Ramos S., Hare J., Castollo R., Prassides K., Cheetham A., Kroto H., and Walton D., Chem. Phys. Lett. **259**, 568 (1996).
8. Chen Y., Fitz Gerald J., Williams J., and Bulcock S., Chem. Phys. Lett. **299**, 260 (1999).
9. Lee R., Gaville J., Lamy M. Chapelle D., and Loiseau A., Phys. Ed. B **64**, 121405 (2001).
10. Ma R., Bando Y., and Sato T., Letters on Chemistry and Physics **337**, 61 (2001).
11. Golberg D., Bando Y., Kurashima K., and Sato T., Chem. Phys. Lett. **323**, 185 (2000).
12. Golberg D., Bando Y., Bourgeois L., Kurashima K., and Sato T., Carbon **38**, 2017 (2000).
13. Han W., Bando Y., Kurashima K., and Sato T., Chem. Phys. Lett. **299**, 368 (1999).
14. Han W., Bando Y., Kurashima K., and Sato T., Appl. Phys. Lett. **73**, 3085 (1998).
15. Rubio A., Corkill J., and Cohen M., Phys. Rev. B: Condens. Matter. **49**, 5081 (1994).
16. Radosavljevi M., Appenzeller J., Derycke V., Martel R., Avouris Ph., Loiseau A., Cochon J.-L., and Pigache D., Appl. Phys. Lett. **82**, 4131 (2003).
17. Cumings J. and Zettl A., Solid State Commun. **129**, 661 (2004).
18. Han W., Mickelson W., Cumings J., and Zettl A., Appl. Phys. Lett. **81**, 1110 (2002).
19. Tang C. and Bando Y., Appl. Phys. Lett. **83**, 659 (2003).
20. Xiao Y., Yan X., Xiang J., Mao Y., Zhang Y., Cao J., and Ding J., Appl. Phys. Lett. **84**, 4626 (2004).
21. Chopra N. and Zettl A., Solid State Commun. **105**, 297 (1998).
22. Bettinger H., Dumitrica T., Scuseria G., and Yakobson B., Phys. Rev. B: Condens. Matter. **65**, 41406 (2002).
23. Dresselhaus M. S., Dresselhaus G., and Eklund P. C., Science of Fullerenes and Carbon Nanotubes. Academic Press. New York, 1996.
24. Jacoby M., Chem., Eng. News. **82** (35), 34 (2004).
25. Zhong B., Huang X., Wen G., Yu H., Zhang X., Zhang T., and Bai H. Large, Nanoscale Res Lett. **26.6** (1), 36 (2010).
26. Xie S. et al., Chem. Commun. 3670–3672 (2005).
27. Li H. H., Journal of Physical and Chemical Reference Data **5** (329), 436–448 (1976).
28. Jain S. K. and Srivastava P., Journal of Applied Physics **114** (073514), 1–9 (2013).
29. Sotudeh M., Boochani A., Parhizgar S. S., and Masharian S. R., International Nano Letters **10**, 293–301 (2020).

30. Badehian H. A. and Vatankhah C., Journal of Molecular Structure **1262** (133069), 1–9 (2022).
31. Jain S. K. and Srivastava P., Comp. Mater. Sci. **50**, 3038–3042 (2011).
32. Allard C., Nascimento R., Fossard F., Schué L., Flahaut E., Loiseau A. et al., ChemRxiv, 171 (2019).
33. Kuzmany H., Shi L., Martinati M., Cambr´e S., Wenseleers W., K¨urti J., Koltai J., Kukucska G., Cao K., Kaiser U., Saito T., and Pichler T., Carbon **171**, 221 (2021).
34. Borin B. G., Fairbrother A., Rotach L., Bayle M., Paillet M., Liang L., Meunier V., Hauert R., Dumslaff T., Narita A., M¨ullen K., Sahabudeen H., Berger R., Feng X., Fasel R., and Ruffieaux F., ACS Appl. Nano Mater. **2**, 2184 (2019).
35. Mutlu Z., Llinas J. P., Jacobse P. H., Piskun I., Blackwell R., Crommie M. F., Fischer F. R., and Bokor J., ACS Nano **15**, 2635 (2021).
36. Kayang K. W., Nyankson E., Efavi J. K., Abavare E. K. K., Garu G., Onwona-Agyeman B., and Yaya A., Results in Materials **2**, 100029 (2019).
37. Allard C., Schu´e L., Fossard F., Recher G., Nascimento R., Flahaut E., Loiseau A., Desjardins P., Martel R., and Gaufr`es E., Adv. Mater. **322**, 202001429 (2020).
38. Cadena A., Botka B., Pekker A., Tschannen C. D., Lombardo C., Novotny L., Khlobystov A. N., and Kamar´as K., Molecular encapsulation from the liquid phase and 6-armchair graphene nanoribbon growth in carbon nanotubes. **2207**, 09533 (June 2022).
39. Ciampalini G., Blaga C. V., Tappy N., Pezzini S., Watanabe K., Taniguchi T., Bianco F., Roddaro S., Fontcuberta A., Morral I., and Fabbri F., 2D Mater. **9**, 035018 (2022).
40. Jordan J. W., Townsend W. J. V., Johnson L. R., Walsh D. A., Newton G. N., and Khlobystov A. N., Chem. Soc. Rev. **50**, 10895.1 (2021).

About authors

Kuzhakov Pavel Viktorovich, Candidate of Physical and Mathematical Sciences, Research Assistant, AO "Scientific and Production Corporation S. I. Vavilov State Optical Institute" (36/1 Babushkina st., St. Petersburg, 192171, Russia); B. P. Konstantinov Peterburg Institute of Nuclear Physics – National Research Center “Kurchatov Institute” (1 mkr. Orlova roshcha, Gatchina, 188300, Russia). E-mail: kpv_2002@mail.ru SPIN-code: 7178-5273, AuthorID: 977752

Kamanina Nataliya Vladimirovna, Doctor of Physical and Mathematical Sciences, Leading Research Assistant, Head of the Department, AO "Scientific and Production Corporation S. I. Vavilov State Optical Institute" (36/1 Babushkina st., St. Petersburg, 192171, Russia); B. P. Konstantinov Peterburg Institute of Nuclear Physics – National Research Center “Kurchatov Institute” (1 mkr. Orlova roshcha, Gatchina, 188300, Russia); St. Petersburg State Electrotechnical University "LETI" (Litera F, 5 ul. Professora Popova, St. Petersburg, 197022, Russia). E-mail: nvkamanina@mail.ru SPIN-code: 1231-5045, AuthorID: 40388

PHYSICAL SCIENCE OF MATERIALS

UDC 53.096+ 541.64+544.77+537.226. PACS: 182.45.Hk
EDN: NMKJTR

Effect of stoichiometry and synthesis conditions on the phase composition, structure, and electrophysical properties of thin films of $Ag_xCu_{1-x}GaSe_2$ – chalcopyrites, promising electrodes for photoelectrochemical decomposition of water

© V. V. Rakitin[1,*], I. D. Kulemetyev[1,2], U. R. Baklanova[1,2], D. S. Lutsenko[1], A. V. Stanchik[3], E. V. Rabenok[1], and M. V. Gapanovich[1,2,4]

[1] *Federal Research Center on Problems of Chemical Physics and Medicinal Chemistry, Russian Academy of Sciences, Moscow, Region, Chernogolovka, 142432 Russia*
[*] *E-mail: domi-tyan@yandex.ru*
[2] *Faculty of Fundamental Physical and Chemical Engineering, Moscow State University, Moscow, 119991 Russia*
[3] *Scientific-Practical Materials Research Centre, National Academy of Sciences of Belarus, Minsk 220072 Republic of Belarus*
[4] *Moscow Institute of Physics and Technology, Moscow Region, Dolgoprudny, 141701 Russia*

Received 29.10.2025; revised 12.11.2025; accepted 20.02.2026

The effect of stoichiometry and synthesis conditions on the phase composition, structure, and electrophysical properties of $Ag_xCu_{1-x}GaSe_2$ chalcopyrite thin films on Mo/MoO_x substrates, promising electrodes for photoelectrochemical decomposition of water, is studied. It has been found that annealing in selenium vapor at T = 650 °C for a period of 15 minutes to 30 minutes is most optimal for obtaining single-phase films. For the first time, for samples of the $Ag_{0.9}Cu_{0.1}GaSe_2$ composition synthesized at 550 °C for 15 minutes, a record photocurrent density of 1.763 mA/cm^2 (at E = –0.517 V relative to 3M SSCE) was obtained under lighting conditions close to AM1.5.

Keywords: thin films, electrodes, chalcopyrites $CuGaSe_2$ and $AgGaSe_2$, phase composition, electrophysical properties.

DOI: 10.51368/2949-561X-2026-1-60-67

Introduction

Currently, one of the most relevant areas of photovoltaics development is the production of hydrogen through photoelectrochemical water splitting. A large number of different compounds are used for this purpose, such as $NaTiO_3$:La, TiO_2, WO_3@$BiVO_4$, compounds of the A^{III}-B^{IV} group, chalcopyrites A^I-B^{III}-C^{VI}_2, and others. All of them can act as photocathodes or photoanodes and have both certain advantages and characteristic disadvantages.

For instance, photocathodes based on $NaTaO_3$:La exhibit one of the highest water splitting rates (9.7 mmol/h) and a high quantum yield (about 57 % under 270–300 nm illumination). However, this requires the use of UV radiation, and the surface of the photocathode must be non-uniform to allow adsorption of the evolved hydrogen [1]. The use of a wide-bandgap *n*-type semiconductor TiO_2 with $E_g = 3$ eV also requires illumination in the UV region. Furthermore, this system necessitates the presence of Pt or any p-type semiconductor as a counter electrode for the target hydrogen evolution reaction [1, 2]. Compared to TiO_2, the compound $BiVO_4$ has a smaller bandgap ($E_g = 2.4$ eV) and extends into the visible part of

the solar spectrum [3]. Study [4] shows that photoanodes based on $BiVO_4$ thin films have an efficiency of $\eta = 5.2$ % (AM1.5 illumination), and with the use of WO_3@$BiVO_4$ core-shell nanostructures, the efficiency of such devices can reach up to 8.2 % [5, 6]. However, achieving such values and high photocurrent densities (6.56 mA/cm^2) requires a tandem structure in the form of WO_3@$BiVO_4$ (photoelectrochemical cell) – GaAs/InGaAsP (heterojunction), which significantly complicates the design and increases production cost. Photocathodes based on thin films of A^{III}-B^{IV} compounds have efficiencies up to 14 %, but they remain quite complex to manufacture and expensive. Furthermore, the long-term operational stability of such photocathodes in aqueous solutions is low [7]. Another type of semiconductor that could potentially be used for hydrogen production is $Cd_{1-x}Zn_xS$ powders ($0.2 \le x \le 0.35$), which possess different bandgaps $E_g = 2.49$–2.68 eV depending on the zinc content in the films. Such systems can operate in the visible range of sunlight and generate hydrogen at a rate of 0.35 mmol/h·g_{cat}. However, efficient photolysis of water requires the use of a consumable SO_3^{2-}/S^2 component, which acts as an electron donor and facilitates the reduction of hydrogen ions from the solution [8]. Currently, a more promising approach is the creation of a heterojunction with *p*-type semiconductors to increase photocurrent density and facilitate electron transfer to active sites on the surface.

To achieve this goal, an alternative to expensive photocathodes based on III-V group semiconductors can be used: compounds of the A^I-B^{III}-C^{VI}_2 type with a chalcopyrite crystal structure, specifically $CuGaSe_2$ (CGS) and $AgGaSe_2$ (AGS), as well as solid solutions based on them. The main advantages of these compounds are their variable bandgap ($E_g \sim 1.6$–1.8 eV), close to the optimal value for efficient absorption of solar radiation and overcoming the thermodynamic threshold of water splitting (1.23 V), as well as their low cost compared to A^{III}-B^{IV} group compounds [9, 10, 11]. Considering the high overpotentials for hydrogen and oxygen evolution reactions caused by the low surface activity of the semiconductor as a photoelectrode and a number of other losses, $E_g \sim 1.7$ eV is considered the optimal value for water molecule splitting [12]. The most widespread method for producing high-efficiency photocathodes based on $CuGaSe_2$ is thermal evaporation of elements in vacuum. CGS films obtained by this method demonstrate high crystallinity and large grains (1–2 μm), and the efficiency of photoelectrochemical water splitting reaches $\eta \sim 10$ % [13]. It is known that an important feature of this method is composition control, as the Cu/Ga ratio significantly affects the properties of the photocathodes. In study [14], devices based on films with different Cu/Ga ratios exhibited high photocurrent density values: –19.0 mA/cm² for Cu/Ga = 0.85 and –12.1 mA/cm² for Cu/Ga = 0.33 (at a potential of $E = -0.4$ V vs. reversible hydrogen electrode, RHE) and 0 mA/cm² for Cu/Ga = 0.85 and –8.2 mA/cm² for Cu/Ga = 0.33 (at a potential of $E = 0$ V vs. RHE) in 0.5 M H_2SO_4 (pH = 0.4). For a pure $CuGaSe_2$ single crystal in study [15], values of $j_{ph} = 0.3$ mA/cm² were achieved (at a potential of $E = 0$ V vs. RHE, which corresponds to –0.517 V vs. 3M Ag/AgCl electrode).

Furthermore, the authors of many studies state that thermal annealing, especially in a selenium atmosphere, is a powerful tool for controlling the defect structure and, consequently, the photoelectrophysical properties. The main goal of this type of annealing is to compensate for selenium loss and eliminate selenium-deficient defects (V_{Se} vacancies), which are deep recombination centers. Annealing facilitates the passivation of acceptor levels associated with copper vacancies V_{Cu} and gallium vacancies V_{Ga} [16]. For example, annealing in a Se atmosphere drastically reduces the resistivity of *p*-type CGS films to 1–10 Ω·cm [17]. In some cases, the application of rapid thermal annealing to finished CGS-based solar cells has increased their efficiency from 10 % to 11.46 % due to grain boundary passivation and improved heterojunction quality [18]. For high efficiency of AGS-based photocathodes, annealing in a selenium atmosphere at 600 °C is typically required [19], since at low annealing temperatures the samples are a mixture of Ag, Ga_2Se_3, GaSe phases and the target $AgGaSe_2$ phase. Reference [20] describes the fabrication of AGS-based photocathodes without a heterojunction; the photocurrent density value was 0.2 mA/cm² (at a potential of $E = -0.1$ V vs. RHE) under

illumination with light of wavelength 420–800 nm (Xe lamp, power 300 W). Of particular interest are $Ag_xCu_{1-x}GaSe_2$ solid solutions, as photocathodes based on them show higher photocurrent values. Reference [20] describes the production of films of mixed composition, in which ~6 % of the copper is substituted by silver atoms. The obtained photocathode with the structure $FTO/Ag_{0.06}Cu_{0.94}GaSe_2/CdS/Pt$ exhibited a photocurrent density of 8.1 mA/cm² (at a potential of $E = 0$ V vs. RHE). In turn, the photocathode without a heterojunction, $FTO/Ag_{0.06}Cu_{0.94}GaSe_2$, had photocurrent density values $j_{ph} \sim 1.4$ mA/cm² (at a potential of $E = 0$ V vs. RHE).

In our previous studies [21, 22], it was established that in the powder system of $Ag_xCu_{1-x}GaSe_2$ solid solutions, an increase in the silver fraction leads to an increase in the lifetime of photogenerated carriers, and the best photocurrent values were characteristic of powders with a higher silver content. This phenomenon is explained by the substitution of deep traps with shallower ones. However, such compositions have not been investigated as photocathodes for direct water splitting in photoelectrochemical cells.

Therefore, this paper studied the influence of synthesis conditions of $Ag_xCu_{1-x}GaSe_2$ thin films on their phase composition, structure, and their applicability as photocathodes for direct water splitting in photoelectrochemical cells.

Experimental section

The synthesis of $Ag_xCu_{1-x}GaSe_2$ thin films was carried out in several stages. In the first stage, intermetallics of various compositions, $CuGa_2$ and Ag_2Ga_3, were obtained by high-temperature solid-state synthesis. In the next synthesis stage, metals and intermetallics of the required mass were thermally evaporated in vacuum onto a pre-heated Mo/MoO_x substrate. The final stage of the synthesis was annealing the obtained films in an active selenium atmosphere. This method for synthesizing chalcopyrite films of other compositions was developed by us earlier [23] and has proven successful. The obtained films had the following structure: Mo (500 μm)/MoO_x (0.05 μm)/$Ag_xCu_{1-x}GaSe_2$ (1.50 μm).

The phase composition of the films was studied by XRD (PANalytical Aeris, Cu-K_α radiation). The applicability of the obtained films as photocathodes was investigated in a three-electrode electrochemical cell with a working electrode of glass/Mo/MoO_{3-x}/$Ag_xCu_{1-x}GaSe_2$ film, a graphite counter electrode, and a reference electrode, a 3 M silver/silver chloride electrode (AgCl), under pulsed illumination conditions close to AM1.5 (metal halide lamp, $P = 0.1$ W/cm²). To increase the shunt resistance, the edges of the sample were insulated. The electrolyte used was a solution containing CH_3COOH (0.1 M) + CH_3COOK (0.175 M) + K_2SO_4 (0.1 M) (acetate buffer with pH = 5), which helps reduce corrosion of the Mo/MoO_x substrates. The potential sweep rate was 5 mV/s.

Results and Their Discussion

Fig. 1*a* shows X-ray diffraction patterns of $AgGaSe_2$ films obtained under different conditions. For $AgGaSe_2$ films obtained at a temperature of 550 °C, a decrease in the amount of impurity phases with increasing annealing duration was characteristic. The films contain an impurity cubic chalcopyrite phase Ag_9GaSe_6 (*P*231), enriched with silver, a hexagonal GaSe phase (*P*63*mc*), and some phases that could not be identified. The intensity of the lines of the main $AgGaSe_2$ phase decreased with increasing annealing time. This change in intensities can be associated with the thermal decomposition of $AgGaSe_2$ into Ag_9GaSe_6 and the volatile Ga_2Se_3 phase upon increasing the heat treatment time. $AgGaSe_2$ films obtained at 650 °C contained the smallest amount of impurity phases compared to those obtained at 550 °C. With increasing duration of heat treatment, the intensity of the lines of the main chalcopyrite phase increases and the amount of the impurity hexagonal GaSe phase (*P*63*mc*) decreases.

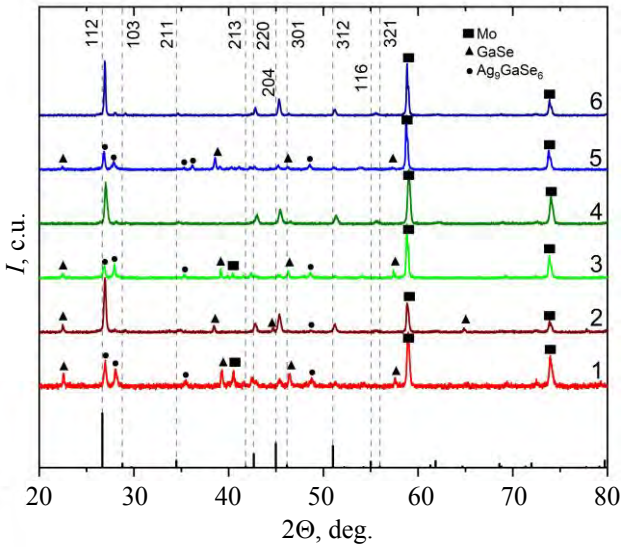

a)

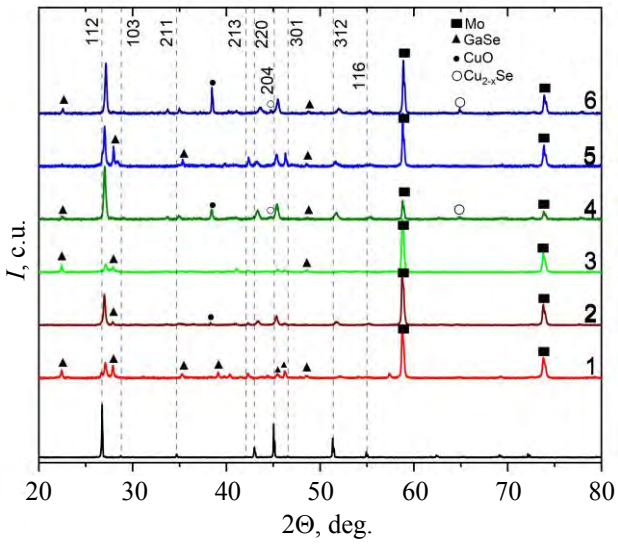

b)

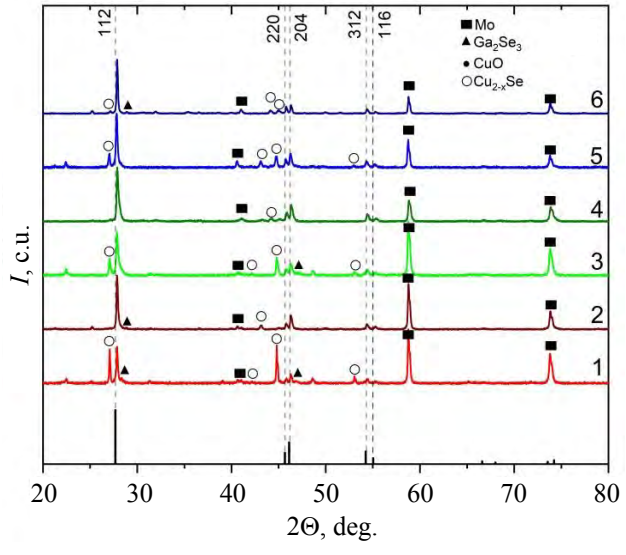

c)

Fig. 1. Diffraction patterns of $AgGaSe_2$ (a), $Ag_{0,9}Cu_{0,1}GaSe_2$ (b) and $CuGaSe_2$ (c) films obtained under conditions: 1) 550 °C, 10 min; 2) 650 °C, 10 min; 3) 550 °C, 15 min; 4) 650 °C, 15 min; 5) 550 °C, 30 min; 6) 650 °C, 30 min. The dashed lines indicate the reflections of the $AgGaSe_2$ and $CuGaSe_2$ standards, as well as the $Ag_{0,9}Cu_{0,1}GaSe_2$ powder [21]

For $Ag_{0,9}Cu_{0,1}GaSe_2$ films (Fig. 1*b*) annealed at 550 °C, an increase in the intensity of the main phase and a decrease in the intensity of the impurity GaSe phase are observed. For films obtained at 650 °C, although an increase in the intensity of the lines of the main chalcopyrite phase is observed with increasing annealing time, impurity phases of cubic $Cu_{2-x}Se$ (*F*-43*m*) and hexagonal GaSe (*P*63*mc*) are still present. This may be because, although the target $Ag_{0,9}Cu_{0,1}GaSe_2$ phase forms at elevated temperature, it begins to decompose with excessively long annealing times.

For $CuGaSe_2$ films (Fig. 1*c*) annealed at 550 °C, the presence of impurity phases of cubic (*F*-43*m*) $Cu_{2-x}Se$ and Ga_2Se_3 was characteristic for different annealing durations. Probably, this time at this temperature is insufficient for the formation of a single-phase film, since copper and selenium form a large number of intermediate selenides and equilibrium in the system does not have time to establish. For $AgGaSe_2$ films, for example, this is not observed, since only the Ag_2Se phase exists and less time is required to achieve equilibrium in the system. The higher annealing temperature of 650 °C, as well as increasing the duration of heat treatment, also does not significantly affect the composition of the obtained $CuGaSe_2$ films.

The crystal lattice parameters a, c and the unit cell volume *V* for $Ag_xCu_{1-x}GaSe_2$ films obtained under different conditions varied nonlinearly. Moreover, for $CuGaSe_2$ samples, only films obtained at 650 °C with an annealing time of 30 min have the closest values of crystal lattice parameters a = 5.611(6) Å, c = 10.989(25) Å

and $V = 346.0(6)$ Å³ compared to powders of the same composition [21, 22]. Among the samples containing silver, only $Ag_{0.9}Cu_{0.1}GaSe_2$ films obtained at 650 °C with an annealing time of 15 min, and $AgGaSe_2$ films obtained at 650 °C with an annealing time of 30 min, had similar crystal lattice parameter values $a = 5.937(9)$ Å, $c = 10.87(7)$ Å and $V = 380.0(21)$ Å³ and $a = 5.976(4)$ Å, $c = 10.702(23)$ Å and $V = 382.3(5)$ Å³, respectively, compared to powders of the same composition [21, 22].

Fig. 2 shows the current-voltage characteristics under intermittent illumination, which best represent the electrophysical properties of $Ag_xCu_{1-x}GaSe_2$ films obtained under different conditions. As can be seen from the figure, films of different compositions exhibit *p*-type dark conductivity, as evidenced by the increase in photocurrent amplitude upon shifting to the negative potential region. The increase in photocurrent density correlates with the increase in the lifetime of photogenerated charge carriers for powders of similar composition, described by us in [21, 22].

Based on the studied current-voltage curves, the photocurrent density values j_{ph} were obtained for films with the best photoelectrophysical characteristics. Furthermore, based on the studied current-voltage curves, the series (R_s) and shunt (R_{sh}) resistances were calculated from the relations: $\frac{1}{R_{sh}} \sim \left[\frac{dI}{dE}\right]$ at $E \to 0$, $\frac{1}{R_{sh}} \sim \left[\frac{dI}{dE}\right]$ at $I \to 0$, where I is current, E is potential [24]. Based on the known thickness and area of the synthesized films, the resistivity values (ρ) were calculated. The table presents summary data with these values for $Ag_xCu_{1-x}GaSe_2$ films obtained under different conditions. For comparison with data available in the literature [14, 20], the photocurrent density values recalculated relative to 3M Ag/AgCl are also given.

As can be seen from the table, for the $CuGaSe_2$ composition, the best photocurrent density values $j_{ph} = 0.066$ mA/cm² (at $E = -0.517$ V vs. 3M Ag/AgCl) are exhibited by $CuGaSe_2$ samples annealed at 650 °C for 10 min, which is in good agreement with literature data for this type of semiconductor material [14, 15]. For $AgGaSe_2$-based samples, the best photocurrent $j_{ph} = 0.132$ mA/cm² (at $E = -0.517$ V vs. 3M Ag/AgCl) was obtained for films annealed at 550 °C for 30 min. The shunt and series resistance values are relatively low. The obtained photocurrent density data are in good agreement with [20]. For photocathodes with the structure $Mo/MoO_x/Ag_{0.9}Cu_{0.1}GaSe_2$, annealed at 550 °C for 15 min, a record photocurrent density value of 1.763 mA/cm² (at $E = -0.517$ V vs. 3M Ag/AgCl) was achieved under illumination conditions close to AM1.5, compared to devices based on similar chalcopyrites described in the world literature [14, 15, 20]. The material of this sample exhibits low series resistance $R_s = 0.5$ kΩ and resistivity ρ = 0.2 MΩ·cm. Thus, based on the combination of our data and literature data [20], it can be concluded that the efficiency in $Ag_xCu_{1-x}GaSe_2$ solid solutions varies nonlinearly. In the range $0 \le x \le 0.06$, a significant increase in photocurrent density is observed, then in the range $0.06 \le x \le 0.2$ a strong decrease in j_{ph} occurs, followed by another increase up to $x = 0.9$. The obtained electrophysical characteristics of the films correlate well with the lifetime data for powders of similar mixed composition $Ag_xCu_{1-x}GaSe_2$, in which the best values were obtained for samples with high silver concentrations [21, 22]. The observed phenomenon may be due to a change in the defect structure of the samples, namely, a decrease in the depth and number of traps for charge carriers. With an increase in the silver content in the samples, a sequential substitution of deep acceptor levels by shallow donor levels occurs.

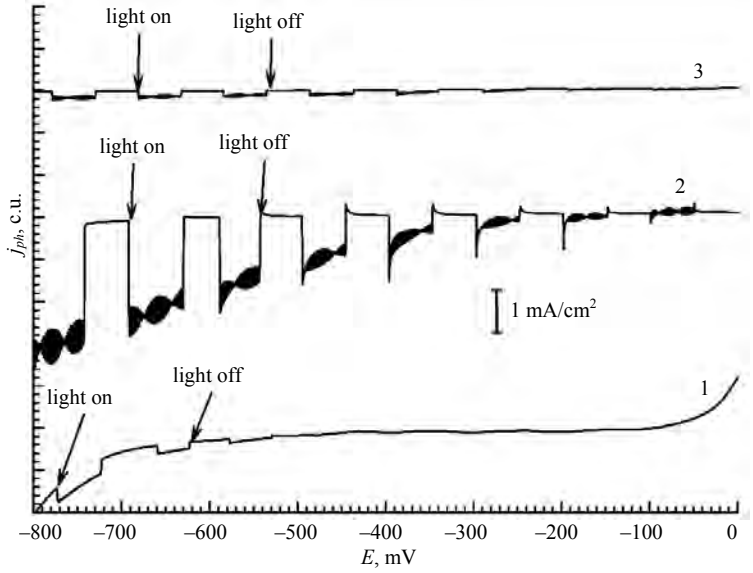

Fig. 2. Current-voltage characteristics (vs. 3M Ag/AgCl) under intermittent light illumination of $Ag_xCu_{1-x}GaSe_2$ films obtained under different conditions: (1) – $CuGaSe_2$ (550 °C, 30 min); (2) – $Ag_{0.9}Cu_{0.1}GaSe_2$ (550 °C, 15 min); (3) – $AgGaSe_2$ (650 °C, 10 min)

Table

Photocurrent density j_{ph}, series R_s and shunt R_{sh} resistance values for $Ag_xCu_{1-x}GaSe_2$ films obtained under different conditions

Film composition	Synthesis conditions	j_{ph}, mA/cm² (at E = –0.517 V vs. 3M AgCl electrode)	R_s, kΩ	R_{sh}, kΩ	ρ, MΩ·cm
$CuGaSe_2$	550 °C 10 min	0.017	2.8	6.6	0.9
	550 °C 15 min	0.026	71.3	92.2	23.8
	550 °C 30 min	0.015	39.1	53.5	13.0
	650 °C 10 min	**0.066**	**5.0**	**0.5**	**1.7**
	650 °C 15 min	0.026	4.4	7.3	1.5
	650 °C 30 min	0.011	5.4	4.9	1.8
$Ag_{0,9}Cu_{0,1}GaSe_2$	550 °C 10 min	0.049	147.5	37.8	49.2
	550 °C 15 min	**1.763**	**0.5**	**2.2**	**0.2**
	550 °C 30 min	0.16	7.9	4.8	2.6
	650 °C 10 min	0.029	6.0	17.3	2.0
	650 °C 15 min	0.075	65.3	2.9	21.8
	650 °C 30 min	0.0074	8.2	5.8	2.7
$AgGaSe_2$	550 °C 10 min	0.014	1.2	12.3	0.4
	550 °C 15 min	0.029	0.7	16.2	0.2
	550 °C 30 min	**0.132**	**0.5**	**7.4**	**0.2**
	650 °C 10 min	0.012	26.2	59.7	8.7
	650 °C 15 min	0.035	0.5	2.6	0.2
	650 °C 30 min	0	–	–	–

Conclusion

A study was conducted on the influence of stoichiometry and synthesis conditions on the phase composition, structure, and electrophysical properties of $Ag_xCu_{1-x}GaSe_2$ chalcopyrite thin films on Mo/MoO_x substrates. It was established that for the synthesis of $Ag_xCu_{1-x}GaSe_2$ films ($x = 0$, 0.9, and 1) on Mo/MoO_x substrates, annealing in selenium vapor at $T = 650$ °C for a duration of 15 min to 30 min is most optimal. Under these conditions, films with a chalcopyrite

structure of the space group *I*-42d are formed, with crystal lattice parameters closest to those of powders of similar composition. At the same time, electrodes based on $Ag_{0.9}Cu_{0.1}GaSe_2$ chalcopyrite composition, obtained at $T = 550$ °C and $t = 15$ min, possess the best electrophysical properties and the highest efficiency. In our opinion, the presence of small amounts of these impurity phases in the films does not significantly affect the photocurrent; a more significant contribution is made by the stoichiometry of the photoactive phase. On such samples, under pulsed illumination conditions close to AM1.5, a record photocurrent density $j_{ph} = 1.763$ mA/cm² (at $E = –0.517$ V vs. 3M Ag/AgCl) was achieved. The efficiency of electrodes based on $Ag_xCu_{1–x}GaSe_2$ solid solutions varies nonlinearly across the entire range of x. The increase in j_{ph} correlates with the increase in the lifetime of photogenerated charge carriers for powders of similar composition, which may be due to a change in the defect structure of the samples, namely, a decrease in the depth and number of traps for charge carriers.

The study was carried out with the financial support of the Russian Science Foundation (Agreement No. 24-43-10003) and the Belarusian Republican Foundation for Fundamental Research (grant No. T23RNFM-029).

REFERENCES

1. Kudo A. and Miseki Y., Chemical Society Reviews **38**, 253 (2009).
2. Eidsvåg H., Bentouba S., Vajeeston P., Yohi S., and Velauthapillai D., Molecules **26**, 1687 (2021).
3. Shafiq I., Hussain M., Shehzad N., Maafa I. M., Akhter P., Shafique S., Razzaq A., Yang W., Tahir M., and Russo N., J. Environmental Chemical Engineering **7** (4), 103265 (2019).
4. Abdi F. F., Han L., Smets A. H., Zeman M., Dam B., and Van De Krol R., Nature Communications **4** (1) 2195 (2013).
5. Pihosh Y., Turkevych I., Mawatari K., Uemura J., Kazoe Y., Kosar S., Makita K., Sugaya T., Matsui T., Fujita D., and Tosa M., Scientific reports **5** (1), 11141 (2015).
6. Kosar S., Pihosh Y., Turkevych I., Mawatari K., Uemura J., Kazoe Y., Makita K., Sugaya T., Matsui T., Fujita D., and Tosa M., Japanese journal of applied physics **55** (4S), 04ES01 (2016).
7. May M. M., Lewerenz H. J., Lackner D., Dimroth F., and Hannappel T., Nature Communications **6** (1) 8286 (2015).
8. Del Valle F., Ishikawa A., Domen K., De La Mano J. V., Sánchez-Sánchez M. C., González I. D., Herreras S., Mota N., Rivas M. E., Galván M. Á., and Fierro J. L. G., Catalysis Today **143** (1-2), 51–56 (2009).
9. Turner J. A., Science **305**, 972 (2004).
10. Barreto L., Makihira A., and Riahi K., Int. J. Hydrogen Energy **28**, 267 (2003).
11. Leijtens T., Bush K. A., Prasanna R., and McGehee M. D., Nat. Energy **3**, 828 (2018).
12. Jacobsson J., Fjällström V., Edoff M., and Edvinssona T., Sol. Energy Mater. Sol. Cells **138**, 87 (2015).
13. Ishizuka Sh., Okamoto R., and Ikeda Sh., Adv. Mater. Interfaces **9** (25), 2201266 (2022).
14. Mahmoudi B., Caddeo F., Lindenberg T., Schneider T., Hölscher T., Scheer R., and Maijenburg A. W., Electrochim. Acta **367**, 137183 (2021).
15. Ikeda S., Fujita W., Katsube R., Nose Y., Suzuki H., Abe R., and Yoshino K., Electrochimica Acta **454**, 142384 (2023).
16. Ponomareva I. P., Serov A. Yu., and Bodnar I. V., Physics of the Solid State **49** (1), 23–27 (2007) [in Russian].
17. Ramakrishna Reddy K. T. and Jayarama Reddy P., Thin Solid Films **253**, 238–242 (1994).
18. Karthikeyan S., Hwang S., Sibakoti M., Bontrager T., Liptak R. W., and Campbell S. A., Appl. Surf. Sci. **493**, 105–111 (2019).
19. Jung S. and Kim J., J. Nanosci. Nanotechnol **16** (5), 5279–5284 (2016).
20. Zhang L., Minegishi T., Kubota J., and Domen K., Phys. Chem. Chem. Phys. **16**, 6167 (2014).
21. Rakitin V. V., Gapanovich M. V., Lutsenko D. S., Nazarov V. B., Stanchik A. V., Gremenok V. F., and Kabyliatski A. V., High Energ. Chem. **58** (5), 492–498 (2024).
22. Rakitin V. V., Gapanovich M. V., Rabenok E. V., Kalimullina D. R., Lutsenko D. S., Kulemetev I. D., Koltsov E. N., Stanchik A. V., and Gremenok V. F., Condensed Matter and Interphases **27** (3), 441 (2025) [in Russian].

23. Aldoshin S. M., Bocharova S. I., Novikov G. F., and Gapanovich M. V. Method of manufacturing photosensitive chalcopyrite films. Patent for invention № RU 2567191 C1 (RF). 2015 [in Russian].
Das D. and Damodare L., Mater. Chem. Phys. **56** (2), 116–124 (1998).

About authors

Rakitin Vladimir Valerievich, Candidate of Chemical Sciences, Senior Researcher, Federal Research Center on Problems of Chemical Physics and Medicinal Chemistry, Russian Academy of Sciences (1 Ac. Semenov Ave., Chernogolovka, Moscow Region, 142432, Russia). E-mail: domi-tyan@yandex.ru SPIN code: 2273-0113, Author ID https://elibrary.ru/author_profile.asp?id=897817, Orcid ID 0000-0001-6582-5212

Kulemetyev Ivan Denisovich, Student, Federal Research Center on Problems of Chemical Physics and Medicinal Chemistry, Russian Academy of Sciences (1 Ac. Semenov Ave., Chernogolovka, Moscow Region, 142432, Russia); Faculty of Fundamental Physical and Chemical Engineering, Moscow State University (1 Leninskie Gory, Moscow, 119991, Russia). E-mail: ivan-2002@bk.ru

Baklanova Ulyana Ruslanovna, Student, Federal Research Center on Problems of Chemical Physics and Medicinal Chemistry, Russian Academy of Sciences (1 Ac. Semenov Ave., Chernogolovka, Moscow Region, 142432, Russia); Faculty of Fundamental Physical and Chemical Engineering, Moscow State University (1 Leninskie Gory, Moscow, 119991, Russia). E-mail: ulyana.baklanova@mail.ru

Lutsenko Denis Sergeevich, Junior Researcher, Federal Research Center on Problems of Chemical Physics and Medicinal Chemistry, Russian Academy of Sciences (1 Ac. Semenov Ave., Chernogolovka, Moscow Region, 142432, Russia). E-mail: rylah161den@mail.ru Orcid ID 0009-0000-5788-7763

Stanchik Aliona Viktorovna, Candidate of Physical and Mathematical Sciences, Leading Researcher, Scientific-Practical Materials Research Centre, National Academy of Sciences of Belarus (19 Petrusya Brovki, Minsk, 220072, Republic of Belarus). E-mail: alena.stanchik@bk.ru Orcid ID 0000-0001-8222-8030, Scopus Author ID www.scopus.com/authid/detail.uri?authorId=57200500542

Rabenok Evgeniya Vitalievna, Candidate of Physical and Mathematical Sciences, Senior Researcher, Federal Research Center on Problems of Chemical Physics and Medicinal Chemistry, Russian Academy of Sciences (1 Ac. Semenov Ave., Chernogolovka, Moscow Region, 142432, Russia). E-mail: jane.rabenok@yandex.ru SPIN code: 6923-7417, Author ID 123644, Orcid ID 0000-0002-3500-6918

Gapanovich Mikhail Vyacheslavovich, Candidate of Chemical Sciences, Head of Group of Semiconductor and Nanocomposite Materials, Federal Research Center on Problems of Chemical Physics and Medicinal Chemistry, Russian Academy of Sciences (1 Ac. Semenov Ave., Chernogolovka, Moscow Region, 142432, Russia); Faculty of Fundamental Physical and Chemical Engineering, Moscow State University (1 Leninskie Gory, Moscow, 119991, Russia); Moscow Institute of Physics and Technology (9 Institutskiy per., Dolgoprudny, Moscow Region, 141701, Russia). E-mail: gmw1@mail.ru Orcid ID 0000-0002-9109-6532, Scopus Author ID www.scopus.com/authid/detail.uri?authorId=6506377278

PHYSICAL SCIENCE OF MATERIALS

UDC 53
EDN: POOARC
PACS: 33.20.-t

Comparative analysis of absorption spectra in zinc phthalocyanine films on different substrates

© S. I. Rasmagin* and V. I. Krasovskii

Prokhorov General Physics Institute of the Russian Academy of Sciences, Moscow, 119991 Russia
** E-mail: rasmas123@yandex.ru*

Received 27.10.2025; revised 8.12.2025; accepted 20.02.2026

Films of butyl-substituted zinc phthalocyanine were fabricated on various substrates using vacuum deposition. Optical studies of the resulting films were conducted, during which their electronic absorption spectra were measured. Analysis of the characteristics of the electronic absorption spectra revealed a dependence of the properties of the butyl-substituted zinc phthalocyanine films on the nature of the substrates. It was established that the crystalline form of butyl-substituted zinc phthalocyanine films on the surfaces of organic and inorganic materials exhibits a metastable α-phase and a stable β-phase, respectively. Further research revealed a significant influence of the interaction between butyl-substituted zinc phthalocyanine molecules and substrate molecules on the film properties. For the potential use of butyl-substituted zinc phthalocyanine films as an active element in gas sensors, it is necessary to consider the nature of the interaction between butyl-substituted zinc phthalocyanine molecules and substrate molecules.

Keyword: zinc phthalocyanine, films, glass, polyvinyl chloride, absorption spectrum, molecular orbitals.

DOI: 10.51368/2949-561X-2026-1-68-72

Introduction

The optical and electrophysical properties of inorganic semiconductors (silicon, germanium, gallium arsenide, etc.) have been studied quite thoroughly. The majority of microelectronic devices are based precisely on the inorganic semiconductors listed above. To analyze the properties of inorganic semiconductors, band theory was developed, which describes the electron spectrum in a periodic crystal potential reasonably well [1]. Alongside inorganic semiconductors, organic semiconductors are widely used in areas such as solar cells, gas sensors, displays, biosensors, etc. Molecular orbital theory was developed to analyze the optical and electrophysical properties of organic semiconductors, and describes with varying degrees of approximation the energy states (spatial distribution and electron energy), types of molecular orbitals, the shape of organic molecules, etc.

Organic semiconductors include, in particular, metal phthalocyanines with conjugated carbon-carbon and nitrogen-carbon bonds. Metal phthalocyanines, both in solutions and in the form of films, are currently finding limited application in solar cells [2, 3, 4] and gas sensors [5, 6, 7]. In metal phthalocyanine molecules, fluorine atoms, chlorine atoms, butyl groups, and other substituents can be used instead of hydrogen atoms in the benzene rings. For example, the characteristics of zinc phthalocyanines with various substituents for hydrogen atoms in the benzene rings have been studied [8, 9]. The optical properties of metal phthalocyanine films also strongly depend on the nature of the substrates on which they are deposited [10]. In particular, zinc phthalocyanine films are capable of exhibiting semiconductor properties [11].

In this paper, samples of the organic semiconductor butyl-substituted zinc phthalocyanine were fabricated and investigated. All samples were obtained by vacuum deposition

onto different substrates. An inorganic material (silicate glass) and an organic substance (heat-treated polyvinyl chloride) were used as substrates. The aim of this paper was to study the influence of organic and inorganic substrates on the characteristics of the absorption spectra in butyl-substituted zinc phthalocyanine films and their polymorphic properties.

Experimental section

The butyl-substituted zinc phthalocyanine films were obtained by thermal vacuum deposition. Powder in the form of needle-shaped crystallites of butyl-substituted zinc phthalocyanine was the starting material, and silicate glass and heat-treated polyvinyl chloride (polyvinyl chloride-polyacetylene copolymer) were used as targets (substrates). The chemical formula of butyl-substituted zinc phthalocyanine with 8 butyl groups instead of hydrogen atoms in the benzene rings can be written as $ZnPcBu_8$, where the symbol Pc denotes the complex $C_{32}H_8N_8$, and Bu denotes butyl, C_4H_9. The films of butyl-substituted zinc phthalocyanine on glass and on the polyvinyl chloride-polyacetylene (PVC-PAC) film were designated as $ZnPcBu_8$ – SG and $ZnPcBu_8$ – PVC-PAC, respectively. The films of butyl-substituted zinc phthalocyanine on the PVC-PAC film and on silicate glass were obtained by sublimation of the $ZnPcBu_8$ powder at a heating temperature of 380 °C for 10 min. The crystalline structures of $ZnPcBu_8$ films exist mainly in two forms: a metastable α-form and a stable β-form. The crystalline structure of metallophthalocyanine films is influenced by several deposition parameters, including the substrate material. This study investigated the influence of the substrate material on the crystalline structure of $ZnPcBu_8$ films.

The deposition of butyl-substituted zinc phthalocyanine films onto the substrates was carried out in a VUP-5 vacuum system. The light absorption spectra in the butyl-substituted zinc phthalocyanine films were obtained using an Option Optics 2000 spectrometer with a dynamic range of 300–1100 nm. A 10 mW tungsten lamp was used as the radiation source.

Results and Their Discussion

For the butyl-substituted zinc phthalocyanine films on silicate glass and on the PVC-PAC surface, the radiation absorption spectra were measured at a measurement temperature of T = 22 °C (figure).

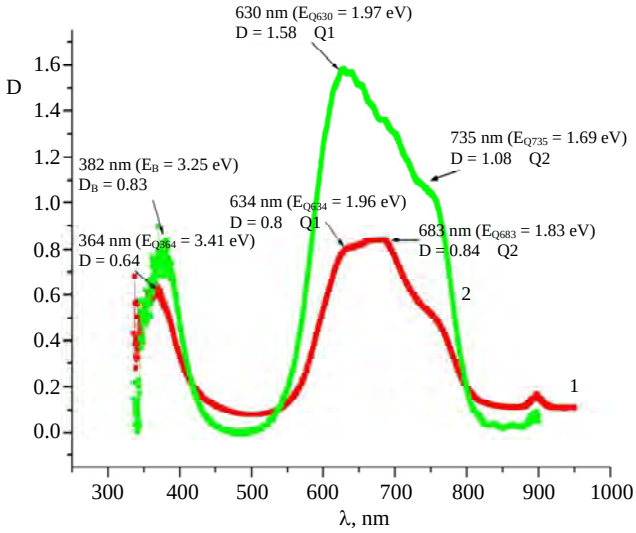

Fig. Absorption spectra of butyl-substituted zinc phthalocyanine films: 1 – $ZnPcBu_8$ film on glass, 2 – $ZnPcBu_8$ film on PVC-PAC

The absorption spectrum of the $ZnPcBu_8$ – SG film has two characteristic bands in the visible radiation range: the Q-band in the range of 550–800 nm and the B-band in the range of 350–500 nm. In the absorption spectrum, the B-band has one absorption peak, and the Q-band has two absorption peaks. The first peak of the Q-band corresponds to a wavelength of λ_{Q1} = 634 nm (E_{Q1} = 1.96 eV), the second peak of the Q-band corresponds to a wavelength of λ_{Q2} = 683 nm (E_{Q2} = 1.83 eV). The half-width of the Q-band is approximately $\Delta\lambda_{Q1/2}$ = 170 nm. The peak of the B-band corresponds to a wavelength of λ_B = 364 nm (E_B = 3.41 eV). The full width at half maximum of the B-band is approximately $\Delta\lambda_{B1/2}$ = 64 nm.

The absorption spectrum of the $ZnPcBu_8$ – PVC-PAC film has two characteristic absorption bands: the Q-band in the range of 500–850 nm and the B-band in the range of 350–500 nm. In the absorption spectrum, the B-band has one absorption peak, and the Q-band has two extreme absorption peaks (see figure). The first peak of the Q-band corresponds to a wavelength of

λ_{Q1} = 630 nm (E_{Q1} = 1.97 eV), the second peak of the Q-band corresponds to a wavelength of λ_{Q2} = 735 nm (E_{Q2} = 1.69 eV). The half-width of the Q-band is approximately $\Delta\lambda_{Q1/2}$ = 188 nm. The peak of the B-band corresponds to a wavelength of λ_B = 382 nm (E_B = 3.25 eV). The full width at half maximum of the B-band is approximately $\Delta\lambda_{B1/2}$ = 57 nm or in energy units $E_{B1/2}$ = 0.51 eV.

Molecules of butyl-substituted zinc phthalocyanine in the $ZnPcBu_8$ – SG and $ZnPcBu_8$ – PVC-PAC films form molecular crystallites due to van der Waals interactions and short-range repulsive forces. Coulomb forces act over a longer range between the Zn^{2+} ions of different $ZnPcBu_8$ molecules. The interaction of butyl-substituted zinc phthalocyanine molecules in the $ZnPcBu_8$ – SG and $ZnPcBu_8$ – PVC-PAC films occur due to van der Waals forces at a close range of about 0.35 nm and Coulomb forces at a long range of about 0.38 nm for the α-phase and, accordingly, at a close range of 0.32 nm and a long range of 0.49 nm for the β-modification of $ZnPcBu_8$.

The butyl-substituted zinc phthalocyanine molecule has 38 delocalized π-electrons. In the macrocycle of $ZnPcBu_8$, there are 18 delocalized π-electrons, and 20 delocalized π-electrons are located in the 4 isoindole groups. Upon light absorption, the delocalized π-electrons of the $ZnPcBu_8$ molecule transition from the ground state to excited electronic states. For the absorption spectra in the $ZnPcBu_8$ – SG and $ZnPcBu_8$ – PVC-PAC films, the Q-band corresponds to the singlet-singlet electronic transition $S_0 \rightarrow S_1$, and the B-band corresponds to the singlet-singlet electronic transition $S_0 \rightarrow S_2$. The butyl-substituted zinc phthalocyanine molecule is characterized by the D_{4h} point group symmetry, which corresponds to a planar square spatial structure. The molecular orbitals of the butyl-substituted zinc phthalocyanine molecule with the D_{4h} point group symmetry are characterized by the symmetry of the molecular orbitals a_{1u}, a_{2u}, b_{1u}, b_{2u}, and e_g. Light absorption in the Q-band in the $ZnPcBu_8$ – SG and $ZnPcBu_8$ – PVC-PAC films occurs at the conjugated double carbon-carbon bonds of the benzene rings (n = 13) and the conjugated double nitrogen-carbon bonds (m = 6) in the macrocycle. Here, n is designated as the number of conjugated double carbon-carbon bonds C=C and m as the number of conjugated double carbon-nitrogen bonds C=N. According to Davydov's theory, in the crystalline structures of metal phthalocyanines (MPc), the splitting of the Q-band into two peaks is caused by the interaction of MPc molecules with each other (dipole-dipole interaction of neighboring molecules). The degree of splitting of the Q-band into two peaks characterizes the interaction energy between MPc molecules that are in positions with different symmetry groups [12]. In the $ZnPcBu_8$ – SG film, the Q-band in the absorption spectrum splits into two peaks: an absorption peak Q1 λ_m = 634 nm (E = 1.96 eV) and an absorption peak Q2 λ_m = 683 nm (E = 1.82 eV) (see figure). Here, the doubly degenerate molecular orbital LUMO $1e_g(\pi^*)$ splits into two molecular orbitals, LUMO+1 and LUMO-1. The absorption peak Q1 (E = 1.96 eV) corresponds to the electronic transition from HOMO $1a_{1u}(\pi)$ to LUMO+1, and the absorption peak Q2 (E = 1.82 eV) corresponds to the electronic transition from HOMO $1a_{1u}(\pi)$ to LUMO-1. The figure shows that the optical density D of the high-energy peak Q1 (E = 1.96 eV) is lower than that of the low-energy absorption peak Q2 (E = 1.82 eV). This ratio of optical densities in the absorption spectrum indicates that the arrangement of zinc phthalocyanine molecules in the $ZnPcBu_8$ – SG film is in the stable β-phase [13, 14, 15]. It should be noted that the peaks Q1 (λ_m = 634 nm) and Q2 (λ_m = 683 nm) of the absorption spectra of the $ZnPcBu_8$ film practically coincide with the peaks at 632 and 689 nm of the ZnPc film in reference [15]. This may indicate that in the β-phase $ZnPcBu_8$ film, replacing the hydrogen atoms in the benzene rings with a butyl group does not significantly change the energy of the electronic transitions in the Q-band. The absorption peak of the B-band with a wavelength of λ_m = 364 nm (E_B = 3.41 eV) is caused by the electronic transition from the HOMO-1 $1a_{2u}(\pi)$ molecular orbital to the LUMO $1e_g(\pi^*)$ molecular orbital. It is worth noting that the absorption peak of the B-band at λ_m = 364 nm (E_B = 3.41 eV) of the $ZnPcBu_8$ film differs from the absorption peak of the B-band at λ_m = 340 nm (E_B = 3.65 eV) of the ZnPc film in reference [15] by 24 nm (or 0.24 eV). This indicates that replacing the hydrogen atoms in the benzene rings with butyl groups increases

the energy of the electronic transitions in the B-band by 0.24 eV. It can be assumed that the electronic transition HOMO-1 $1a_{2u}(\pi) \rightarrow$ LUMO $1e_g(\pi^*)$ in the $ZnPcBu_8$ film, compared to the ZnPc film, occurs to a lower vibrational level of the $1e_g(\pi^*)$ molecular orbital.

In the $ZnPcBu_8$ – PVC-PAC film, the Q-band in the absorption spectrum splits into two extreme peaks: an absorption peak Q1 $\lambda_m = 630$ nm (E = 1.97 eV) and an absorption peak Q2 $\lambda_m = 738$ nm (E = 1.68 eV) (see figure). Consequently, the doubly degenerate molecular orbital LUMO $1e_g(\pi^*)$ splits into two molecular orbitals, LUMO+1 and LUMO-1, upon interaction between $ZnPcBu_8$ molecules. The absorption peak Q1 (E = 1.97 eV) corresponds to the electronic transition from HOMO $1a_{1u}(\pi)$ to LUMO+1, and the absorption peak Q2 (E = 1.82 eV) corresponds to the electronic transition from HOMO $1a_{1u}(\pi)$ to LUMO-1. The figure shows that the optical density D of the high-energy peak Q1 (E = 1.97 eV) is greater than that of the low-energy absorption peak Q2 (E = 1.69 eV). This ratio of optical densities indicates that the zinc phthalocyanine molecules in the $ZnPcBu_8$ – PVC-PAC film are in the metastable α-phase [13, 14, 15].

Thus, the crystalline form of butyl-substituted zinc phthalocyanine on the surfaces of PVC-PAC and silicate glass has the metastable α-phase and the stable β-phase, respectively. The different polymorphism of the crystalline $ZnPcBu_8$ films has a noticeable effect on the characteristics of the film absorption spectra. It should be noted that for the development of gas sensors based on butyl-substituted zinc phthalocyanine deposited onto inorganic and organic substrates, it is necessary to consider the nature of the interaction between the butyl-substituted zinc phthalocyanine molecules and the substrate molecules.

Conclusion

A study was conducted on the influence of organic (polyvinyl chloride-polyacetylene) and inorganic (silicate glass) substrates on the polymorphism of butyl-substituted zinc phthalocyanine films. The influence of the polymorphism of butyl-substituted zinc phthalocyanine on the characteristics of the light absorption spectra was revealed. The influence of polymorphism on the electronic transitions in butyl-substituted zinc phthalocyanine films was established.

As a result of the performed analysis of the absorption spectra of butyl-substituted zinc phthalocyanine films on organic and inorganic substrates, the following conclusions were drawn:

1. In crystalline films of $ZnPcBu_8$ – PVC-PAC in the α-phase and $ZnPcBu_8$ – SG in the β-phase, the Q-band in the absorption spectra splits into two main peaks. The high-energy peak Q1 is caused by the electronic transition from the HOMO $1a_{1u}(\pi)$ molecular orbital to the LUMO+1 molecular orbital with an energy $E_{Q1} = 1.97$ eV. The low-energy peak Q2 is caused by the electronic transition from the HOMO $1a_{1u}(\pi)$ molecular orbital to the LUMO-1 molecular orbital with an energy $E_{Q2} = 1.69$ eV.

2. In the crystalline film $ZnPcBu_8$ – SG in the β-phase, the Q-band in the absorption spectrum splits into two main peaks. The high-energy peak Q1 is caused by the electronic transition from the HOMO $1a_{1u}(\pi)$ molecular orbital to the LUMO+1 molecular orbital with an energy $E_{Q1} = 1.96$ eV. The low-energy peak Q2 is caused by the electronic transition from the HOMO $1a_{1u}(\pi)$ molecular orbital to the LUMO-1 molecular orbital with an energy $E_{Q2} = 1.83$ eV.

3. For the $ZnPcBu_8$ – SG film in the β-phase, the energy $E_{Q2\text{-}\beta}$ of the HOMO $1a_{1u}(\pi) \rightarrow$ LUMO-1 electronic transition is 0.14 eV higher than the energy $E_{Q2\text{-}\alpha}$ in the $ZnPcBu_8$ – PVC-PAC film in the α-phase. Most likely, the electronic transition in the α-phase $ZnPcBu_8$ film occurs to a lower energy vibrational level compared to the $ZnPcBu_8$ – SG film in the β-phase. It can also be assumed that the energy level of LUMO-1 depends on the crystalline form of the films and, consequently, on the nature of the substrate.

4. The energy of the electronic transitions for the absorption peaks of the B-band of butyl-substituted zinc phthalocyanine molecules differs for different substrates. For the $ZnPcBu_8$ – PVC-PAC film in the α-phase, the energy of the $1a_{2u}(\pi) \rightarrow 1e_g(\pi^*)$ electronic transition of the B-band is $E_{B\text{-}\alpha} = 3.25$ eV. For the $ZnPcBu_8$ – SG film in the β-phase, the energy of the $1a_{2u}(\pi) \rightarrow 1e_g(\pi^*)$ electronic transition of the

B-band is $E_{B-\beta}$ = 3.41 eV. For the $ZnPcBu_8$ – SG film in the β-phase, the energy of the electronic transition $E_{B-\beta}$ = 3.41 eV exceeds the energy $E_{B-\alpha}$ for the $ZnPcBu_8$ – PVC-PAC film in the α-phase by 0.07 eV.

Thus, we summarize the overall results of the studies of optical films of butyl-substituted zinc phthalocyanine on different substrates.

1. For $ZnPcBu_8$ – PVC-PAC films in the α-phase and $ZnPcBu_8$ – SG films in the β-phase, the energies of the HOMO $1a_{1u}(\pi) \rightarrow$ LUMO+1 electronic transitions, characteristic of the high-energy peak of the Q-band absorption spectra, are practically independent of the crystalline form of the films and, consequently, indirectly through the film polymorphism, independent of the nature of the substrate.

2. For $ZnPcBu_8$ – PVC-PAC films in the α-phase and $ZnPcBu_8$ – SG films in the β-phase, the energies of the HOMO $1a_{1u}(\pi) \rightarrow$ LUMO-1 electronic transitions, characteristic of the low-energy peak of the Q-band absorption spectra, depend on the crystalline form of the films and, consequently, indirectly through the crystalline form of the films, depend on the nature of the substrate.

REFERENCES

1. Bonch-Bruevich V. L. and Kalashnikov S. G. Semiconductor Physics. Moscow, Nauka, 1977 [in Russian].
2. Sekar N. and Ghelot V., Resonance **15**, 819–831 (2010). https://doi.org/10.12691/pmc-3-1-1
3. Rasmagin S. I., Optics and Spectroscopy **130** (12), 1893–1898 (2022). https://doi.org/10.21883/OS.2022.12.54097.3602-22
4. Walter M. G., Rudine A. B., and Wamser C. C., JPP **14**, 759–792 (2010).
5. Debliquy M., Lahem D., Bueno-Martinez A., and Caucheteur C., Sensors **18** (3), 740 (2018). https://doi.org/10.3390/s18030740
6. Bohrer F. I., Colesniuc C. N., Park J., Ruidiaz M. E., Schuller I. K., Kummel W. C., and Trogler W. C., Am. Chem. Soc. **131**, 478–485 (2009).
7. Rasmagin S. I., Optics and Spectroscopy **132** (6), 591–596 (2024). https://doi.org/10.61011/OS.2024.06.58635.6787-24
8. Mogileva T. N., Angelov I. P., Mantareva V. N., Eneva I. Z., and Mikheev G. M., Chemical Physics and Mesoscopy **18** (2), 281–287 (2016).
9. Chaidogiannos G., Petraki F., Glezos N., Kennou S., and Nešpůrek S., Appl. Phys. A: Mater. Sci. Process. **96**, 763–767 (2009).
10. Sindu Louis J., Lehmann D., Friedrich M., and Zahn D. R. T., J. Appl. Phys. **101**, 013503 (2007). https://doi.org/10.1063/1.2403845
11. Guillaud G. and Simon J. P., Coordination Chemistry Reviews **178**, 1433–1484 (1998).
12. Davydov A. S. Theory of molecular excitons. New York, McGraw-Hill, 1962.
13. Roy D., Das N. M., Shakti N. M., and Gupta P. S., RSC Adv. **4**, 42514–42522 (2014). https://doi.org/10.1039/C4RA05417B
14. Shahiduzzaman M., Horikawa T., Hirayama T., Nakano M., Karakawa M., Takahashi K., Nunzi J.-M., and Taima T., J. Phys. Chem. C **124**, 21338–21345 (2020). https://doi.org/10.1021/acs.jpcc.0c07010
15. Zanfolim A. A., Volpati D., Olivati C. A., Job A. E., and Constantino C. J. L., J. Phys. Chem. **114**, 12290–12299 (2010).

About authors

Rasmagin Sergey Iosifovich, Candidate of Physical and Mathematical Sciences, Senior Researcher, Prokhorov General Physics Institute of the Russian Academy of Sciences (38 Vavilov st., Moscow, 119991, Russia). E-mail: rasmas123@yandex.ru SPIN-code: 8350-5100, AuthorID: 41958

Krasovskii Vitaly Ivanovich, Candidate of Physical and Mathematical Sciences, Senior Researcher, Prokhorov General Physics Institute of the Russian Academy of Sciences (38 Vavilov st., Moscow, 119991, Russia). E-mail: krasovskii@nsc.gpi.ru SPIN-code: 8116-4994, AuthorID: 41957

PHYSICAL SCIENCE OF MATERIALS

UDC 53.083.8 PACS: 81.70.-q
EDN: QYJELI

Application of different methods for measuring modulus of elasticity of nanostructured materials on the example of titanium

© A. S. Useinov[1,2], G. Kh. Sultanova[1,3], I. V. Laktionov[1*], and A. P. Fedotkin[1]

[1] *Moscow Institute of Physics and Technology, Moscow Region, Dolgoprudny, 141701 Russia*
[*] *E-mail: laktionov@mipt.ru*
[2] *Vereshchagin Institute for High Pressure Physics Russian Academy of Sciences, Moscow, Troitsk, 108840 Russia*
[3] *National Research Center «Kurchatov Institute», Moscow, Troitsk, 108840 Russia*

Received 9.09.2025; revised 4.12.2025; accepted 20.02.2026

The article presents the results of a comparative study of various methods for determining the Young's modulus of nanostructured titanium obtained by equal-channel angular pressing followed by drawing. The approaches based on the Hertz model, the Oliver-Farr method of instrumental indentation, and dynamic mechanical analysis (DMA) are considered. It is shown that all methods allow to obtain the values of elastic modulus, which are in agreement with each other and close to the tabular data, while the differences are related to the phase of the loading process, which is taken into account in a particular model. The peculiarities of the spherical indenter application, which allows to restore the true stress-strain diagram, are analyzed. It is shown that at low loads the roughness of the indenter and the investigated surface, as well as the noise level, is the determining factor of accuracy. It is concluded that it is reasonable to measure Young's modulus by the method of instrumental indentation with subse quent use of this value in reconstructing the full stress-strain diagram from the data of indentation with a spherical tip.

Keywords: stress-strain diagram, modulus of elasticity, tool indentation, nanostructured titanium.

DOI: 10.51368/2949-561X-2026-1-73-78

Introduction

The assessment of the elastic characteristics of a material, primarily Young's modulus, plays a key role in engineering materials science, contact interaction mechanics, micro- and nanoelectronics, as well as in functional coating technologies. The elastic modulus determines not only the initial response of a material to external loads, but also is directly involved in calculations of durability, vibration resistance, and strength characteristics in structures of various scales.

Classical mechanical tests for uniaxial tension or compression are certainly the benchmark for constructing a stress-strain diagram, as they allow obtaining a complete picture of the material's mechanical behavior from the elastic to the fracture stage. However, the implementation of such tests requires samples of a specific shape and size that comply with standards (e.g., GOST 1497–84, ASTM E8/E8M) [1], which practically excludes the possibility of directly testing objects with a characteristic size less than 1 mm, thin coatings, g radient structures, or individual components of microelectromechanical systems (MEMS/NEMS). For such objects, local mechanical probing methods, in particular instrumented indentation, prove to be the most suitable [2].

One of the urgent tasks in this area is not just extracting individual mechanical parameters (such as hardness or elastic modulus), but also reconstructing the complete stress-strain curve from indentation data. Today, there are a number of methods for transitioning from the indentation diagram to the tensile hardening curve. In particular, the study [3] shows that the suitability of some simplified analytical models describing the complex stress state of bodies of non-conforming shape during contact has been established. Another approach, implemented within the ABI method or in multi-step loading-unloading cycles, allows extrapolating macromechanical characteristics to the micro level. However, the reliability of such reconstructions depends on many factors: calibration of the contact area, accuracy of force and depth measurement, choice of the contact interaction model (Hertz, Oliver-Pharr, etc.), as well as the correctness of assumptions about the stress distribution in the vicinity of the imprint.

Comparison of diagrams reconstructed from indentation data with reference diagrams obtained from macro-tests represents a critically important step for validating the contact methods and models underlying the processing of experimental data. Without such verification, it is impossible to reliably assert the equivalence of the obtained mechanical characteristics, especially under conditions where the stress and strain gradients in the local region significantly exceed the corresponding values in macroscopic tests. Such systematic studies are particularly important from the perspective of further investigation of gradient structures, layered and topocomposite materials [4], characterized by anisotropy of mechanical properties.

Thus, the development and testing of methods for measuring Young's modulus based on spatially localized measurements represents an important direction in experimental solid mechanics.

Methods

A common method for reconstructing the stress-strain diagram from indentation results is the automated ball indentation (ABI) technique [5]. Within this approach, a series of sequential loading-unloading cycles is performed with an increasing maximum applied normal force. The elastic and plastic characteristics of the material are determined from the reconstructed stress-strain diagram obtained by analyzing the accumulated indentation. A feature of this method is the possibility of directly reconstructing equivalent stresses and strains without prior knowledge of the cross-sectional area, which makes it particularly valuable for micro-volumes and inhomogeneous structures [6].

When transitioning to sub-micrometer indentation depths, correctly constructing the elastic portion of the stress-strain diagram using the ABI method becomes extremely difficult, because the measurement error becomes too large due to the small depths and applied loads. Therefore, to construct this portion, a strategy can be chosen in which Young's modulus, which characterizes the slope of the σ–ε diagram in the elastic deformation region, is determined by one of the alternative methods based on quasi-static or dynamic instrumented indentation.

Indentation with a spherical tip using the Hertz model

The first approach to estimating the elastic modulus is based on analyzing the loading curve when indenting with a spherical indenter. According to the classical Hertz theory, the contact between an elastic half-space and a rigid sphere is described by the analytical expression:

$$P = \frac{4}{3} E^* R^{\frac{1}{2}} h^{\frac{3}{2}},$$

where P is the load, h is the indentation depth, R is the radius of curvature of the indenter, and E^* is the reduced elastic modulus.

$$\frac{1}{E^*} = \frac{1-\nu_1^2}{E_1} + \frac{1-\nu_2^2}{E_2},$$

where E_1 and E_2 are the elastic moduli, and ν_1 and ν_2 are Poisson's ratios of the contacting bodies (indenter and specimen).

Approximating the experimental loading curves with the Hertz function allows determining E^*, and then, considering the elastic properties of the indenter material, Young's modulus of the material under study.

Instrumented indentation method

GOST R 8.748-2011 standard [7] regulates the procedure for determining the elastic modulus based on the analysis of the unloading segment during an indentation cycle. This uses the model proposed in the papers of Oliver and Pharr [8, 9], which relates the contact stiffness $S = dP/dh$ to the value of the reduced elastic modulus:

$$E^* = \frac{\sqrt{\pi}}{2\beta} \cdot \frac{S}{\sqrt{A}},$$

where A is the contact area, and β is a factor depending on the indenter geometry. After accounting for the indenter properties, Young's modulus of the material under study is calculated. For a spherical indenter geometry, $\beta = 1$.

Dynamic mechanical analysis (DMA)

The dynamic indentation mode is based on superimposing a harmonic excitation of small amplitude onto the main quasi-static indentation of the indenter into the material under study. The dynamic operating mode of the indenter allows recording the dependence of hardness, elastic modulus, and loss on the penetration depth in a single cycle mode.

The model of such interaction can be described in the first approximation as a system with forced harmonic oscillations, analogous to a damped oscillator. The external force signal has the form:

$$F(t) = F_{dc}(t) + F_{ac} \cdot \sin(\omega t),$$

where F_{dc} is the quasi-static load component, F_{ac} is the amplitude of the harmonic component, and ω is the angular excitation frequency.

The indenter displacement:

$$h(t) = h_{dc}(t) + h_{ac} \cdot \sin(\omega t + \delta),$$

where δ is the phase shift between excitation and response, determining the presence of a viscous material response.

Different materials can resist the applied load as elastic or viscous substances. The former store energy during deformation and return to their initial state upon load removal. The latter, which remain compressed after load removal, dissipate all the work of their deformation as heat.

When using the dynamic method, the deformation ε of the body depends on the frequency ω of the applied force as follows:

$$\varepsilon = \varepsilon_0 \sin(t\omega).$$

For a purely elastic body, Hooke's law holds, and the stress σ is proportional (with coefficient E – Young's modulus) to the strain:

$$\sigma = E\varepsilon.$$

Consequently, load and strain are in phase. In a viscous material, where there is no elastic deformation, the stress is given by Newton's law: $\sigma = \eta\dot{\varepsilon}$, and the stress arising in response to the load differs from it in phase by $\delta = 90°$ [10]:

$$\sigma = \sigma_0 \sin(t\omega + \delta).$$

However, absolutely elastic and absolutely inelastic bodies do not exist in nature. The imaginary and real components of Young's modulus $E^* = E' + iE''$ have the form:

$$E' = \frac{\sigma_0}{\varepsilon_0}\cos\delta,\ E'' = \frac{\sigma_0}{\varepsilon_0}\sin\delta.$$

From the analysis of the phase and amplitude of the response, the complex elastic modulus is measured, including the real part (storage modulus) E' and the imaginary part (loss modulus) E''. In this case, the storage modulus E' approximately corresponds to Young's modulus for linearly elastic materials.

Experimental procedure

Commercially pure titanium Grade 4, subjected to severe plastic deformation by equal-channel angular pressing using the Conform scheme (ECAP-C) followed by drawing, was used as the material for the comparative study. This method enables obtaining an ultrafine-grained structure through the accumulation of large plastic strains without changing the external geometry of the sample. ECAP-C was carried out using the KV-048.IFPM.043911001 setup (Research Institute of Physics of Advanced Materials of the Ufa University of Science and Technology and Limited Liability Company NanoMeT):

deformation temperature – 250 °C, channel intersection angle – 120°, processing route Bc, number of passes – 4. For uniform deformation, the billet was rotated by 90° around its axis before each pass. Drawing of the billets after ECAP-C was carried out to a rod diameter of 6 mm over 17 passes with a die diameter change step of 0.5 mm. The drawing temperature was 250 °C, and the deformation rate was 0.3 m/s.

Based on the results of X-ray diffraction analysis using the broadened lines method (Williamson–Hall analysis) [12], the average equivalent grain size was determined to be about 41 ± 2 nm, which confirms the formation of a nanostructured state. The sample surface was mechanically polished, providing a roughness level Ra < 5 nm, sufficient for high-precision indentation tests.

Measurements were carried out on a NanoScan-4D nanoindenter [13]. A spheroconical diamond tip made from a single-crystal diamond was used as the indenter. The radius of the spherical part of the tip was 2.5 μm, and the height of the working part was 1 μm. The tip area function was obtained from data from an Ntegra Prima scanning probe microscope.

Measurements using the static indentation method were carried out at a rate of 50 nm/s until a maximum load of 30 mN was reached. DMA tests were carried out up to the same maximum load and at the same loading rate, with an oscillation frequency of 10 Hz and amplitude of 20 nm, respectively.

Discussion of the results

The table presents the averaged measurement results obtained by different methods. The instrumented indentation data were obtained with a maximum load starting from 1 mN (Fig. 1).

Table

Elastic modulus values

Measurement method	Young's modulus value, GPa
Hertz model	107 ± 5
Instrumented indentation	104 ± 4
Dynamic mechanical analysis	97 ± 3
Tabulated value [11]	110 ± 10

The key difference in the approaches based on the Hertz model and the Oliver-Pharr method is that the elastic properties of the surface are determined in different phases of loading. The Hertz model describes the elastic response of the initial, undeformed surface in a small local area of the contact spot under the indenter. The Oliver-Pharr model describes the elastic response of the surface contour upon unloading at the end of the indentation procedure.

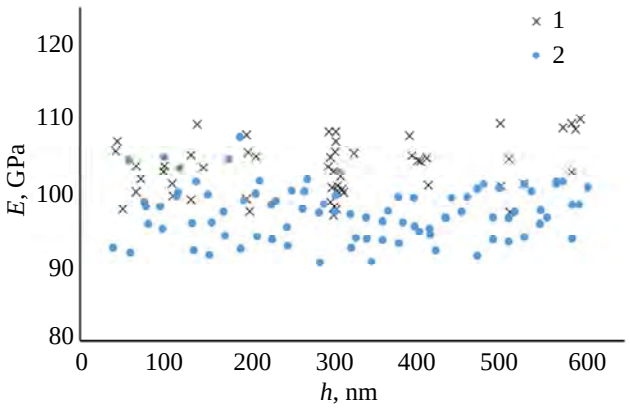

Fig. 1. Dependence of the elastic modulus on depth in instrumented indentation tests (1) and DMA (2)

To calculate the elastic modulus according to the Hertz formula, the initial section of the loading curve under static loading was approximated by a power function (Fig. 2). In this case, the load range in the elastic deformation region was less than 1 mN, which is consistent with the experimentally obtained dependence, as well as with the value calculated by the formula given in [5].

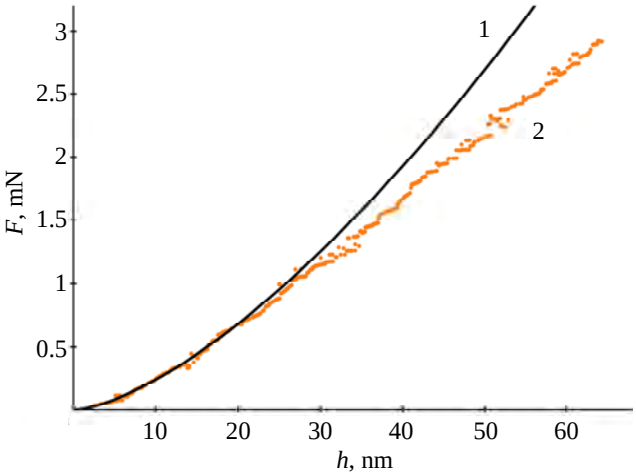

Fig. 2. Dependence of force on indentation depth: 1 – approximation of the elastic deformation section according to the Hertz model, 2 – experimental data

The Hertz theory was applied to describe the indentation of an ideal sphere into an elastic half-space. This model does not account for surface roughness. Moreover, the considered elastic deformation region is comparable to the roughness of the indenter. According to the Greenwood-Williamson theory for elastic deformation of micro-asperities (plasticity index < 2/3), the arithmetic mean surface roughness should be 1.1 nm. Exceeding this value by the actual surface roughness leads to an overestimated measured value and an increased measurement error.

The DMA method demonstrates lower elastic modulus values. During the DMA test, an oscillating load acts at a given loading rate. Therefore, the strain rate turns out to be higher than the rate of increase of the mean load and amounts to ~200 nm/s. To exclude the influence of strain rate for this material in this range of values, comparative tests were carried out using the instrumented indentation method with a maximum load of 15 mN and loading rates of 10, 50, 100, and 200 nm/s. No dependence of properties on loading rates was found in this range. An increase in the strain rate during dynamic tests of titanium leads to an increase in strength characteristics but does not affect the elastic modulus.

Conclusion

When constructing the stress-strain diagram in the elastic deformation region using a small-diameter spherical indenter, large errors arise related to the roughness of the indenter and the investigated surface, as well as to seismic noise.

In this study, various methods for determining the elastic modulus were investigated: using the Hertz model, the instrumented indentation method, and dynamic mechanical analysis. These methods demonstrate values that are close within the margin of error. To eliminate inaccuracies when constructing the σ–ε diagram in the elastic deformation region, it is proposed to use the value of the elastic modulus determined at large indentation depths in the region of plastic deformation of the material, for which instrumented indentation appears to be the most reliable method.

An advantage of using a spherical tip is the construction of the true stress diagram. Tensile test results of materials allow constructing an engineering stress diagram, which does not account for the change in cross-sectional area during tension.

The study was carried out with the financial support of the Russian Science Foundation, grant No. 25-29-00291.

REFERENCES

1. GOST 1497–84. Metals. Tensile testing methods. Moscow, Publishing House of Standards, 1985.
2. Golovin Y. I., Physics of the Solid State **63** (1), 3–42 (2021).
3. Johnson K. L., Proc. R. Soc. Lond. A **324** (1558), 301–313 (1971).
4. Voronin N., Materials Physics and Mechanics **22** (1), 20–29 (2015).
5. Haggag F. M., ASTM Special Technical Publication **1204**, 27–27 (1993).
6. Kushnereva A. S. Industrial Laboratory **91** (4), 78–84 (2025).
7. GOST R 8.748–2011. State System for Ensuring the Uniformity of Measurements. State Verification Scheme for Pressure Measuring Instruments. Moscow, Standartinform, 2012.
8. Oliver W. C., Journal of materials research **7** (6), 1564–1583 (1992).
9. Oliver W. C., Journal of materials research **19** (1), 3–20 (2004).
10. Xiaodong L., Materials Characterization **48**, 11–36. (2002).
11. Handbook of Physical Quantities / Ed. Kikoin I. K. Moscow, Nauka, 1976.
12. Himabindu B., Materials Today: Proceedings **47**, 4891–4896 (2021).
13. Reshetov V.N., Nanoindustry **15** (7-8), 466–476 (2022).

About authors

Useinov Alexey Serverovich, Candidate of Physical and Mathematical Sciences, Senior Researcher at the Functional Materials Testing Center, Moscow Institute of Physics and Technology (9 Institutskiy per., Dolgoprudny, Moscow Region, 141701, Russia); Deputy Director, Vereshchagin Institute for High Pressure Physics Russian Academy of 14 Sciences (14 Kaluzhskoe shosse, Troitsk, 108840, Russia). E-mail: useinov@mail.ru SPIN-code: 41532, ORCID: 0000-0002-9937-0954 2318-4230, AuthorID: 41532, ORCID: 00000002-9937-0954

Sultanova Gulnaz Khakkimovna, Engineer at the Functional Materials Testing Center, Moscow Institute of Physics and Technology (9 Institutskiy per., Dolgoprudny, Moscow Region, 141701, Russia); Junior Researcher at the Laboratory of Nanomechanical Testing, National Research Center «Kurchatov Institute» (7a Central'naya st., Moscow, Troitsk, 108840, Russia). E-mail: sultanova.gkh@phystech.edu SPIN-code: 7358-9564, AuthorID: 1189457, ORCID: 0000-0002-4770-5724

Laktionov Ivan Valerievich, Engineer at the Functional Materials Testing Center, Moscow Institute of Physics and Technology (9 Institutskiy per., Dolgoprudny, Moscow Region, 141701, Russia). E-mail: laktionov@mipt.ru, SPIN-code: 8452-3715, AuthorID: 1111093, ORCID: 0000-0002-8576-3669

Fedotkin Alexander Pavlovich, Engineer at the Functional Materials Testing Center, Moscow Institute of Physics and Technology (9 Institutskiy per., Dolgoprudny, Moscow Region, 141701, Russia). E-mail: aleksandr.fedotkin@phystech.edu SPIN-code: 8957-9170, AuthorID: 1232517, ORCID: 0000-0003-3822-4811

PHYSICAL EQUIPMENT AND ITS ELEMENTS

UDC 614.485; 614.487 PACS: 87.50; 92.60.Sz
EDN: SQWVLQ

UV protection grating for UV reactors with gas flow

© D. E. Naumenko[1,2,*], N. A. Kolesnik[1], and L. M. Vasilyak[3]

[1] *LIT, Moscow Region, Dolgoprudny, 141701 Russia*
[2] *Moscow Institute of Physics and Technology, Moscow Region, Dolgoprudny, 141701 Russia*
[*] *E-mail: ddannaum@yandex.ru*
[3] *Joint Institute for High Temperatures of the Russian Academy of Sciences, Moscow, 125412 Russia*

Received 20.11.2025; revised 12.12.2025; accepted 20.02.2026

An analysis of light-shielding protection grating designs (U-shaped, honeycomb, and louvered) for flow-through UV reactors revealed a contradiction between achieving a high level of UV radiation shielding and low aerodynamic drag. A louvered grating with angled lamellas complemented by straight inlet and outlet sections was proposed. Numerical modeling and experimental studies showed that the new design provides a level of UV radiation attenuation comparable to the best analogs, such as a U-shaped grating, while reducing aerodynamic drag by a factor of 9. Flow alignment in the UV reactor was achieved, noise levels were reduced to below 40 dB, and the reactor's dimensions were reduced without any loss of performance.

Keywords: UV radiation, UV reactor, UV disinfection, recirculator.
DOI: 10.51368/2949-561X-2026-1-79-83

Introduction

Flow-through gas UV reactors are widely used in different fields, including air disinfection in recirculating systems, removal of contaminating gases and odors, as well as conducting photochemical reactions. Recirculators with air disinfection with UV-radiation are widely used in medical institutions, food processing facilities, public and residential premises, as well as other crowded places. UV radiation occupies a leading position [1] among methods of air disinfection methods due to its effectiveness among a wide spectrum of microorganisms and the absence of formation of harmful by-products. Practical operation reveals a number of technical difficulties related to ensuring reliability and efficiency of UV recirculators. One of them is the need to shield UV radiation coming from the disinfection chamber for the protection of people against exposure. For this purpose, light-protective grids are used at the input and output of the reactor with UV-radiation, the material and design of which have contradictory requirements. On the one hand, the grid must ensure safety by blocking the escape of UV radiation outside the unit’s body. On the other hand, its structure should not impair the aerodynamic and acoustic (noise) indicators of system operation, at the same time, the material of grids should be resistant to UV radiation. An unsuccessfully designed grid creates significant aerodynamic resistance, can be a cause of low bactericidal efficacy and increased noise level during the system operation. Protective grids currently used in recirculators design have high aerodynamic resistance and create additional noise or insufficiently shield UV radiation.

The purpose of this study was to develop the design of light-protective grid of the UV reactor with a high degree of UV radiation shielding, low loss of airflow pressure, maintenance of uniform flow in the disinfection chamber and low noise level.

Geometry of the protective grid

Recirculators use several types of light-protective grids: grids based on embedded U-shaped profiles [2] (fig. 1*a*); louvered grids with wave-shaped lamels (fig. 1*b*); honeycomb filters made of sheet metal (fig. 1*c*).

U-shaped grids demonstrate the maximum UV radiation shielding efficiency compared to louvered and honeycomb ones. However, the trajectories of air flows in such grids include two consecutive 180° turns, which in combination with local velocity increase in the channels leads to significant loss of head.

Honeycomb metal filters have lower aerodynamic resistance than U-shaped grids. Loss of head in the honeycomb filter are related to the interaction and friction of differently directed jets at the grid outlet, as well as with energy dissipation of turbulent vortices at the result of their contract with the reactor walls and surrounding jets. The geometry of honeycombs in most cases excludes the straightline passage of UV radiation, however, there is a critical angle of rays incidence for them, at which the number of internal reflections is insufficient for effective weakening of UV radiation.

Louvered grids have a low aerodynamic resistance, however, they do not always provide a required level of UV radiation shielding. To increase the level of UV radiation absorption, the lamels of grids are covered with absorbing coatings (paints), however, under prolonged exposure to UV radiation they are destructed with emission of resulting products into the air stream [3]. Currently used shape of lamels sets the flow direction different from the normal to the grid's plane which results in flow breakdown from one of the walls of the UV reactor chamber, causes the formation of turbulent zones and unequal distribution of velocities in the reactor's displacement volume.

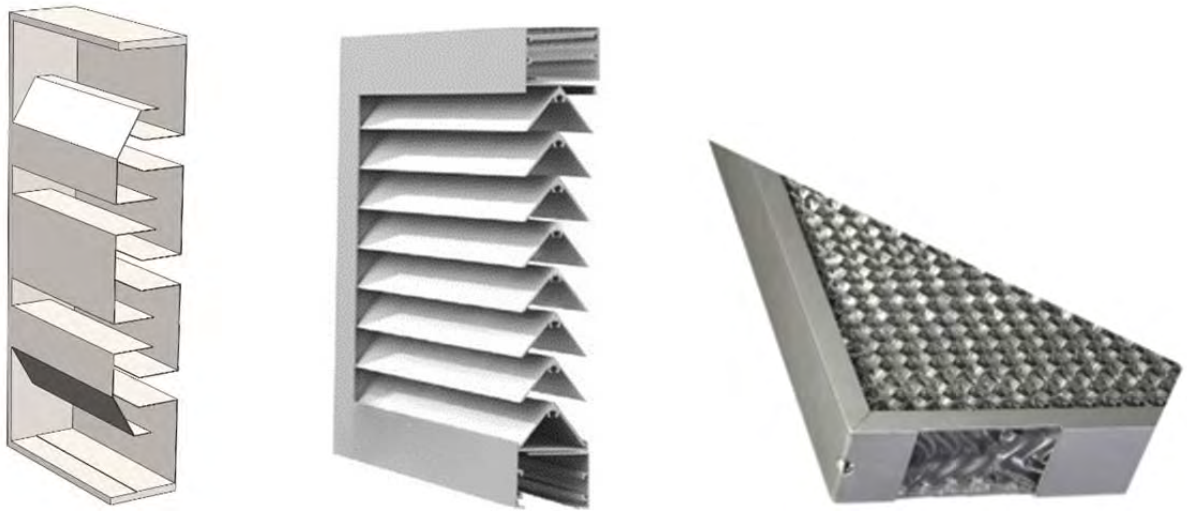

a) *b*) *c*)

Fig. 1. Types of grids. a) – U-shaped, b) – louvered, c) – honeycomb

Non-uniformity of the field of velocities in the reactor's working chamber results in significant variation in the residence time of various parts of the air stream in it. Part of microorganisms goes through the radiation area in a time different from calculated time and receive a radiation does lower than required threshold which does not ensure their inactivation. As the result, the total disinfection efficiency of the recirculator decreases. To compensate for the decrease in compensation efficiency, it is required either to increase the power of UV lamps or to decrease the flow rate to increase the exposure time, which reduces the unit performance. The structure of grids and the reactor must ensure not only the blockage of UV radiation but also equalizing air flow behind the grate.

As part of the analysis of existing structures, a louvered-type grid scheme was created for further development. To achieve the set goals a new lamel profile was developed with is an angular V-shaped structure with added straight-lined inlet and outlet sections direction

along the air channel of the system. Functional purpose of these areas is as follows:

1. The inlet area is designed for segmentation and stabilization of incoming flow before it moves into the labyrinth part of the profile which contributes to the decrease of turbulence generation inside the grid.

2. Outlet section ensures the orientation of the airflow along the disinfection chamber axis after passing the labyrinth, minimizing the jet deflection onto the chamber walls.

3. Additional straight-line sections increase light-protective characteristics by increasing the number of rereflections in the interlamellar space of the grids and creating additional shielded areas of UV radiation trajectories.

Numerical modeling

At the first stage, numerical modeling of hydrodynamic and optical characteristics of two types of light-protective grids was conducted: a traditional structured based on U-shaped profiles and developed grid consisting of angular lamels with additional straight-lined sections.

Hydrodynmaic modeling was conducted using the finite-volume method (CFD-modeling by FVM method with RANS [4] turbulence model). Borderline conditions for CFD-model were set as follows: dimensions of the air duct 250 mm × 300 mm; a uniform flow velocity of 1 m/s is set at the outlet; static pressure equal to atmospheric pressure – at the inlet; channel walls were considered smooth and impenetrable, and the roughness of 1 μm was considered for grids surface; linear dimensions of computational cell were 1 mm. Both grids were modeled in the same overall dimensions. Geometrical parameters of light-protective grid with U-shaped profile are shown in the left part in fig. 2*a*, louvered grid – in fig. 2*b*.

The program of numerical modeling provided for:

1. Visualization of flow patterns and velocity vector fields;

2. Calculation of velocity distribution in the cross section at a distance of 100 mm behind the grid;

3. Determination of the difference value of the total pressure on the grid;

4. Calculation of attenuation coefficient of the UV radiation by grids.

Results of CFD-modeling of flow trajectories in the grid and on the reactor are shown in fig. 2. Fig. 2*a* shows the distribution of flows with grid with U-shaped lamels profile, fig. 2*b* – a grid with lamels with the structure designed in the plane of symmetry of the problem. The grid with P-shaped lamels is characterized by wider velocity spread, occurrence of vortices and development of turbulence at the grid outlet which resulted in local increase of flow rate in the disinfection chamber, as expected based on the flow conservation equation. Open area at the outlet for grid with U-shaped profiles was 20 % of the channel cross section, which is the reason for a local increase in flow rate at the grid's outlet by 5 times relative to the velocity behind the grid. Open area at the grid outlet with angular lamels is 90 % of the channel cross section, so the air flow rate at the outlet of the grid channels is increased only by 10 % compared to the velocity in the channel. There are no vortices behind the grid, the flow velocity profile is fairly uniform. Mean square deviation of the velocity at the distance of 100 mm from the grid outlet was 1.03 for the grid with U-shaped lamels and 0.27 for the grid with angular lamels. Differential pressure for grids with U-shaped lamels was 81.1 Pa, and for the grid with angular once only 12 Pa.

Calculation of light-protective properties of grids were conducted by ray tracing method. For ray tracing, models were used that consider the reflection coefficient of UV radiation with a wavelength of 254 Nm and combined diffuse-specular nature of reflection from surfaces. Results of modeling of UV radiation distribution show that the grid made of angular lamels ensures an average shielding in the output plane comparable to that in the case of using grid with U-shaped lamels. At the same time, the peak values of radiation behind both grids are at the same comparable level. Design average attenuation of UV radiation (averaging of the cross-sectional area of the air duct) defined as $\lg(E_0/E)$, where E_0 and E are exposure rates without and with grid, respectively, for U-shaped grid it was 3.50, for grid with angular lamels – 3.44, which is enough to provide safety.

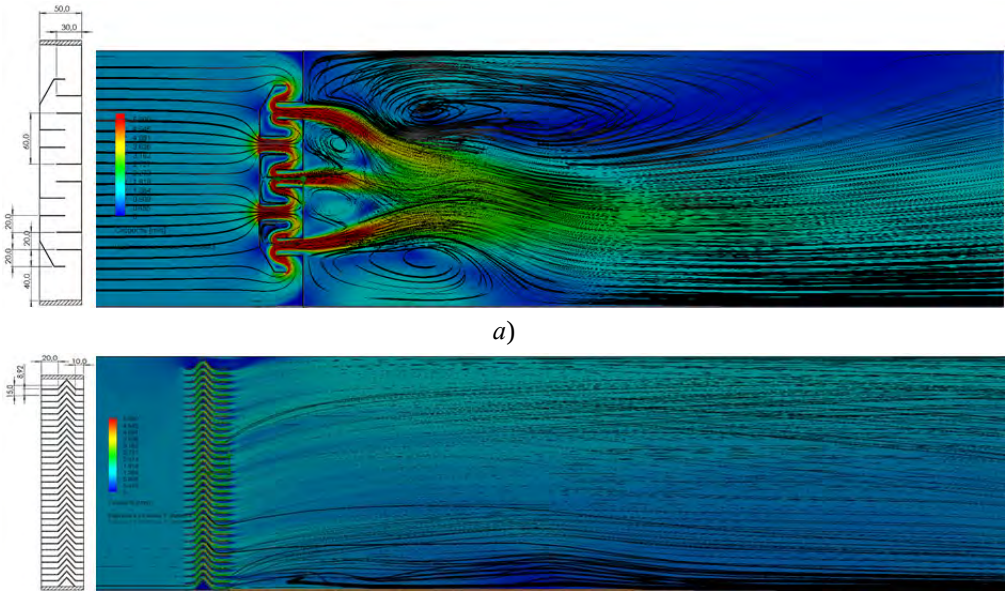

a)

b)

Fig. 2. Trajectory of flows in the grid and reactor: a) – U-shaped grid; b) – louvered. Air flow from left to right. Geometry of grids is shown on the left

Comparison with the experiment

Experimental verification of the results of numerical modeling was conducted at the second stage of the study. Differential pressure was measured in the air duct with cross-section identical to the calculation model with installed metal light-protective grids. A centrifugal fan located at the channel output was used to create air flow. Regulating flow rate in the rage of 0.3–1.8 m/s, respectively, was conducted using a PWM controller, regardless of the type of the installed gird, the velocity measurement was conducted using Testo 417 anemometer. Measurement of differential pressure on the grid was performed by digital differential pressure gauge. Measured differential pressure values depending on air velocity in the channel are shown in fig. 3.

As follows from fig. 3, up to the air flow velocity v = 0.6 m/s, pressure differences on both grids differ insignificantly. Starting from a velocity of 0.8 m/s, U-shaped grit had a multiple higher resistance than an angular one. At a flow velocity of 1 m/s, the differential pressure on the angular grid is 5 Pa, and on the U-shaped grid the interpolated value is 48 Pa. Thus, by using protective grid with angular lamels for the reactor with gas flow, it is possible to reduce the pressure drop by an order of magnitude at flow rates of more than 1 m/s.

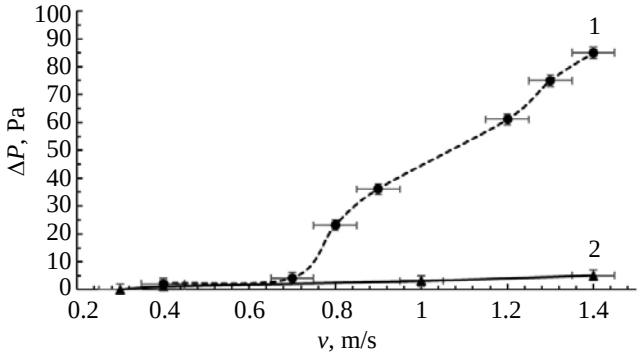

Fig. 3. Dependence of differential pressure ΔP, Pa upstream and downstream of the grid on the air velocity. 1 – grid with U-shaped profiles, 2 – angular grid

Flow breakdown on the fan blades is one of the main sources of aerodynamic noise in air duct systems, since the turbulent vortices that appear during the process cause pressure fluctuations and, consequently, sound waves [5]. The reduced grid resistance made it possible to reduce the overall pressure drop in the recirculator which resulted in the decrease of noise from the device, since the fan created a lesser pressure drop in the chamber which led to a decrease in the number of flow breakdowns on its blades. The noise reduction effect was measured using method recommended by GOST R ISO 3744-2013 [6] for two test reactors having the same dimensions and fans but different light-protective grids. The system with two U-shaped grids had a noise level of 42 dB, and the system with the proposed angular grids – 36 dB. It is worth noting that the

noise level from devices in different institutions is strictly regulated, for example, in hospital wards and operating theaters, the noise level should be lower than 40 dB [7].

To measure the light-protective efficiency of the grids in the air duct, a U-shaped UV lamp with a power of UV radiation of 33 W at a wavelength of 254 nm was placed in 100 mm from the open end, and the test grid was installed at the channel's output. Measurement of initial irradiance without grid was conducted using ILT2400 digital radiometer in the plane located at a distance of 100 mm from the channel edge perpendicular to its axis along a grid of 5×9 points. After the test grid was installed on the open pipe edge, the measurements were repeated at the same points. The light-protective efficiency was determined by the attenuation coefficient, as the logarithm of the ratio of the irradiance values at the points before and after the installation of the grid. For U-shaped grid the average attenuation was 3,88, and for the angular grid – 2,97 which complies with calculations for ray tracing model. Thus, angular grid with such attenuation ensures a reduction in UV intensity to values not exceeding the permissible levels defined in SanPiN 2.2.4.3359-16 [8].

Conclusion

The proposed design of light-protective grid with angular lames with additional plane guides which is significantly superior to the existing analogs for UV reactors with gas flow. The measured degree of UV radiation shielding with a wavelength of 254 nm was 2,97 which is comparable to the attenuation degree of the best sample of light-protective grids, and aerodynamic resistance at flow rates of 1 m/s is reduced by an order of magnitude compared to the widespread grid with U-shaped profiles. Moreover, angular grid with additional straight-lined guide sections stabilizes the flow in the UV reactor chamber and minimizes its separation and reduces velocity variation to the men-square deviation of 0.27. Currently used grid with U-shaped profile creates strong spatial deviations of the flow behind the grid, occurrence of vortices and large velocity inhomogeneities in the reactor chamber with mean square deviation of velocity at a distance of 100 mm from the grid's outlet equal to 1.03. Such differences are explained by a fourfold increase of open area of angular grid compared to the U-shaped one and presence of straight-lined guides. The noise level was reduced to 36 dB which is lower than the threshold level 40 dB according to SanPiN [6] without loss of performance which was previously impossible when using U-shaped light-protective grids with noise level of 42 dB. A more stable gas flow is obtained in the radiation chamber of the UV reactor which increases the efficiency of air disinfection. The use of improved light-protective grids made it possible to increase the air velocity in the reactor which allowed to halve the overall dimensions of the recirculator. The proposed design is used in serial devices of NPO "LIT" UV circulators.

REFERENCES

1. Vasilyak L. M., Plasma Phys Rep. **47**, 318 (2021).
2. Sizikov V. P., Device for Air Disinfection. Patent for invention № 2462269C1 (RF). 2011 [in Russian].
3. Savenkov D., Donskoy D., Limarenko N., and Gladckih D., E3S Web of Conferences, 05010–05018 (2024).
4. Menter F., Hüppe A., Matyushenko A., and Kolmogorov D. J., Appl. Sci., **11** (6), 2459 (2021).
5. Roger M. and Moreau S. J., AIAA, **42** (3), 536–544 (2004).
6. GOST R ISO 3744-2013. Acoustics. Determination of sound power levels and sound energy levels of noise sources using sound pressure. Engineering methods for an essentially free field over a reflecting plane [in Russian].
7. SanPiN 1.2.3685-21. Hygienic Standards and Requirements for Ensuring the Safety and (or) Harmlessness of Environmental Factors for Humans [in Russian].
8. SanPiN 2.2.4.3359-16. Sanitary and Epidemiological Requirements for Physical Factors at Workplaces [in Russian].

About authors

Naumenko Danila Evgenevich, head of air handling equipment department, LIT (25 Likhachevskij proezd, Dolgoprudny, Moscow Region, 141701, Russia); student, Moscow Institute of Physics and Technology (9 Institutskiy per., Dolgoprudny, Moscow Region, 141701, Russia). E-mail: ddannaum@yandex.ru SPIN-code: 3670-9247, AuthorID: 1318520

Kolenikov Nikita Alexandrovich, leading designer of UV-devices development team. LIT (25 Likhachevskij proezd, Dolgoprudny, Moscow Region, 141701, Russia). E-mail: kolesnik@lit-uv.ru

Vasiliak Leonid Mikhailovich, Doctor of Physics and Mathematics, Chief Research Assistant, Joint Institute for High Temperatures of the Russian Academy of Sciences (Bd. 2, 13 Izhorskaya st., Moscow, 125412, Russia). Email: vasilyak@ihed.ras.ru SPIN-code: 5623-5167, AuthorID 19599. ORCID 0000-0001-6982-3038. Scopus 7004886755

PHYSICAL EQUIPMENT AND ITS ELEMENTS

UDC 53.096 PACS: 51.50.+v
EDN: TIDUIN

Hydrogen current generator based on Pd/InP Schottky diode

© V. A. Shutaev*, E. A. Grebenshchikova, and Yu. P. Yakovlev

Ioffe Institute, Russian Academy of Sciences, St. Petersburg, 194021 Russia
** E-mail: vadimshutaev@mail.ru*

Received 18.09.2025; revised 10.10.2025; accepted 20.02.2026

A new current generator based on Pd/InP Schottky diode with an area of 1 mm^2 operating in hydrogen medium in complete darkness has been created. It is established that in a short-circuit regime a "hydrogen current" of the Schottky diode increases by about three orders of magnitude with increasing the temperature from 90 to 300 K. It is shown that the increase of the "hydrogen current" with increase the temperature is related to the decrease of the potential barrier height of the diode in the temperature range 90–300 K. The mechanism of current generation in Pd/InP Schottky diodes in 100 % hydrogen, consisting in appearance of an additional number of electrons in Pd-layer as a result of palladium hydride formation, is proposed.

Keywords: hydrogen, palladium, Pd/InP, ionization, palladium hydride.

DOI: 10.51368/2949-561X-2026-1-84-87

Introduction

Electrical properties of Schottky diodes Pd/InP in the gaseous environment with hydrogen are studied to create hydrogen detectors [1–5]. At the same time, changes in current-voltage and capacity characteristics of such diodes are studied in hydrogen compared to air environment, and all measurements are usually performed when applying an external voltage. In hydrogen, the work function of palladium changes [6, 7] and, consequently, the height of potential barrier in Pd/InP diodes, at the same time, the electrical characteristics of diodes also change, and the change of characteristics can be used to judge the hydrogen concentration in gaseous environment.

Previously, current conduction mechanisms [1, 2] in Pd/InP structures in hydrogen environment with and without LED illumination of the structure at room temperature without the application of external voltage were investigated. In study [3] current generation was detected in Schottky diodes Pd/InP when placing them in hydrogen environment without applying external bias. This study is a continuation of the above-mentioned papers and dedicated to the study of current generation and EMF in Pd/*n*-InP structures in the temperature range of 90–300 K in the hydrogen atmosphere.

Experiment

The manufacturing process of the studied Pd/InP structures is described in detail in [1–3]. A palladium layer with an area of 1×1 mm^2 and thickness of 25 nm was created by thermal vacuum deposition of 99.96 % purity on InP single crystal wafers with the electron concentration Pd of 10^{16} cm^{-3}. Gold-based ohmic contacts were created for palladium and InP. Electrical properties of Pd/InP structures were studied in the temperature range of 90–300 K in vacuum and hydrogen environment. The study of structures was conducted under the conditions of short-circuited electrical circuit and in the open-circuit mode. To assess the temperature dependence of the height of the potential barrier in the studied Schottky diodes, current-voltage characteristics were measured in complete darkness in vacuum and in the 100 % hydrogen environment.

When studying electrical characteristics of Pd/InP structures, KEITLEY-6517B (Keithley Instruments, Inc.) electrometer was used with data output to a computer.

Experiment results

Let us consider the current behavior in the hydrogen atmosphere in the temperature range of 90–300 K (fig. 1). “Hydrogen current”, i.e. the current that appears only in hydrogen environment in the short-circuit mode in complete darkness, increases by about 3 orders of magnitude with temperature increase from 90 to 300 K.

At $T \sim 270$ K, the current reaches the maximum value of 10 μA at a structure area of 1 mm^2. Based on the dependence of EMF (E) on the temperature in the hydrogen environment (fig. 2), fluctuation in the considered temperature range can be distinguished, however, there is a tendency for EMF to increase in absolute value when temperature decreases. EMF reaches the maximum value $|E| = 170$ μV at a temperature of 90 K.

Fig. 3 shows the dependence of the potential barrier height of Schottky diode Pd/InP on the temperature in 100 % hydrogen. Height of the potential barrier was determined according to the cutoff potential value of the current-voltage characteristics extrapolated to I = 0.

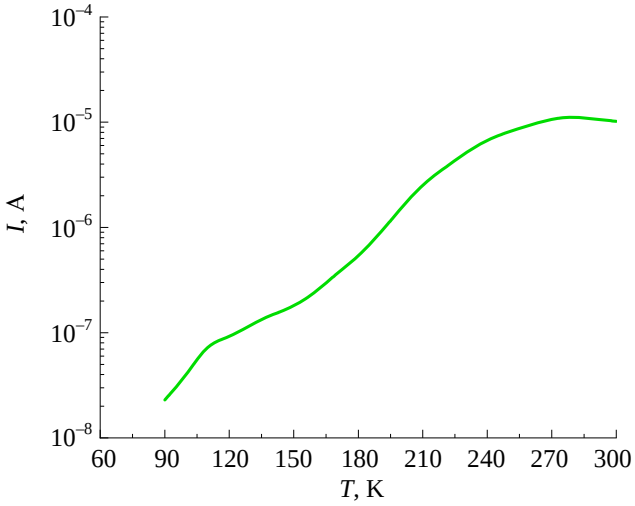

Fig. 1. Temperature dependence of current generation in the hydrogen atmosphere

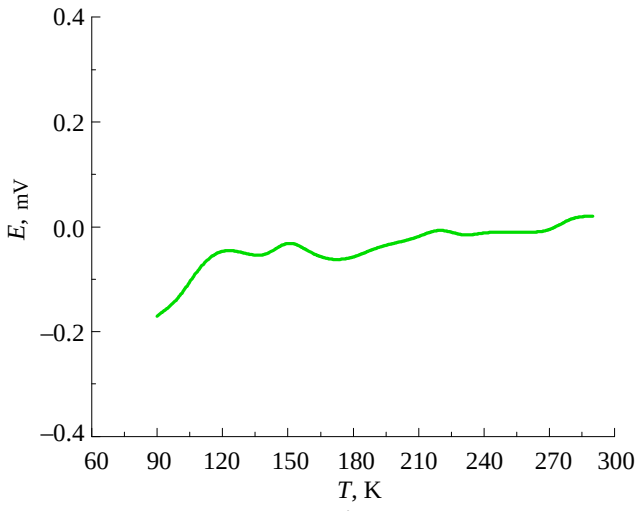

Fig. 2. Temperature dependence of EMF generation in the hydrogen atmosphere

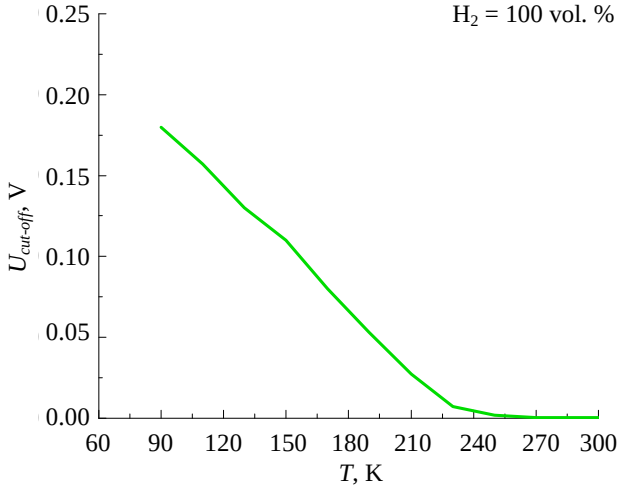

Fig. 3. Temperature dependence of the potential barrier height

The presented chart shows that the barrier height of Schottky diode in the hydrogen medium decreases monotonously from 0.18 to 0 eV with increase of the temperature from 90 to 270 K.

Results analysis

The appearance of “hydrogen current” in Schottky diodes in the hydrogen environment can be related, according to the authors, to the formation of an additional electrons in the Pd-layer. Formation of the additional number of electrons, in turn, can be the result of two factors. Firstly, ionization of hydrogen atoms is possible upon contact of hydrogen with Pd-layer. As was shown in study [8], when hydrogen atoms approach Pd atoms at a distance less than Bohr radius, energy of hydrogen atoms ionization can be reduced to 0 eV. Secondly, upon contact of hydrogen with Pd-layer, palladium hydride PdH_x is formed [9, 10]. The process of PdH_x formation is exothermic and occurs with the release of thermal energy [11]. Combined effect of these two factors possibly leads to the appearance of the additional electrons in the palladium layer.

After the formation of the additional electrons, they drift from the palladium layer to InP. Potential barrier of Schottky diode significantly restricts the flow of electrons formed at the result of ionization. In the hydrogen environment
(100 vol. %), the barrier height of Schottky diodes Pd/InP decreases linearly from 0.18 to 0 eV when temperature increases from 90 K to 270 K. At the barrier height close to 0 eV, conditions arise for free electrons flow along the electrical circuit. The current generated as the result of this effect is maximum at a temperature of 275–280 K. With a further increase of temperature to 300 K, a gradual decrease in the generated "hydrogen current" begins. The resistance of the potential barrier determined by the slope of current-voltage characteristics at a voltage value of 10 mV decreases from 10^5 to 1–2 Ohm at temperature increase from 90 to 300 K.

Fig. 4 shows band diagrams explaining the obtained experimental result. The height of Schottky diode Pd/InP barrier in vacuum is determined by difference between the work function of Pd and InP and is 0.32 eV at $T = 90$ K. When palladium interacts with hydrogen in complete darkness at room temperature, ionization of hydrogen atoms occurs with the formation of protons and electrons, and palladium work function W_{Pd} decreases by 0.3–0.7 eV [2, 6].

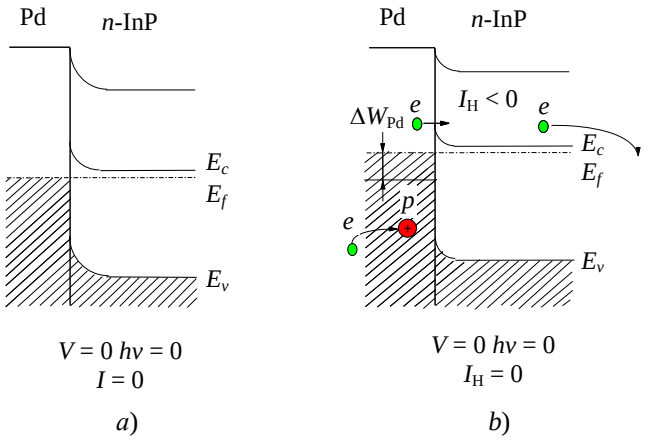

Fig. 4. Band diagrams and currents in the Pd/InP structure, external voltage on the sample is equal to zero, electrical circuit is short-circuited, T = 90 K: a – in the vacuum; b – in the hydrogen; I_H – “hydrogen current”; ΔW_{Pd} – change of Pd work function in hydrogen; e – electrons; p – protons

A decrease in W_{Pd} results in decrease in Schottky barrier height. As a result of separation of charge carries, short circuit current appears in the structure the value of which depends on the barrier height. As the temperature decreases, the barrier height increases and electrons begin to accumulate near the Pd/InP interfacial area. This causes the short-circuit current to decrease and the open-circuit EMF to increase. Duration of current flow in the structure at $T = 300$ K is maintained for a day and then it linearly decreases for 7 days to 10 % of the original value. When hydrogen is repeatedly filled into the cell, the current increases to the same value as at first hydrogen filling (10 μA) The value of generated current (10 μA) is proportional to the structure area (1 mm^2) It is worth noting that with temperature increase from 90 to 300 K, the barrier height in the hydrogen environment will reduce and approach to 0 eV due to the reduction of energy band gap E_g in InP.

Conclusion

The current generation and EMF were studied in vacuum and hydrogen environment in

the temperature range of 90–300 K in complete darkness. In the hydrogen environment, Schottky diodes generate current in the temperature range of 90–300 K. The value of generated current increases by about 3 orders of magnitude with temperature increase from 90 to 300 K. EMF value increases by absolute value from 0 to 170 μV with temperature decrease from 300 to 90 K. Current generation may be due to the formation of the additional electrons due to the formation of palladium hydride during hydrogen interaction with Pd layer.

The authors declare that they have no conflict of interests.

REFERENCES

1. Shutaev V. A., Grebenshchikova E. A., Sidorov V. G., and Yakovlev Yu. P., Semiconductors **56** (14), 2170–2173 (2022).
2. Shutaev V. A., Sidorov V. G., Grebenshchikova E. A., Vlasov L. K., Pivovarova A. A., and Yakovlev Yu. P., Semiconductors **53** (10), 1389–1392 (2019).
3. Shutaev V. A., Sidorov V. G., Grebenshchikova E. A., and Yakovlev Yu. P., Semiconductors **58** (1), 34–37 (2024).
4. Chou Y.-I., Chen C.-M., Liu W.-Ch., and Chen H.-I., IEEE Electron Device Lett. **26** (2), 62–65 (2005).
5. Kumar A. A., Janardhanam V., and Reddy V. R., J. Mater Sci: Mater Electron, № 22, 854–861 (2011).
6. Yamamoto N., Tonomura S., Matsuoka T., and Tsubomura H., J. Appl. Phys. **52** (10), 6227–6230 (1981).
7. Skucha K., Fan Zh., Jeon K., Javey A., and Boser B., Sensors Actuators B, № 145, 232–238 (2010).
8. Konstantinov O. V., Dymnikov V. D., and Mitsev M. A., Semiconductors **42** (8), 931–933 (2008).
9. Ube T., Hasegawa S., Horie T., and Ishiguro T., J. Mater. Sci., № 56, 3336–3345 (2021).
10. Ndaya C. C., Javahiraly N., and Brioude A., Sensors **19** (4478), 1–41 (2019).
11. Bar'yudin L. E., Fiz. Tverd. Tela **37** (5), 1484–1491 (1995) [in Russian].

About authors

Shutaev Vadim Arkadievich, Candidate of Physical and Mathematical Sciences, research scientist, Ioffe Institute, Russian Academy of Sciences (26 Politekhnicheskaya st., St. Petersburg, 194021, Russia). E-mail: vadimshutaev@mail.ru

Grebenshchikova Elena Aleksandrovna, Candidate of Physical and Mathematical Sciences, senior research scientist, Ioffe Institute, Russian Academy of Sciences (26 Politekhnicheskaya st., St. Petersburg, 194021, Russia). Email: lot160@mail.ru AuthorID: 116448

Yakovlev Yuri Pavlovich, Doctor of Physics and Mathematics, Senior Research Assistant, Ioffe Institute, Russian Academy of Sciences (26 Politekhnicheskaya st., St. Petersburg, 194021, Russia). E-mail: yakovlev.iropto@mail.ioffe.ru SPIN-code: 3394-1498, AuthorID: 20496

Happy anniversary!

On February 21, 2026, Igor Burlakov, Doctor of Technical Sciences, Professor, Deputy General Director for Innovation and Science at the State Research Center of the Russian Federation “Research, Development and Production Center ORION” JSC, celebrated his 70th birthday.

In 1979, I. Burlakov graduated from the Moscow Institute of Physics and Technology with a speciality in physicist-engineer. Since 1976, he has been continuously working at RD&P Center ORION JSC, progressing from a junior researcher to Deputy General Director for Innovation and Science.

I. Burlakov is a well-known specialist in the field of optoelectronics and photonics technologies, semiconductor physics, and photoelectronic devices. For the first time in Russia, he developed the basis of industrial technology for cooled focal plane arrays (FPA) based on the semiconductor compound cadmium-mercury-telluride. As a leader, he possesses the ability to successfully find optimal approaches and make prompt decisions to achieve his set goals. The advanced infrared FPAs and optoelectronic devices created under his leadership and with his direct participation have found wide application in systems and complexes for defense and civil purposes. The completed developments are competitive on the global market and create the basis for the transition of infrared optical information technologies to a new grade generation.

I. Burlakov carries out extensive scientific, organizational, and pedagogical work as the Head of the Basic Department of Infrared Technology and Electronic Optics at the Russian Technological University – MIREA, Chairman of the State Examination Committee of the School of Electronics, Photonics, and Molecular Physics at the Moscow Institute of Physics and Technology, Editor-in-Chief of the journals "Advances in Applied Physics" and "Applied Physics," Member of the Editorial Board of the "Optical Journal", Deputy Chairman of the Dissertation Council at RD&P Center ORION JSC, and Member of the Dissertation Council at the Moscow Power Engineering Institute (MPEI). He has supervised 3 doctors and 6 candidates of science. He is the author of more than 340 scientific papers published in

Russian and foreign journals, including more than 35 invention patents, 3 books, and 3 training edition.

Burlakov's high level of professionalism, extensive experience, and in-depth knowledge of the industry's development prospects enable him to perform extensive expert work as a member of the Presidium of the Interdepartmental Expert Council for Federal Project No. 3 (Strategic Materials), a member of the Expert Council for Scholarships for Outstanding Achievements and Significant Contributions to the Creation of Breakthrough Technologies and the Development of Modern Equipment for the Country's Defense and Security, and an expert for the Advanced Research Found.

For his many years of scientific, technical, and leading work, he has received awards and honors from federal government agencies, including the Honorary Worker of Science and Technology of the Russian Federation, and was awarded the Government of the Russian Federation Prize in Science and Technology in 2024.

The Editorial Board and the Editorial Office of the journal "Applied Physics" sincerely thank you, Igor Burlakov, for your invaluable contribution to the development of the journal, which, thanks to your professionalism, demanding nature, and ability to see the future, is one of the most famous and respected Russian scientific publications. Together with your numerous colleagues, friends, and students, we congratulate you on your glorious anniversary and wish you good health, fruitful scientific and educational activities, success, and good luck in achieving outstanding results.

INFORMATION

Rules for submission, reviewing and publishing of scientific papers

(as revised in 2026)

1. The “Applied Physics” journal is mainly intended for urgent publication of short papers concerning recent achievements in physics that have a potential of applied (technical and scientific) use. The journal is included in the new List of the Higher Attestation Commission, which came into effect on December 1, 2015.

By sending the article manuscript to the journal’s editorial board, the authors grant the editorial board, founder and publisher of the journal a free, non-exclusive right to publish it in Russian as an article in the printed version of the journal, in the electronic version of the journal in the Internet and on laser disks. At the same time the authors retain their intellectual rights to the article manuscript (including “copyright”). In this regard and considering Part Four (Section VII) of the Civil Code of the Russian Federation, the authors shall submit a letter to the editor in the following form:

License agreement for transfer of the publish right (publishing license agreement)

We, the undersigned, the manuscript authors _____,
grant the editorial board, founder and publisher of “Applied Physics” journal a free, simple (non-exclusive) license to publish the article manuscript in both printed and electronic journal versions.

We confirm that this publication does not violate the intellectual rights of other persons or organizations. Signatures of authors: _____ (full name, academic degree, date)

The article shall be signed by all authors. If there are several authors, the name of the author responsible for message exchange with the editorial board shall be indicated. The article manuscript shall be sent to the address of the journal’s editorial board: 111538, Moscow, Kosinskaya st, 9, AO NPO Orion, editorial board of “Applied Physics” journal or by e-mail: advance@orion-ir.ru

2. The article manuscript shall be submitted to the editor only in Russian.

3. The article manuscript shall be accompanied by an expert opinion whether its publication in the open media is allowed, which shall be drawn up in accordance with the established procedure.

4. The article size (including figures, bibliography and the English-language part) shall not exceed **7 pages** of A4 format with single line spacing. (A larger article is proposed to be sent to the affiliated **"Applied Physics Advances”** journal intended for publication of detailed articles and reviews). The article material shall be submitted in printed form (on paper) and in electronic form on a CD/DVD disk with the text in Word format (font type – Times New Roman, font size – 12), and the text shall already include figures with captions under them in the proper places. However, overly detailed and cumbersome mathematical transformations and expressions should be avoided in the text. The article styling shall be as follows:

– title of the journal section;
– UDK index;
– PACS classification code (https://publishing.aip.org/wp-content/uploads/2019/01/PACS_2010_Alpha.pdf);
– article title;
– initials and surnames of authors;
– abstract of the article (10–15 lines describing the purpose of the paper and its main findings);
– keywords;
– scientific specialty code.

5. The main text of the article shall begin with the “Introduction” section clearly stating the purpose and objectives of the paper along with arguments in favor of its preparation against the background of the existing state of the problem addressed in the article. The further text of the article shall also have meaningful headings (sections and subsections) without being numbered. The article shall end with a separate section, “Conclusion,” listing the main findings, conclusions that follow from them, and, if possible, proposals for the research advance and use of its findings.

The bottom of the first page of the text shall accommodate a separate paragraph (in bold) containing contact information about the author (or authors) **(mandatory section)**: surname, first name, patronymic (in full), **e-mail (of all authors),** profiles and registration numbers in scientometric databases (SPIN code, RINTS Author ID, ArXiv Author ID, Orcid ID, Scopus Author ID), academic degree, title, position, postal address of the enterprise).

Also a person responsible for message exchange with the editorial board shall be specified.

Authors can suggest potential reviewers (2–3 people by indicating their full name, place of work, and email address). The proposed candidates shall not work in the institutions where the authors do.

The main text shall be followed by the list of references called “Bibliography”.
Examples of designations of references used in the "Bibliography" section.

Articles shall be referred to as follows: Surname, initials, journal title, year, volume, issue, page numbers.
Ivanov I. I. / Applied Physics. 2022. No. 1. P. 12–18.
Lang D. V. / J. Appl. Phys. 1974. Vol. 45. No. 7. R. 3023–3034.
Reference to **books**: Surname, initials, book title, city, publisher, year. (When a specific chapter or page in a book is referred to, the page number is placed after the year.)
Korn G., Korn E. Mathematical Handbook. – Moscow: Nauka, 1974.
Biberman L. M., Vorobiev V. S., Yakubov I. T. Kinetics of non-equilibrium low-temperature plasma. – Moscow: Nauka, 1982. P. 371.
Ultraviolet technologies in the modern world / edited by Karmazinov F.V. Kostyuchenko S.V., Kudryavtsev N.N. – Dolgoprudny: Intellekt, 2012.

Reference to **conference proceedings:** Surname, initials, title of publication, place and date of publication, page numbers.
Romanov A. V., Stepovich M. A., Filippov M. N. / Proceedings of the XVII International Conference "Radiation Physics of Solids". – Sevastopol, 2007. P. 592–599.

Reference to **patents**: Surname, initials, title, type, number, year.
Davydov S. G., Dolgov A. N., Yakubov R. H. Vacuum spark gap. Patent of invention No. 2654494 (RF). 2018.

Reference to **dissertations and Abstracts**: Surname, initials, title of paper (abstract), diss. … Candidate (Doctor) of Physics and Mathematics, city, organization, year.
Grechikhin V. A. Development and analysis of computer algorithms for processing single-particle signals of laser Doppler anemometers: Abstract from diss. by Candidate of technical sciences. – Moscow: MPEI, 1996.

Further, detailed English-language information about the article required for indexing the entire journal, the given article and its authors in international scientometric databases shall follow, namely: PACS, article title, authors' surname and initials (English transliteration), enterprise, its postal address, author(s) e-mail, abstract, keywords, references; since the journal is also distributed abroad, the editorial board reserve the right to correct the English part of the text without changing its meaning.
Styling of the References in the English part of the article has its own peculiarities. In particular, if the cited book or monograph is a translation into Russian from a foreign publication, the original data of this publication (authors, book title, publisher, city or country, year of publication) shall be given, as well as the Russian publisher and the year of publication in Russian. Given below are the main examples of designation of used references in the References section:
Article from the journal:
Ivanov I. I., Applied Physics, No. 1, 12–18 (2022) [in Russian].
Lang D. V., J. Appl. Phys. **45** (7), 3023–3034 (1974).
Note: if a Russian journal has a printed English analogue, the English title of the analogue shall be used and page numbers shall be taken therefrom. If there is no English analogue, the English transliteration of the Russian name shall be used.

Book:
Korn G. and Korn E. Mathematical Handbook. New York-London, Mcgraw-Hill Book Company, 1968; Moscow, Nauka, 1974.
Ultraviolet technologies in the modern world / ed. Karmazinov F. V., Kostyuchenko S. V., Kudryavtsev N. N. Dolgoprudny, Intellect, 2012 [in Russian].

Conference proceedings:
Romanov A. V., Stepovich M. A., and Filippov M. N. Proc. XVII Intern. Meeting on Radiation Physics of Solid State. Sevastopol, 2007, pp. 592–599.

Patents:
Davydov S. G., Dolgov A. N., Yakubov R. H. Vacuum spark gap. Patent for invention No. 2654494 (RF). 2018.
Dissertations and Abstracts:
Grechikhin V. A. Development and analysis of computer algorithms for processing single-particle signals of laser Doppler anemometers: Abstract. Diss. Candidate of Technical Sciences. M., MEI, 1996.

6. The list of references (“References”) shall correspond to all references to external sources used in the text of the article. These references shall be enclosed in square brackets, for example, [1–3], [7, 8]. Internal references, i.e. references to formulas, figures and tables of the article shall be enclosed in round brackets, for example, formula (3), equation (1), (Fig. 2), (Table 3). Any references in figure captions or in the figures are not recommended.

7. The number of figures and photos for a typical article shall not exceed 4. If one figure contains two, three or more variants of graphic (or photo) images of the type “Fig. 2*a*”, “Fig. 2*b*”, etc., each individual variant is considered as a separate figure. If the above limit number of figures (photos) is exceeded, the article is sent back to the authors for revision. Graphics (black and white and color) shall be put directly in the proper place in the article and in the proper scale. Next to the graph axes, the displayed physical quantities shall be indicated only (**strictly!**) using symbols (letters), and after a comma - the quantity dimension in Russian (in direct font). It is recommended to number different curves on graphs, even if they are identified by a different color or line type. Graphs shall be submitted only (**strictly!**) against the white background. Auxiliary grids are not allowed in the graph area.

8. Captions under the corresponding figures shall be out in the proper places in the text. Each caption shall be as short as possible, but meaningful in terms of its content. Any physical (technical) symbol included in the caption shall have its verbal explanation there.

9. Simple formulas shall be included in the text in the format of the text editor used; more complex formulas shall included using MathType formula editor. Standard mathematical notations (e.g. max, log, sin, exp, etc.) shall be typed directly. The same is true about figures and numbers. Formula numbers shall written in parentheses on the right. To indicate non-vector physical (technical) quantities using symbols, use only the Latin and Greek alphabets, while using a straight font for Greek letters, and an oblique font (italics) for Latin letters in the text. Vectors and matrices shall be marked by a bold, upright font (preferred) or an arrow above the italic vector symbol (less preferred). For subscripts and superscripts, use Arabic numerals, Latin or Greek letters, but if the index, usually a subscript, is a short (abbreviated) form of the Russian characteristic word, it is allowed to use Russian letters in its designation (uppercase font), for example U_{in}, I_{out}, v_{gr}, etc. The dimension of physical quantities shall be always given only in Russian, using an uppercase font.

10. Tables shall be made in accordance with the following requirements: the top line contains the data name and dimensions; the following lines contain the data itself.

11. Formulas, tables and figures shall have their own separate continuous numbering system. If there are no additional (return) references to a specific formula in the text or it is used only once, it shall not be numbered. A table and/or a figure used only once do not require numbering either.

12. Manuscripts and CD/DVD will not be sent back by the editorial board.

13. Authors (or an author) of each article after it is published in a journal issue have a right to receive an electronic version of the article in PDF format (Adobe Acrobat editor) from the editorial board.

14. When published in the journal, each article is accompanied by a footnote with the copyright symbol © placed before the author's name (authors’ names). The article shall also specify the date the article was received by the editorial board.

Applied Physics: Scientific and Technical Journal / RD&P Center ORION, JSC, 2026. No. 1.

Signed to the press on February 20, 2026
A4 format. Offset paper.
Digital printing.
Printed in the printing house of LLC PKK "YOUR FORMAT".
Address: 15, Malaya Kaluzhskaya st., Moscow, 119071.
Tel. (495) 749-45-84